RSC Advances

REVIEW

View Article Online
View Journal | View Issue

Cite this: *RSC Adv.*, 2026, **16**, 18816

Recent advances in lignin-based carbon materials for pollutant removal and oil–water separation: a review

Sonal Vithoba Tarkar,[a] Anuradha K,[a] Ranjeet Kumar Mishra *[a] and Mubarak Marutholi[b]

Received 3rd January 2026
Accepted 10th March 2026

DOI: 10.1039/d6ra00055j

rsc.li/rsc-advances

The rapid escalation of water pollution from industrial effluents, oil spills, and emerging contaminants has created an urgent need for sustainable, high-performance remediation materials. Although surface water covers nearly 71% of the Earth's surface, only about 2.5% constitutes freshwater, and less than 1.2% is readily accessible for human use. Moreover, over 113 billion m^3 of untreated wastewater is discharged annually into natural water bodies, further exacerbating global water scarcity and pollution. Lignin accounts for 15–30% of lignocellulosic biomass and contributes more than 60% of its carbon content. It has emerged as a promising precursor for advanced carbon materials. Globally, over 100 million tonnes of lignin are generated annually by the pulp and paper industry, yet 98% is still underutilised or combusted for low-value energy recovery. This review critically summarises recent advances in the conversion of lignin into porous, heteroatom-doped carbon materials *via* thermochemical routes, including pyrolysis, hydrothermal carbonisation, and chemical activation. Lignin-derived carbons exhibit exceptionally higher surface areas (1700–2285 $m^2\ g^{-1}$), tunable pore structures, and rich surface functionalities, enabling efficient removal of heavy metals, dyes, pharmaceuticals, and oils. Furthermore, the adsorption capacities exceed 300 mg g^{-1} for organic pollutants, while lignin-based foams, aerogels, and sponges demonstrate oil absorption efficiencies greater than 20–40 g g^{-1} with excellent

[a]*Manipal Institute of Technology, Manipal Academy of Higher Education, Manipal, India. E-mail: ranjeet.mishra@manipal.edu*

[b]*Department of Mechanical Engineering, TKM Institute of Technology, Musaliar Hills, Karuvelil PO, Ezhukone, Kerala, 691505, India*

Sonal Vithoba Tarkar

Ms Sonal Vithoba Tarkar is a research scholar in the School of Civil and Chemical Engineering, Manipal Institute of Technology (MIT), Manipal Academy of Higher Education, Manipal, Karnataka, India. Her research focuses on the development of biochar through thermochemical and chemical modification routes for wastewater treatment. Her work particularly focuses on the removal of heavy metals, organic dyes, and pharmaceutical pollutants. Her research interests include biomass valorization, sustainable carbon materials, adsorption mechanisms, pyrolysis, surface functionalization, and green remediation technologies. Her growing research interest is in advancing renewable, low-cost, and environmentally sustainable materials for pollution control and water purification applications.

Anuradha K.

Ms Anuradha K. is a research scholar in the School of Civil and Chemical Engineering, Manipal Institute of Technology (MIT), Manipal Academy of Higher Education, Manipal, Karnataka. Her research focuses on the pyrolysis of lignocellulosic biomass and plastic waste to generate useful char materials for energy storage applications. She works on the thermochemical conversion and physicochemical characterisation of carbonaceous materials and their application as electrode materials for batteries and supercapacitors. Her interests include understanding structure–property relationships, charge storage mechanisms, and performance optimisation of waste-derived carbon materials. Through her research, she aims to develop sustainable, low-cost, and environmentally responsible energy storage solutions.

recyclability. Key adsorption mechanisms, including electrostatic attraction, π–π interactions, surface complexation, and pore filling, are systematically discussed. Furthermore, current challenges related to scalability, regeneration, and process economics are highlighted. Overall, lignin-derived carbon materials offer a low-cost, sustainable, and scalable solution for advanced wastewater treatment and oil–water separation, aligning closely with the principles of the circular bioeconomy and UN Sustainable Development Goals (SDGs 6, 12, and 13).

1. Introduction

Water is the foundation of life and a critical resource for human health, ecosystems, and socio-economic development. Although water covers nearly 71% of the Earth's surface, only about 2.5% constitutes freshwater, and less than 1.2% is readily accessible in rivers, lakes, and wetlands for direct human use.[1] Over 113 billion m^3 of untreated wastewater are released annually, severely impairing ecosystems and water quality, while the demand for freshwater worldwide is predicted to rise by 20–50% by 2050.[2] Consequently, water pollution has emerged as one of the most pressing environmental challenges worldwide. Industrial wastewater poses a significant environmental threat due to its complex mixture of heavy metals (Hg, Pb, Cd, As, Cr, Ni, Cu, Zn, Fe, and Mn), organic compounds, and chemical pollutants from industries such as textiles, leather, electroplating, mining, pharmaceuticals, and petroleum refining.[3] Oil spills represent another form of severe environmental contamination.[4] It was found that approximately 3.7 million tonnes of oil entered the ocean between 1970 and 2023, including 1.5 million tonnes from tanker accidents. These spills have destroyed vital habitats such as mangroves, coral reefs, and seagrass beds and suffocated marine organisms.[5] Emerging contaminants that are persistent and resistant to conventional methods, such as microplastics, PFAS, pesticides, and medicines, pose significant challenges for wastewater treatment. Fig. 1(a) highlights the environmental

Ranjeet Kumar Mishra

Dr Ranjeet Kumar Mishra is an Associate Professor in the School of Civil and Chemical Engineering at the Manipal Institute of Technology, Manipal Academy of Higher Education, India. He holds a PhD in Chemical Engineering and has over a decade of experience in academic and research roles, with a focus on sustainable materials, biomass valorisation, thermochemical conversion processes, and environmental remediation technologies. His research primarily focuses on biomass- and waste-derived carbon materials, including biochar, activated carbon, and functional carbons, for applications in wastewater treatment, the adsorption of emerging contaminants, energy storage, and oil–water separation. Dr Mishra has published 94 articles in high-impact international journals and has authored several review and research articles on pyrolysis, hydrothermal carbonisation, lignin valorisation, and circular bioeconomy approaches. His work integrates material synthesis, physicochemical characterisation, adsorption mechanisms, and process optimisation, with increasing emphasis on scalable and sustainable solutions. He has actively supervised doctoral and postgraduate research scholars and has contributed to funded research projects supported by national agencies. Dr Mishra serves as a reviewer for leading journals published by the Royal Society of Chemistry, Elsevier, Springer, and Wiley, and actively participates in academic outreach, faculty development programmes, and international conferences. His research aligns strongly with the United Nations Sustainable Development Goals related to clean water, sustainable materials, and climate action.

Mubarak Marutholi

Dr Mubarak M. is a dedicated academician and researcher with more than 15 years of experience in Mechanical Engineering, specialising in alternative fuels, bioenergy, and internal combustion engines. He presently serves as Vice Principal, Professor, and Head of Mechanical Engineering at TKM Institute of Technology, Kollam, where he plays a key role in academic administration, faculty development, and strengthening research initiatives. He completed his PhD at the National Institute of Technology, Calicut, with research focused on producing biodiesel from microalgae and aquatic weeds for diesel engine applications. He also holds a Master's degree in Automobile Engineering from Anna University, Chennai, where he was awarded the University Gold Medal. Dr Mubarak has published numerous high-impact research articles, presented papers at leading international and national conferences, and received competitive research grants from agencies such as SERB and KSCSTE. His research interests include algae-based biofuels, dual-fuel engines, renewable energy systems, and pollution reduction in the transportation sector. An active contributor to the academic community, he serves as a journal reviewer, editorial board member, conference session chair, and recognised PhD supervisor.

challenges posed by oil spills and industrial wastewater. Conventional wastewater treatment techniques are often expensive, energy-intensive, and less effective at removing low-concentration contaminants, whereas sophisticated membrane systems have complex maintenance requirements and are prone to fouling. The adsorption system is easy to use and highly effective, making it an affordable alternative. However, the high price of commercial activated carbon has led to the emergence of inexpensive, sustainable carbon compounds derived from biomass that are potential substitutes.[6]

Lignin is a promising biomass resource for carbon materials, serving as a significant natural source of aromatic monomers and the second-most prevalent biopolymer after cellulose. About 15% to 30% of plants contain lignin, an amorphous, three-dimensional polymer composed of *p*-hydroxyphenyl, guaiacyl, and syringyl units that provides a rich supply of functional groups and aromatic carbon.[7] The pulp and paper industry produces over 100 million tonnes of lignin annually, yet about 98% is burned as low-value fuel, with only 2% utilised for high-value applications.[8,9] Its aromatic structure and functional groups (phenolic, aliphatic hydroxyl, carboxyl and methoxyl) make lignin an excellent precursor for carbon materials and pollutant adsorbents. Thermochemical conversion methods such as hydrothermal carbonization, pyrolysis followed by activation using KOH, K_2CO_3, $ZnCl_2$, H_3PO_4, and $FeCl_3$ produce lignin-derived carbons with high surface areas (1700–2285 $m^2\ g^{-1}$), hierarchical porosity and tunable surface chemistry, comparable to or even surpassing those of commercial activated carbons.[8,10] The process of turning lignin, a low-value byproduct, into high-performance adsorbents minimises industrial waste and reduces reliance on petrochemicals. Recent studies have demonstrated the exceptional potential of lignin-derived carbons for removing a wide range of pollutants, including heavy metals, dyes, pharmaceuticals, and oils. Adsorption capacities exceeding 300 mg g^{-1} for organic pollutants have been reported, highlighting their competitiveness with conventional adsorbents. In addition to powdered carbons, lignin has been engineered into advanced macroscopic architectures, including foams, aerogels, sponges, and membranes. These materials exhibit high porosity, hydrophobicity, mechanical stability, and oil absorption efficiencies of 20–40 g g^{-1}, making them particularly attractive for oil–water separation and spill remediation.[11] Importantly, lignin's renewable origin and waste-derived nature align closely with circular bioeconomy principles and sustainability goals.

Past research on lignin-derived carbon materials mainly demonstrated proof-of-concept synthesis and adsorption under ideal laboratory conditions, typically using single, high-concentration model pollutants.[8,10] Such approaches offer a limited understanding of real wastewater systems and often overlook lignin source variability arising from different pulping methods, biomass origins, and molecular heterogeneity. Recent advances include heteroatom doping, hierarchical pore design, and lignin-based foams, aerogels, and composites with enhanced adsorption and separation performance. Nevertheless, the major gaps between lignin structure, extraction chemistry, and carbon performance remain unclear, while long-term regeneration, stability, and fouling resistance are rarely assessed. Moreover, scalability, techno-economic viability, life-cycle impacts, and performance under realistic multi-contaminant conditions also remain largely unexplored. Dong *et al.* (2023) examined the various pollutants using biochar in aquatic systems, with an emphasis on adsorption performance and the underlying processes for distinct types of contaminants. However, the review did not examine lignin extraction techniques and the impact of lignin-derived biochar precursors on surface chemistry and porosity.[12] Further, Zhang *et al.* (2023) studied the biomass-based porous absorbents for oil/water separation and reported that oil absorption capacities of up to 50–150 times their weight for cellulose-derived aerogels, water contact angles of 135–156°, and surface areas up to 2262.93 $m^2\ g^{-1}$ after activation, enabling quick uptake of oils and organic solvents with strong recyclability over 5–40 cycles.[13] However, these studies do not combine the chemistry of lignin, carbon material synthesis pathways, adsorption processes, oil–water separation efficiency, and environmental applications into a cohesive framework. By combining these disparate fields into a comprehensive review, the present study closes the gap and presents lignin-derived carbons as sustainable, high-performance materials for pollutant adsorption and oil–water separation technologies. Additionally, most studies focus on single-pollutant systems under ideal laboratory conditions, with limited attention to the complexity of real wastewater, regeneration performance, and long-term stability. Addressing these challenges requires a comprehensive understanding of structure–property–performance relationships and the development of scalable, cost-effective production strategies.

Therefore, this review critically examines recent progress in lignin-derived carbon materials for pollutant removal and oil–water separation, focusing on synthesis routes, structural features, and water treatment performance. It systematically evaluates the effects of lignin source, extraction and pretreatment methods, and thermochemical conversion pathways, including pyrolysis, hydrothermal carbonisation, and activation on pore structure and surface chemistry. The review also elucidates key adsorption and separation mechanisms for heavy metals (HMs), dyes, pharmaceuticals, and oils, and compares lignin-derived carbons with conventional activated carbons, highlighting advantages and limitations. Finally, it identifies challenges related to scalability, regeneration, and economic viability, and outlines future research directions to support practical implementation in sustainable water treatment systems. This article primarily reviews studies published over the past decade, with a limited number of earlier works included to provide essential background and continuity.

2. Fundamentals of lignin

2.1. Structure and chemical composition of lignin

The polymerisation of monolignols, primarily *p*-coumaryl alcohol, coniferyl alcohol and sinapyl alcohol, produces lignin, which is a complex three-dimensional amorphous aromatic polymer. The 3 primary structural units are produced when these monolignols polymerize. These are *p*-hydroxyphenyl (H)

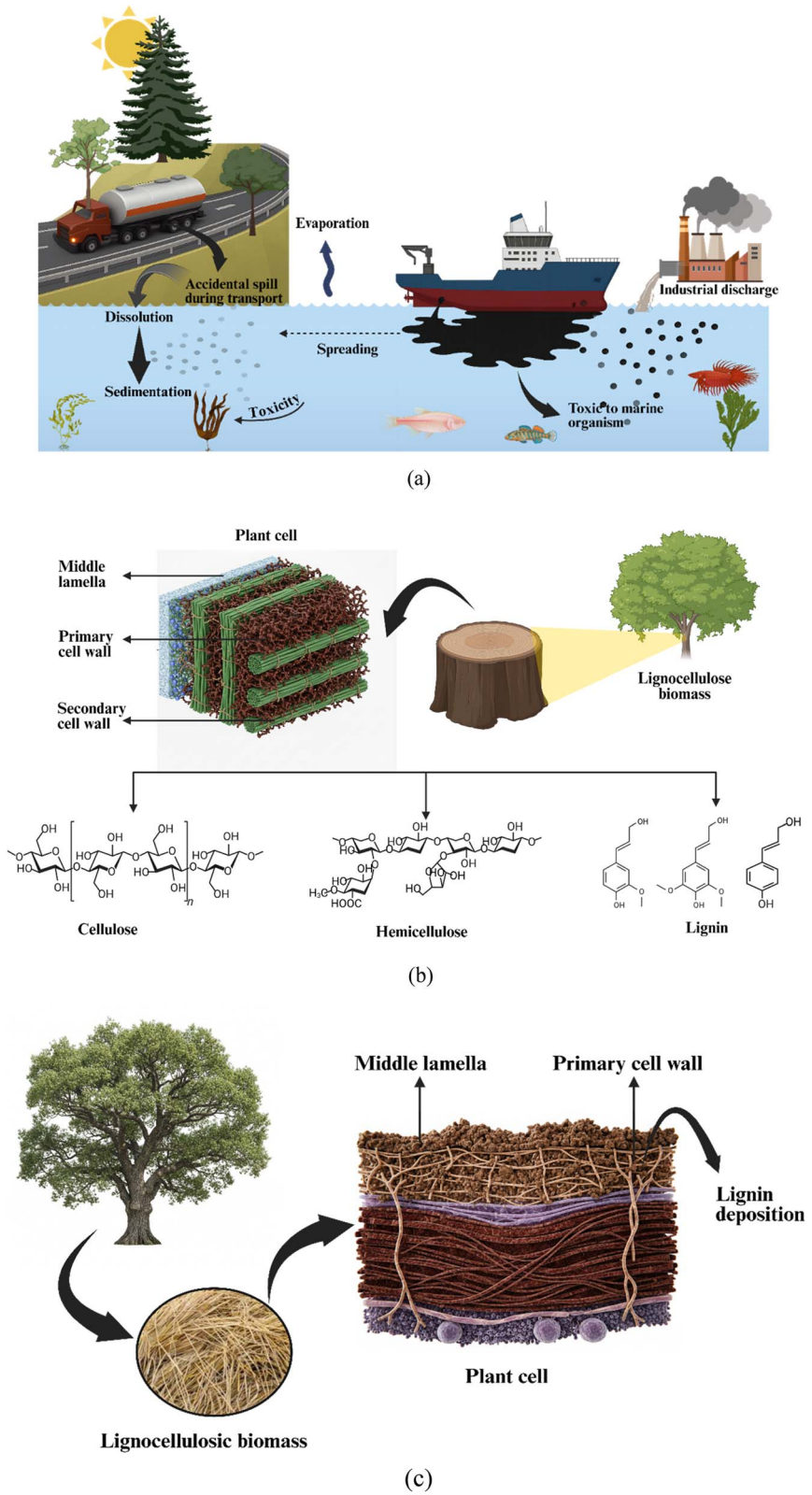

Fig. 1 (a) Environmental challenges from oil spills and industrial wastewater. (b) Schematic representation of the hierarchical structure and chemical composition of lignocellulosic biomass. (c) Lignification process in plant biomass.

units (derived from *p*-coumaryl alcohol), guaiacyl (G) units (derived from coniferyl alcohol) and syringyl (S) units (derived from sinapyl alcohol).[14,15] The cross-linking density, chemical reactivity, and functional behaviour of lignin are determined by the relative amounts of these H, G, and S units, which vary among plant species and tissues. Since guaiacyl (G) units free

the C5 position, they allow to produce more C–C bonds, which results in a more condensed structure that raises the lignin cross-linking density. As a result, hardwood lignin (LHSL), which has a lower G concentration (24–32%, DC about 24%), exhibits a lower degree of condensation (DC about 38%) than softwood lignin (LSSL), which has a higher G content (75–92%).[16] Despite occupying the C3 and C5 positions, methoxyl groups inhibit the formation of C–C bonds and prefer ether connections; thus, syringyl (S) units resist condensation. Although syringyl-derived compounds break down more easily, hardwood lignin can attain maximal phenolic aldehyde yields faster than softwood lignin due to this structural difference, which makes S-rich lignin more chemically reactive during oxidation. These differences demonstrate how the proportion of H/G/S regulates lignin cross-linking and reaction.[16] In terms of structure, lignin is composed of phenylpropanoid (C3–C3) units linked by a variety of carbon–carbon (C–C) and ether (C–O–C) bonds, forming an irregular, highly branched polymer network. Lignin's mechanical strength, stiffness, and resistance to chemical and biological deterioration are influenced by its heterogeneous, cross-linked structure.[14,17] Lignin is primarily made up of atoms of carbon (C), hydrogen (H) and oxygen (O) organised in aromatic phenylpropanoid units. The 3 fundamental monolignols, *p*-coumaryl alcohol, coniferyl alcohol and sinapyl alcohol undergo oxidative polymerization to produce the *p*-hydroxyphenyl (H), guaiacyl (G) and syringyl (S) structural units, respectively. The variations in the quantity and location of hydroxyl (–OH) and methoxy ($-OCH_3$) groups on these unit aromatic rings are the cause of lignin chemical heterogeneity. The plant species and tissue type determine the proportions of H, G and S components. Softwoods are generally rich in G-units, hardwoods contain G and S units, and grasses contain all three (H, G and S) units.[18] Fig. 1(b) shows the schematic representation of the hierarchical structure and chemical composition of lignocellulosic biomass. The hierarchical structure of lignocellulosic biomass, showing cellulose microfibrils embedded in a hemicellulose–lignin matrix derived from wood. It also highlights that the plant cell wall components originate from trees and decompose into cellulose, hemicellulose, and lignin, which are key precursors for biofuel and bioproduct production.

2.2. Lignification process in plant biomass

Lignification is a fundamental biochemical process in higher plants that involves the polymerization of monolignols. It consists mainly of *p*-coumaryl, coniferyl, and sinapyl alcohols, forming a complex, 3D aromatic polymer known as lignin. Fig. 1(c) represents the lignification process in plant biomass. Lignin is mostly deposited in the SCWs of vascular tissues such as TEs. Oxidative enzymes like laccases and peroxidases catalyze the process by mediating the radical coupling of monolignols to make phenylpropanoid units.[19] Río *et al.* (2020) reported that the 3 main monolignols are derived from the phenylpropanoid biosynthesis pathway. They are *p*-coumaryl alcohol, coniferyl alcohol and sinapyl alcohol, which are oxidatively polymerised to produce lignin, which is a complex aromatic polymer. The enzymes include PTAL, C4H, 4CL, HCT, C3H, F5H, CCoAOMT, CCR, COMT, and CAD, which catalyse a series of hydroxylation, *O*-methylation and reduction processes.[20] The primary structural components of lignin, *p*-hydroxyphenyl (H), guaiacyl (G) and syringyl (S) units, are produced when these monolignols are carried to the cell wall. Therefore, they are oxidised by peroxidases and laccases, then polymerised *via* free-radical coupling. An irregular, non-template macromolecule forms through polymerisation, resulting in many inter-unit connections, primarily β-O-4 ethers, β-5 phenylcoumarans, and β–β resinols.[20]

Tobimatsu *et al.* (2019) describe lignin polymerisation as a combinatorial radical coupling that occurs in apoplast cell wall domains. Laccases (LACs) use molecular oxygen to oxidise monolignols released into the apoplast, while peroxidases (PRXs) use hydrogen peroxide. To extend the polymer *via* β-O-4, β-5, or β-β linkages, these oxidation systems generate phenoxy radicals that endwise couple with growing lignin chains. The chemical irregularity of lignin can be explained by the non-enzymatic nature of the process. This indicates that while enzymes determine the position and timing of polymerization, they are unable to regulate the precise bond formation. Different peroxidases and laccases localise to distinct wall regions, which provides spatiotemporal accuracy in lignin deposition during cell differentiation. The wall polysaccharides, which function as scaffolds to direct the synthesis of polymers, may have an additional effect on the structural organisation of lignin.[21] Simon *et al.* (2023) found that lignification in plant cell walls is extremely localised and dynamic. The study demonstrated that the content and activity of lignification zones differ across individual cells. However, lignin deposition occurs in specific wall regions, such as pits, the middle lamellae, and the secondary wall layers. Triple-click chemical labelling was used to instantly view active lignification sites. This shows that lignin production and polymerization are tissue-specific and developmentally controlled rather than evenly dispersed across the wall matrix.[14] Li *et al.* (2025) found lignification in Asparagus officinalis during storage and demonstrated that it is closely related to cell wall metabolism, ROS activity, and phenylpropanoid metabolism. The excessive ROS promoted oxidative polymerization of lignin monomers at higher temperatures (25 °C). Hence, increased enzymatic activity of 4CL, C4H and CAD accelerated monolignol production and deposition. In addition, ROS served as signal molecules that initiated secondary wall production, and increased tissue stiffness resulted from the cross-linking of lignin with cellulose and hemicellulose. On the other hand, storage at 4 °C successfully inhibited these metabolic processes, thereby postponing lignification and preserving product quality. This demonstrates the environmental stress, ROS management and phenylpropanoid enzyme activity, which interact to regulate the lignification process.[22] The transformation of woody and agricultural biomass into lignocellulosic material features the layered plant cell wall structure. It emphasises the organisation of cellulose, hemicellulose, and lignin, demonstrating that natural biomass is structured at the microscopic level and serves as a fundamental feedstock for bioenergy and biorefinery applications.[22]

2.3. Types of lignin

Lignin is the heterogeneous, three-dimensional aromatic polymer that binds cellulose and hemicellulose in plant cell walls. The different species have distinct native (protolignin) structures and interunit linkages (β-O-4, β-5, 5–5, β–β, *etc.*).[23] The grasses have more H units and greater phenolic diversity, hardwoods have higher S content, and softwoods are G-rich.[24] Native lignin is very different from industrial and technical lignin, which are characterised by the extraction/process used. Kraft lignin (from kraft/sulfate pulping), lignosulfonates (from sulfite pulping), organosolv lignin (from organic-solvent extraction) and milled-wood lignin (MWL, a lab isolate that approximates native structure) are common technical varieties. Each class exhibits unique MW distributions, functional-group profiles (methoxy content, phenolic *vs.* aliphatic OH), sulfur content (particularly in kraft lignin) and degree of condensation.[25] All of which influence reactivity and suitability for valorization into chemicals, fuels or materials. Technical lignin is more condensed and chemically diverse than native lignin, due to the extraction chemistry driving condensation and demethoxylation processes that decrease β-O-4 content and increase carbon–carbon bonds. Prior to selecting downstream conversion or modification routes, lignin utilisation requires assessing the source species and isolation method, as process history and feedstock influence features.[26] Table 1 compares the effects of lignin derived from different sources on its chemical characteristics and applications.

2.3.1. Kraft lignin. Kraft lignin is the technical lignin that is produced and mostly dissolved during the kraft (sulfate) pulping of wood, where strong alkaline (NaOH) conditions are used. However, hydrosulfide conditions cleave many ether linkages and solubilise lignin fragments into black liquor. Currently, the majority of kraft lignin is burned in recovery boilers for energy and chemical recovery, though it is also extracted for valorisation.[25] Jiang *et al.* (2023) characterised 7 mixed hardwood kraft lignin samples from different regions using chemical and spectroscopic techniques. They measured lignin purity (86–96%), methoxy content (0.85–1.20 per C9 unit), MW (1895–4800 Da), aliphatic hydroxy groups (14–25 per 100 C9), phenolic hydroxy groups (65–112 per 100 C9), catecholic groups (12–34 per 100 C9, significantly higher than softwood lignin) and sulphur content (0.5–2.2%, organically bonded). The study revealed that the origin of wood species and processing method strongly influence the structure of hardwood kraft lignin. Thus, the native lignin linkages were severely degraded during pulping and replaced by new condensation products, such as stilbenes and biphenyls.[24] Resende *et al.* (2024) used a factorial experimental design with 19 reactions that varied temperature (120–160 °C), time (5–15 h), imidazole (0.04–0.13 mol) and succinic acid (0.35–0.69 mol) to systematically modify softwood kraft lignin with succinic acid. The glass transition temperature dropped from 183.3 °C to 118.5 °C, and 0.73 mmol g^{-1} of new succinic acid groups were incorporated. However, the polydispersity index decreased from 11.31 to 8.96, and the maximum weight-loss temperature (shifted from 400 °C to 500 °C) was observed under ideal conditions (160 °C) for 5 h with 0.13 mol imidazole and 0.35 mol succinic acid. The spectroscopic analysis verified successful esterification with 78.2% aliphatic hydroxyl conversion and 54.20% phenolic hydroxyl conversion. Thus, indicating the efficiency of succinic acid modification in plasticising and enhancing the thermal properties of lignin for possible uses in lignin-based resins and carbon fiber precursors.[34]

Argyropoulos *et al.* (2023) conducted a comprehensive review of kraft lignin as a sustainable resource from pulp production. Over 70 million tonnes of lignin are available in black liquor, and a large mill could extract about 450 000 tonnes of lignin yearly. They reported that approximately 170 million tonnes of

Table 1 Effect of lignin source on chemical characteristics and applications

Type of lignin	Chemical characteristics	Properties	Processing notes	Applications	Reference
Kraft lignin	MW = 2480 g mol^{-1}, phenolic OH 4.29 mmol g^{-1}, low β-O-4/β-5 bonds, S about 1–3%	High thermal stability, alkaline soluble	pH fractionation for MW control	Used in epoxy thermosets, carbon fibers	27
Organosolv lignin	Mw 500–3000 g mol^{-1}, β-O-4 40–60%, S-free, purity >95%	High reactivity, organic soluble	Microwave-assisted, solvent recovery	Used in 3D printing resins, nanocomposites	28 and 29
Soda lignin	Phenolic OH > 4 mmol g^{-1}, β-O-4 20–40%, S-free, MW 1500–4000 g mol^{-1}	Good dispersibility, reactive	Alkaline pretreatment of birch residue	Used in bio-composites, compatibilisers	30
Lignosulfonates	Sulfonated (sulphur 3.5–8%), water-soluble, high MW (140 Da)	Excellent dispersant and binder properties	Sulfonation post-extraction	Used in cement additives, binders, and dye formulations	31
Hydrolysis lignin	Highly C 65–75% condensed, heterogeneous, low solubility	High carbon content; suitable for energy recovery	Acid hydrolysis impurities	Used in biochar, activated carbon, and biofuel production	32
Enzymatic lignin	β-O-4 50–70%, MW 2k–5k, native structure	Retains natural structure, good for analytical studies	Enzyme optimisation for low yield	Applied in lignin model studies and green material synthesis	33

kraft pulp are produced each year globally. The study described the molecular characteristics of kraft lignin, which included a weight-average MW of 1700–6000 Da. A branching degree of around 84% and very few native β-O-4 linkages (2–8 per 100C9 units), which were substituted by biphenyl and stilbene structures. They examined 3 commercial isolation technologies (LignoBoost, LignoForce and SLRP). Thus, assessed applications such as gasification that achieved >99% carbon conversion, polyurethane systems with tensile strength of 33.0 MPa. Young's modulus of 176.4 MPa and phenol-formaldehyde resins with 60% phenol replacement, demonstrating superior adhesive performance.[25] Kraft lignin is an abundant industrial-scale aromatic feedstock with a large potential for conversion into chemicals and materials. However, its widespread valorization requires addressing two related issues: (1) controlling and characterizing feedstock and extraction variability (species, pulping severity, precipitation method) as these determine MW and functional-group inventory and (2) selecting targeted chemical or fractionation strategies (mild depolymerization, selective functionalization like succinylation) that compensate for condensation and heterogeneity while remaining economically compatible with mill recovery limits.[24,34]

2.3.2. Organosolv lignin. Organosolv lignin is a promising sustainable substitute for materials derived from fossil fuels. The most prevalent natural aromatic source and the second-most prevalent carbon source after cellulose is lignin.[35] The organosolv approach, unlike conventional technical lignin methods, produces high-purity, sulfur-free lignin. This result is achieved by gradually breaking down and modifying lignin macromolecules. This takes place under reaction circumstances using organic solvent-water mixtures, leading to a much lower MW. Due to an increased degree of depolymerization and decreased susceptibility for condensation processes, organosolv lignin produced after organosolv fractionation often exhibits low MW and polydispersity in comparison to other technical lignins.[36] Tanis *et al.* (2025) used GVL-organosolv treatment to recover lignin from Norway spruce at different temperatures (140–180 °C), GVL concentrations (60–80%) and catalysts (phosphoric or sulfuric acid). To assess the recovered lignin's chemical composition and structure, they methodically examined various conditions and employed FTIR, SEM/FE-SEM, Py-GCMS, and NMR spectroscopy. Thus, the best results were obtained at 60% GVL and 180 °C, resulting in 78% delignification and 66% lignin recovery with a phosphoric acid catalyst. Due to its high β-O-4 linkage retention (46.66 per 100 aromatic units), which is significantly better than that of other technical lignins, like kraft and Alcell lignin. However, the recovered lignin demonstrated remarkable reactivity, making it ideal for high-value applications in biorefineries.[35]

Jasiukaitytė-Grojzdek *et al.* (2025) developed a sustainable water-based fractionation technique for organosolv lignin extracted at 140, 160, and 180 °C. The increased lignin depolymerisation at higher temperatures reduced the MW from about 11 kDa to 1 kDa and increased aromatic OH groups while lowering aliphatic OH groups. Significant structural changes were observed in the lignin fractions, especially in the β-O-4 linkages, which decreased rapidly at 180 °C. The adjustment of temperature and solvent content enabled this method to modify lignin characteristics for various uses.[37] Tanase-Opedal *et al.* (2022) found that adding organosolv lignin (40 wt%) to thermoformed pulp decreased water uptake from 192% to 123%. The increased stiffness, from 2960 to 3660 MPa, and density, from 939 to 1096 kg m^{-3}, were accompanied by a decrease in tensile strength, from 42.9 to 34.8 MPa. Lignin with a MW of about 3300 g mol^{-1} and a glass transition temperature of 146 °C filled the fiber pores, decreasing wettability and swelling. Starch coating lignin further enhanced its water resistance, producing contact angles greater than 90°, making it a suitable ingredient for environmentally friendly pulp packaging.[38] Park *et al.* (2019) showed that the lignin melting and agglomeration problems observed in fixed-bed reactors can be effectively addressed by the rotary kiln reactor (RKR) (Fig. 2(a)). Compared with the fixed-bed system (47.7 wt% char), the RKR operating at 773 K yielded lower char (37.10 wt%) and higher bio-oil in the organic phase. The greater deoxygenation was also evident in the RKR char, which showed a noticeably higher carbon content (91.6%) and a lower oxygen content (2.5%). In contrast to the dense agglomerates that formed in the fixed bed, SEM pictures showed that RKR-derived char remained as a fine powder without expanding. Additionally, the gas composition varied: RKR pyrolysis produced less CO and C_4–C_4 gases and higher CO_2 (27 wt%), indicating that decarboxylation was the predominant process.[39] The specific extraction conditions enable the precise engineering of MWs (1–11 kDa) with adjustable characteristics. Organosolv lignin exhibits exceptional potential for a variety of applications, including the synthesis of carbon fibre and phenolic monomers.[37] Organosolv lignin has the potential to transition from laboratory innovation to industrial-scale reality by enhancing process intensification and optimising solvent recovery. This will significantly change the production of sustainable materials and reduce dependence on fossil fuels.[38]

2.3.3. Soda lignin. Soda lignin is a type of technical lignin that is mostly produced by alkaline pulping methods that use sodium hydroxide, commonly from non-wood biomass and agricultural leftovers.[23] It is reactive to chemical alterations due to its abundance of phenolic hydroxyl groups and its composition of aromatic monomers, including guaiacyl and syringyl units. Soda lignin is valued for its relatively high purity and its potential as a sustainable resource. Due to the production of bio-based adhesives, oleogels and photopolymerization initiators. However, lignin waste streams from the pulp and paper industry can be used to synthesise green materials.[40,41] Fig. 2(b) shows the lignin-phenol-formaldehyde (LPF) adhesive composed of lignin extracted from oil palm empty fruit bunch (OPEFB) fibre by the soda pulping method. Toma *et al.* (2022) isolated soda lignin with a 15% yield and a low ash concentration (0.93%) from oil palm empty fruit bunch fiber. They assessed the lignin structure and thermal stability using FTIR, ^{1}H NMR and TGA. Phenol was partially replaced by up to 50% of the phenol in phenol-formaldehyde adhesives with soda lignin. Significantly lower formaldehyde emissions (1.08 mg L^{-1} *vs.* 1.73 mg L^{-1}) and increased mechanical strength (tensile strength 2.6 MPa *vs.* 2.1 MPa for pure phenol) were found in

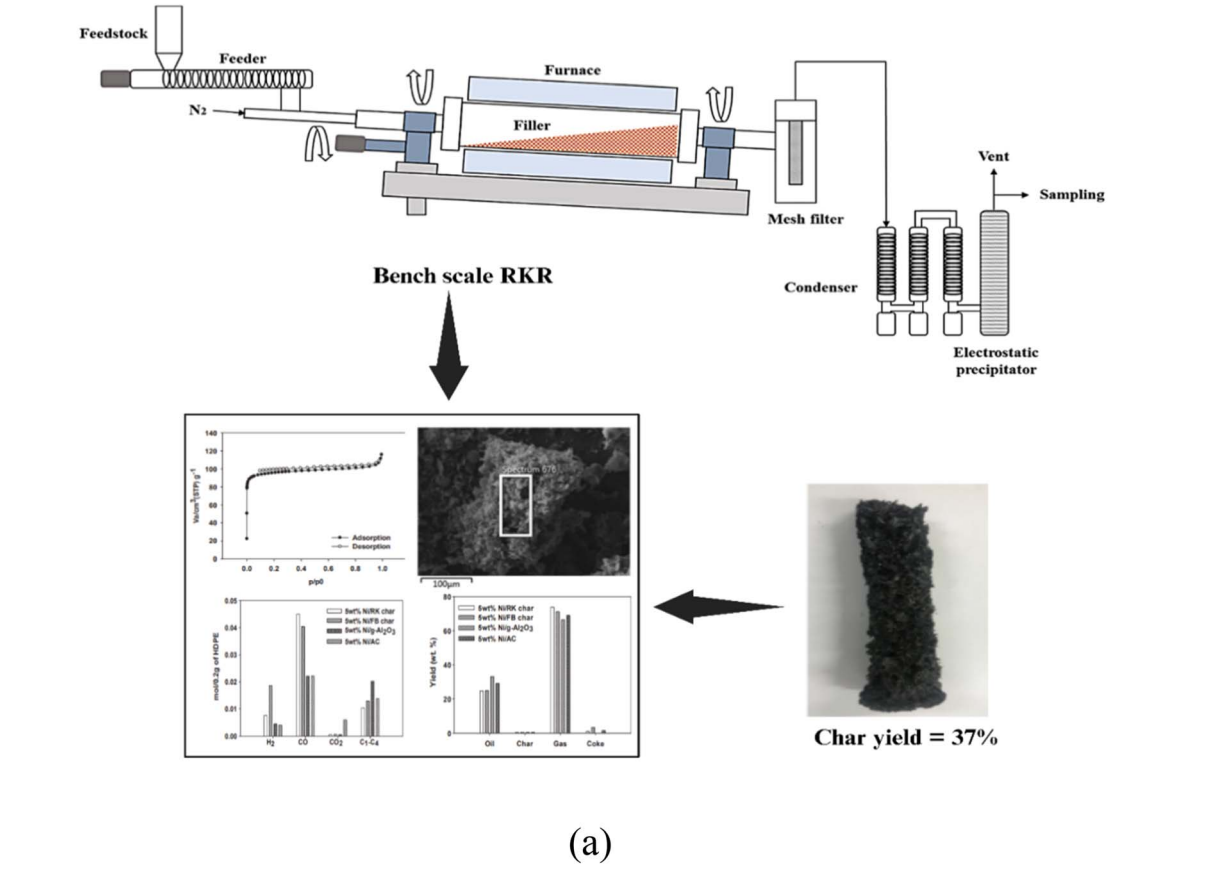

(a)

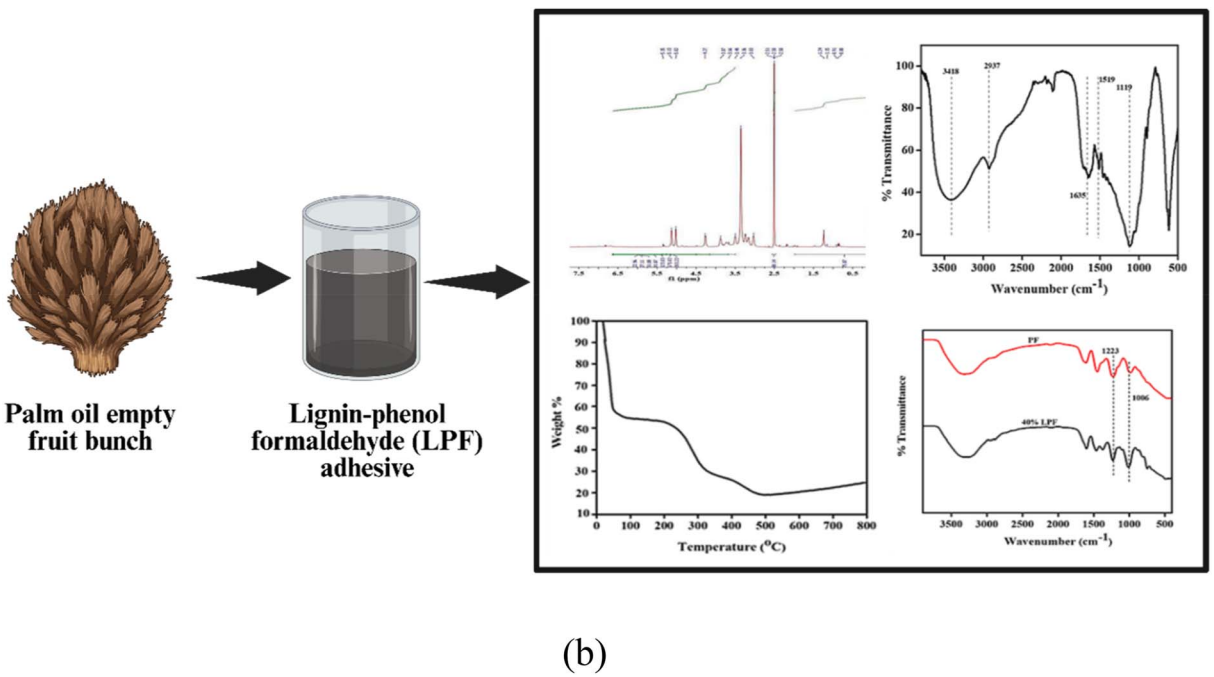

(b)

Fig. 2 (a) Schematic workflow of lignin pyrolysis and biochar formation in a rotary kiln reactor (redrawn from Park *et al.* (2019)[39]), (b) lignin-phenol-formaldehyde (LPF) adhesive composed of lignin, extracted from oil palm empty fruit bunch (OPEFB) fiber by soda pulping method (redrawn from Toma *et al.* (2022)[40]).

plywood bonded with 40% lignin. This indicates that soda lignin can be used as a sustainable co-monomer in adhesives.[40]

Moreover, Ruwoldt *et al.* (2024) investigated single-stage water extraction combined with two-stage treatments, including organic solvents and thermal treatments. They discovered that water washing was the most effective method, increasing acid-insoluble lignin to 91.40% and reducing ash content from 11.90% to as low as 0.10%. The low-MW components were removed using solvent treatments and cross-linking during calcination, thereby increasing the MW. Modifications in lignin structure were identified using UV/Vis and FTIR analyses, and a mathematical model was developed to more accurately estimate lignin concentration from FTIR data. In general, obtaining high-purity soda lignin appropriate for valorisation in chemicals and materials requires water washing.[42] Wang *et al.* (2025) prepared a liquid photopolymerizable macromonomer by modifying wheat straw soda lignin in a two-step process. They first oxyalkylated soda lignin to increase solubility and decrease viscosity. After that, they methacrylated it to add photopolymerizable groups. Despite a high lignin concentration (up to 41%), the final lignin-based methacrylate resin photopolymerized effectively, achieving a double-bond conversion of >80%. The material's potential as a sustainable, bio-based photopolymer for additive manufacturing was demonstrated by its effective use in 3D printing without the need for additional reactive diluents.[43] Soda lignin is a renewable biopolymer that is primarily purified by water washing. Its use in lubricants, adhesives and photopolymerization is enhanced by chemical changes.[42] Its molecular characteristics are improved by biological pretreatments. Therefore, it is a flexible substitute for materials derived from fossil fuels, strengthening phenol-formaldehyde adhesives and lowering emissions.[42]

2.3.4. Lignosulfonate lignin. Lignosulfonates are amphiphilic, water-soluble lignin derivatives that develop as byproducts of the sulfite pulping process. They have many sulfonic acid groups, which give them superior emulsifying, dispersing and binding capabilities. Their versatility has drawn interest for uses, including active food packaging, due to their UV-blocking, antibacterial, antioxidant, and mechanical reinforcing properties.[44] Khajeh *et al.* (2024) provided a thorough analysis of the application of lignosulfonate (LS) in soil stabilization. Its structure, physicochemical and geotechnical properties, and soil interaction mechanisms are emphasized. LS improves soil strength and stiffness by enhancing particle cohesion, decreasing soil erosion, and limiting the risk for swelling, they stressed. The LS treatment, for example, increased the UCS of fine-grained soils by up to 105% and granular soils by up to 450%.[45] Additionally, LS improves soil resilience under wet–dry and freeze–thaw cycles, enhancing practical engineering performance and providing an affordable, environmentally acceptable substitute for conventional stabilisers.[45] Wibowo *et al.* (2023) studied the thermal and chemical characteristics of ion-exchanged lignosulfonate by contrasting lignosulfonic acid (H-LS) with sodium lignosulfonate (Na-LS). Through ion exchange, they converted Na-LS to H-LS, reducing ash content by 92% (from about 18% to about 1.4%) and increasing the MW due to hydrogen-bonded aggregation. According to ^{31}P NMR and HSQC NMR, they found that H-LS had fewer phenolic –OH groups but more polymeric chains and sulfonated β-O-4 linkages than Kraft lignin. Thermal analysis revealed that H-LS, which was likely catalysed by acidic sulfonic groups, broke down more quickly than Na-LS and exhibited a higher glass transition temperature (T_g). These findings demonstrate the unique thermal and structural behaviour of H-LS which is crucial for its industrial uses.[46] The ability of lignosulfonates to improve mechanical strength, oxygen and water vapour barrier qualities, antioxidant activity and antimicrobial effects in composite films for food packaging, prolonging shelf life and preserving food quality.[44]

2.4. Physicochemical characteristics affecting carbon production

Lignin is a common aromatic biopolymer and a viable renewable precursor for carbon compounds due to its high carbon content and renewability. Carbon production and quality during carbonisation and activation are significantly influenced by lignin's physicochemical parameters. The physicochemical parameters include its MW, elemental composition, thermal degradation behaviour, and structure. The performance of the resulting carbon materials is determined by factors that impact lignin decomposition pathways, porosity development, surface area and crystalline structure. These factors include pyrolysis temperature, activation agents (such as $ZnCl_2$), and the extraction method (such as deep eutectic solvents). Higher carbonisation temperatures usually increase microporosity and fixed carbon content, but they also decrease yield because of increased volatilization.[47] Yu *et al.* (2024) investigated the physicochemical characteristics of biomass that influence the formation of HTC carbon, observing that cellulose (35–50 wt%) breaks down at 210 °C, hemicellulose (25–30 wt%) at 180 °C, and lignin (15–30 wt%) at 260 °C. VM (69–87%), FC (6–25%), and carbon content (45–53 wt%) affect yields ranging from 28.6% to 79.90%. The hydro-char carbon content increases while H/O drops, producing primary hydro-char from cellulose/lignin solids and secondary spheres *via* liquid repolymerization. The temperature increases aromatisation/pore volume but decreases yields (46.9–35.5% for brewers' spent grain, 180–250 °C). Moreover, the pressure (up to 20 MPa) increases C–H activation by reducing cellulose degradation to 117 °C; yields and porosity are impacted by BW ratios, with severity (Ro) being correlated with degradation rates.[48] Salcedo-Puerto *et al.* (2024) utilised hydrothermal carbonisation (HTC) at 200–240 °C, with residence times of 3–24 h and process water recirculation rates of 40–80%, to investigate the physicochemical properties of hydro char produced from industrial kraft lignin. At 240°C/12 h, ash content decreased by 75% to 0.32–0.53 wt%, volatile matter decreased by 13.2% to 61.6 wt%, and fixed carbon peaked at 38.0 wt%. Due to the recalcitrance of lignin, mass yields remained high at 85–97% while carbon content reached 66 wt% and HHV increased to 27.89 MJ kg^{-1} at 240°C/6 h. Temperature caused carbonization through dehydration and decarboxylation; recirculation increased yields (79–86%) but decreased

fuel ratios (0.42–0.62); H/O decreased with sulphur steady at 1.6–2.3 wt%.[49]

In addition, the degree of graphitisation, the development of the pore structure, and the chemical functionalities generated control the carbon's reactivity and adsorption capacity. Therefore, it is crucial to optimise these lignin physicochemical properties to produce high-performance, sustainable carbon products for a variety of applications.[50] The degree of graphitisation, pore structure evolution and chemical functionalities all affect the carbon's reactivity and adsorption. To develop high-performing, sustainable carbon materials for diverse applications, it is essential to optimise lignin's physicochemical properties.[50]

2.5. Availability and industrial valorisation potential

Lignin makes up 15–30 wt% of lignocellulosic biomass and up to 40% of its energy content, which is the second most common natural polymer on earth after cellulose. It serves as a structural binder, providing plant cell walls with their stiffness, impermeability, and resistance to microbial attack. An estimated 100 million tons of lignin are produced each year globally, primarily from the pulp and paper sector and second-generation bioethanol plants.[51] Less than 2% of technical lignin is used for high-value applications, despite its abundance; the remainder is burned on-site for energy recovery, resulting in an underutilization of its chemical potential.[52] Kylili *et al.* (2023) reported that lignin constitutes 30–34% of black liquid from the Kraft pulping process, which yields 1.7–1.8 tons of black liquor every tonne of pulp and around 30% of the organic carbon on earth. In addition to its wide industrial availability, it is a crucial feedstock for producing value-added goods such as carbon fibres, biochar, vanillin, and bio-oil. Thermochemical processes can cut CO_2 emissions by up to 99%, while lignin-based carbon fibers use 5% less energy and emit 22% less greenhouse gases than petroleum-based fibers. Despite its potential, lignin is challenging to value on large-scale due to its complex structure and energy-intensive processing requirements.[53]

Ahmad *et al.* (2023) studied the potential of lignin as a renewable feedstock and found that it comprises 15–20% of lignocellulosic biomass, with the pulp and paper industry producing 50–70 million tonnes of lignin annually worldwide. They suggested that as bioethanol production increases, it may reach 225 million tonnes annually by 2030. The study highlighted that lignin's carbon-rich content and aromatic structure make it suitable for converting into high-value compounds, biofuels, and bioplastics. To fully realise its industrial valorisation potential, they identified obstacles, including low monomer yields and considerable structural variability. Also, emphasising the necessity of effective depolymerisation procedures and integrated biorefinery techniques.[54] Alherech *et al.* (2021) showed that lignin may be valued by oxidative alkaline depolymerization of Cu-AHP pretreated poplar lignin, yielding about 30% aromatic monomer. The procedure yielded useful chemicals, including vanillin, syringaldehyde, and vanillic acid, which were effectively separated with over 95% purity and 80–91% recovery using centrifugal partition chromatography. The enormous industrial potential of lignin as a renewable supply of valuable aromatic compounds is highlighted in this study.[55] Lignin aromatic nature and accessibility make it a promising renewable feedstock for sustainable industrial processes. However, to fully realise its potential for bioeconomy valorisation, problems with its heterogeneity and with process optimisation need to be addressed.[56] Fig. 3(a) illustrates industrial availability and valorisation potential of lignin as a renewable feedstock. It highlights the large-scale industrial availability of lignin, which is primarily from the pulp and paper and biorefinery industries. This emphasises its status as an abundant and underutilised renewable resource. It also illustrates the various valorisation pathways through which lignin can be converted into high-value products such as biochar, carbon fibres, bio-oil, and aromatic chemicals. This demonstrates lignin's significant potential for sustainable material production, waste valorisation, and for advancing the circular bioeconomy and low-carbon technologies.[51]

3. Lignin extraction and pretreatment

3.1. Conventional extraction processes

The fundamental basis of technological lignin recovery from lignocellulosic biomass remains conventional lignin extraction methods, such as the kraft, sulfite, soda/alkaline, and organosolv processes. By cleaving lignin-carbohydrate and ether linkages under specific chemical conditions (alkaline, acidic, and solvent-based), these techniques separate lignin from cellulose and hemicellulose.[58] For example, the kraft method dissolves lignin in an alkaline sulfide solution, producing sulfur-rich, structurally condensed and less reactive lignin.[59] The sulfite process, uses bisulfite salts at pH values ranging from acidic to neutral to produce water-soluble lignosulfonates with sulfonate functionality and comparatively less condensation.[60] The soda or alkaline process, which uses NaOH alone (usually for non-wood biomass), avoids sulfur impurities and produces a purer lignin stream; however, it remains susceptible to some condensation in highly alkaline conditions.[32] To eliminate lignin with higher purity, lower MW, and preservation of β-O-4 bonds, the organosolv process uses organic solvents (such as ethanol and acetic acid), often with catalysts, at moderate heat, which makes the product more suitable for high-value applications.[61] A common problem with all these methods is that the extraction conditions (temperature, pH, solvent/chemical load) drastically change the isolated lignin chemical structure (fewer aliphatic hydroxyls, more phenolic groups, increased condensation), which affects downstream valorisation.[59] Fig. 3(b) illustrates the extraction processes, including sulfate (Kraft), sulfite, organosolv, and soda pulping. A comparative summary of lignin extraction, fractionation, purification, and modification strategies, along with their structural characteristics and outcomes, is presented in Table 2.

3.1.1. Kraft process. The kraft process is an alkaline pulping method based on a mixture of sodium hydroxide (NaOH) and sodium sulfide (Na_2S). It efficiently depolymerizes and solubilises lignin from wood fibre matrices while largely preserving cellulose integrity. However, without additional

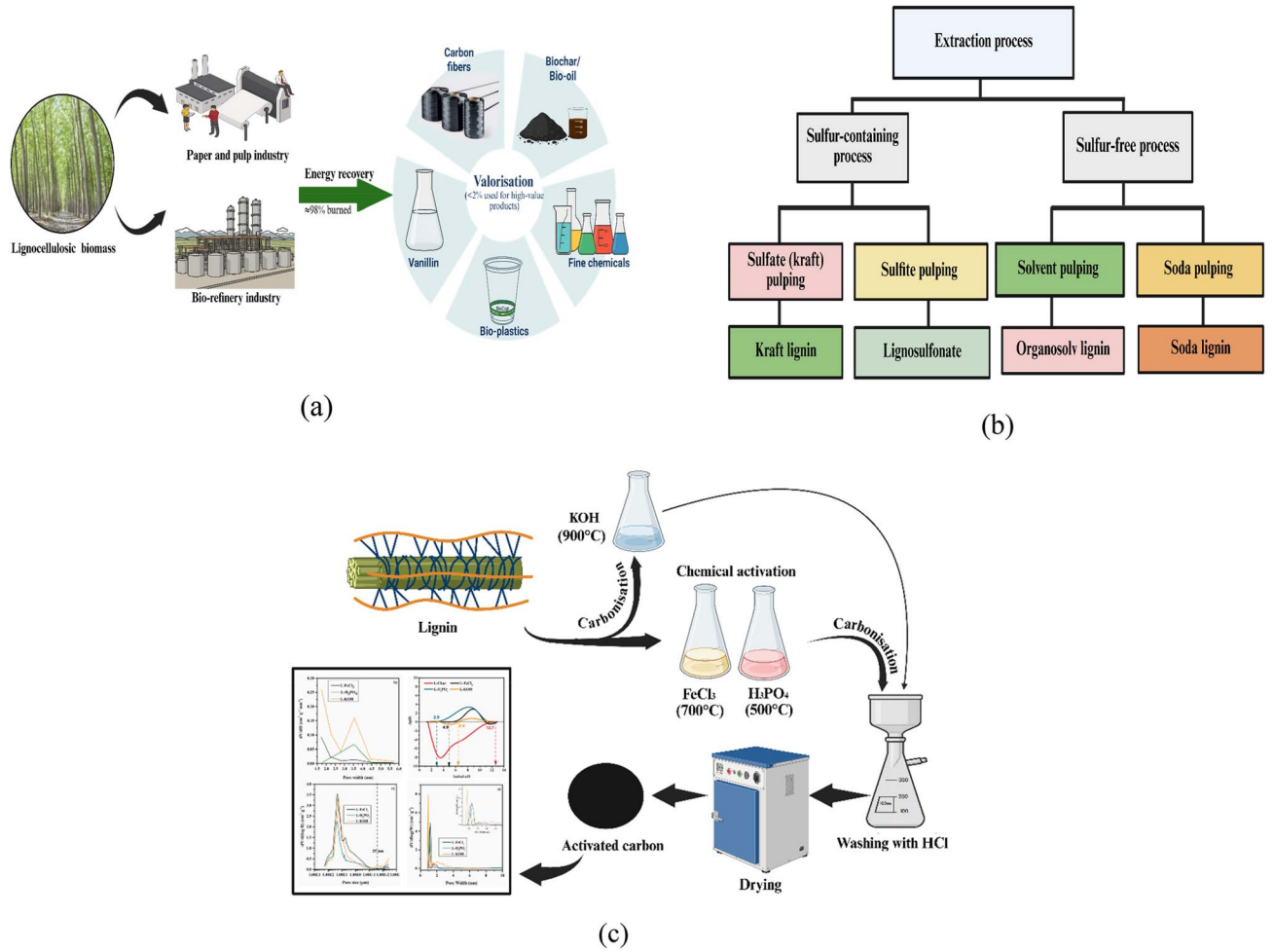

Fig. 3 (a) Industrial availability and valorisation potential of lignin as a renewable feedstock. (b) Extraction processes include sulfate (Kraft), sulfite, organosolv and soda pulping. (c). Schematic representation of lignin-based activated carbon preparation *via* chemical activation (redrawn from Álvarez-Montero *et al.* (2025)[57]).

modification, it produces a highly condensed lignin fraction that contains sulfur and exhibits decreased chemical reactivity, making it less suitable for high-value applications.[73] Lahtinen *et al.* (2021) reported that β-O-4 links in lignin rearrange *via* radical reactions to form secoisolariciresinol (β–β) structures during kraft pulping at about 170 °C. The fatty acids that covalently bind to lignin increase from 4 to 7 mol%. Thus, resulting in the formation of new C–C bonds, decreased solubility and increased chemical stability of the residual lignin.[62] Lancefield *et al.* (2018) discovered a unique lactone condensation product that revealed a hitherto unknown homo vanillin-based condensation route developed during pulping in softwood kraft lignin. They demonstrated that most native β-O-4 ether bonds are broken and replaced with novel C–C condensed structures and synthetic lignin models, with the lactone motif being notably concentrated in lower molecular weight fractions. Furthermore, Kraft lignin undergoes ionic and radical-mediated processes that yield chemically stable ring structures. This makes the lignin less reactive and more recalcitrant during downstream valorization.[74] Henriksson *et al.* (2024) provided an in-depth review of the chemical processes. It involved kraft pulping, focusing on the production of sulfur-containing condensed structures in alkaline sulfide conditions and the cleavage of β-O-4 ether linkages, which make up 45–50% of native lignin. According to the study, 90–95% of lignin is eliminated during the bulk delignification stage, with the remaining 3–7% remaining as insoluble residual lignin due to condensation and cross-linking reactions. These results highlight how the kraft process effectively separates lignin from cellulose while causing structural changes that lower the solubility and reactivity of lignin.[73] The kraft process effectively eliminates lignin but produces a condensed, sulfur-rich and less reactive lignin, which restricts its direct use in complex applications.[62,74]

3.1.2. Sulfite process. In the sulfite pulping process, lignin is solubilised using bisulfite or sulfite salts in acidic to neutral environments to generate sulfonated, water-soluble lignosulfonates, which are useful for both pulp production and lignin valorization.[75] Kong *et al.* (2024) showed that in acidic conditions (pH < 4), reductive $SO_2^{\bullet-}$ radicals develop in the UV/sulfite process and transform into dithionite, thiosulfate, and H_2S. The elemental sulfur extends the use of sulfite chemistry for lignin

Table 2 Comparative summary of lignin extraction, fractionation, purification and modification strategies with their structural characteristics and outcomes[a]

Method/ process	Chemicals/solvent system	Operating conditions	Type of lignin obtained	Structural features	Outcomes	References
Kraft process	NaOH + Na_2S	150–170 °C, 2–3 h, pH > 13	Kraft lignin (sulfur-containing)	Highly condensed β-O-4	90–95% delignification, low reactivity	62
Sulfite process	Na/Ca/Mg/NH_4 bisulfite	130–180 °C	Lignosulfonate	Sulfonated, water-soluble	3–8 wt% S, used as dispersant	16
Soda (alkaline) process	NaOH	140–170 °C, 1–3 h	Soda lignin	Sulfur-free, reactive	92% delignification, 97% purity	63 and 64
Organosolv process	EtOH, MeOH, AcOH, HCOOH	160–200 °C, 1–2 h	Organosolv lignin	Low MW, rich β-O-4	74–90% delignification, 97% purity	65
Ionic liquid (IL) extraction	HSO_4, OAc	120–150 °C	ILs-derived lignin	Preserved β-O-4, S-free	85% delignification, phenolic OH = 4.6 mmol g^{-1}	66
Deep eutectic solvent (DES)	ChCl : LA (1 : 2)	120 °C, 4 h	DES lignin	Low MW = 2300 g mol^{-1}	84% delignification, high phenolic content	67
Membrane fractionation	Ultrafiltration (1–10 kDa)	Ambient	Fractionated lignin	Controlled MW, PDI <1.8	Phenolic OH 5.2 mmol g^{-1}, high uniformity	68
Purification	*n*-Butanol + H_2O + H_2SO_4	140–160 °C	Butanosolv lignin	β-O-4 = 67 per 100C9	>98% carbohydrate removal	69
Esterification (succinylation)	Succinic acid	100 °C, 6 h	Succinylated lignin	+COOH = 0.73 mmol g^{-1}	T_g 183–118 °C, better solubility	34
Oxidative modification	H_2O_2/Laccase	50–70 °C	Oxidized lignin	+38% COOH groups	Improved hydrophilicity, dispersion	70 and 71
Grafting modification	PEG/TOFA	80–100 °C	PEG/TOFA lignin	Solubility 85%	Tensile 8.7 MPa, polymer compatibility	72

[a] PDI = polydispersity index, PEG = polyethylene glycol, TOFA = tall oil fatty acid, Na_2S-sodium sulphide, HSO_4-hydrogen sulfate, OAc-acetate anion, AcOH-acetic acid, HCOOH-formic acid.

modification and pollutant degradation.[76] Cao *et al.* (2021) found that the UV/sulfite system breaks down halogenated chemicals and metals by acting as an advanced reduction and oxidation process (ARP/AOP) and producing hydrated electrons (e_{aq}^-) and $SO_3^{\bullet -}$ radicals with a reduction potential of roughly −2.9 V. When O_2 is present, the process changes to oxidation, producing $SO_4^{\bullet -}$ radicals.[77] Casimiro *et al.* (2022) conducted a comparative study of hardwood and softwood lignin recovered from sulfite liquors *via* ultrafiltration and freeze-drying. Later, followed by detailed structural characterisation and oxidative depolymerisation. They found that hardwood lignin (LHSL) had a higher β-O-4 linkage content (42 per 100 aromatic units) and a lower degree of condensation (24%) than softwood lignin (LSSL). As a result, it had a higher MW (48 566 g mol^{-1}) and greater condensation (38%) using methods such as nitrobenzene oxidation, 13C NMR, and GPC. LHSL produced mostly syringaldehyde (2.5% w/w) during alkaline oxidation with O_2 at 120 °C and 3 bar, whereas LSSL produced mostly vanillin (4.7% w/w). The study demonstrated that sulfite lignins are viable feedstocks for producing value-added compounds, such as vanillin and syringaldehyde. It also indicated that controlled oxidation could maximise phenolic monomer output.[16] Although the sulfite process effectively delignifies biomass and yields sulfonated, water-soluble lignosulfonates with superior dispersing and surface-active qualities. It also produces lignin with high sulfur content and structural modification, which limits its direct use in high-value applications.[75]

3.1.3. Soda/alkaline process. Sodium hydroxide (NaOH) is used in the sulfur-free alkaline delignification process known as "soda pulping". It is more environmentally friendly than sulfur-based techniques and especially appropriate for non-woody biomass.[63] Hawanis *et al.* (2025) enhanced a hybrid alkaline pulping of sugar palm fibers using 15% NaOH. This resulted in increased thermal stability (580 °C), 92% delignification, 2.8% increase in cellulose content and 29.18% increase in crystallinity index. The soda pulping is a practical and sustainable substitute for manufacturing paper from non-woody sources.[78] Allegretti *et al.* (2018) utilised a membrane-assisted ultrafiltration technique, and wheat straw soda lignin was separated into several MW fractions (1000–3500 g mol^{-1}). The intrinsic heterogeneity of soda lignin was demonstrated by the unique chemical composition, functionality and thermal behaviour of each fraction. Higher MW fractions demonstrated increased aromaticity and thermal stability, while lower MW fractions had higher phenolic hydroxyl content and improved solubility according to the study. By customising lignin reactivity and performance, this selective fractionation method supported the circular and sustainable valorisation of agricultural leftovers. Thus, it made it more suitable for application in biopolymer synthesis, polymer composites, and advanced organic materials.[63]

Shulga *et al.* (2025) examined the effects of alkaline pretreatment on birch sawdust and the properties of the soda lignin that was isolated from it. Compared to untreated samples, sawdust treated with 0.5% NaOH showed a significant decrease in hemicelluloses, a 25.5% increase in cellulose content, and a 5.7% increase in lignin production. A higher level of condensation and cross-linking was observed in the resultant soda lignin, as evidenced by the reduced phenolic hydroxyl and methoxyl groups.

Additionally, modified soda lignin (MSL) was successfully incorporated into bio-composites composed of recycled polypropylene (rPP), polylactic acid (PLA), and ammoxidized wheat straw. This replaced more than 30% of the synthetic compatibiliser without sacrificing mechanical properties. This shows immense potential to produce sustainable composites.[64] The soda method provides a sulfur-free, environmentally friendly, and efficient way to extract lignin, although it is less delignifying than the kraft process. Additionally, producing low-MW, reactive lignin with functional groups conserved suitable for use in biopolymers, composites, and green technologies.[64,78]

3.1.4. Organosolv process. The organosolv process is an effective, sulfur-free delignification method that separates lignocellulosic biomass into cellulose, hemicellulose and high-purity lignin. Organic solvents, including acetic acid, methanol, ethanol, or formic acid are commonly employed, often when combined with water and a catalyst. This produces lignin with low MW, little condensation, and no sulfur, making it ideal for the synthesis of carbon materials, resins, and biopolymers. The organosolv pretreatment provides cleaner recovery, better lignin quality. Additionally, simpler solvent recycling is achieved compared to kraft and sulfite methods; however, its higher cost and energy requirements remain issues.[79,80] Wei Kit Chin *et al.* (2020) provided a thorough explanation of the organosolv pretreatment process, highlighting its capacity to lower biomass recalcitrance while producing high-purity, sulfur-free lignin. They reported that under moderate settings (100–200 °C), organic solvents, including ethanol, methanol and acetic acid. They efficiently cleave β-O-4 ether bonds between lignin and carbohydrates, enabling delignification efficiencies of up to 85–90%. Due to its high hydrophobicity, low ash content (<0.1%) and minimal structural degradation, the recovered lignin is ideal for bioproduct applications.[80]

Parot *et al.* (2022) enhanced a catalytic organosolv process using ethanol for black spruce (softwood), achieving the highest reported total lignin recovery of 74% with 97% purity. Both lignin fractions had comparable structural characteristics, but the procedure yielded different densities and colours, conducted at 180 °C for 90 min using 5% $FeCl_3$ as a catalyst. The cellulose pulp was used to extract one lignin fraction, and residual liquid was used to precipitate the other. Since the lignin retained its β-O-4 structures and showed no condensation, catalytic organosolv pulping can recover high-quality lignin.[65] The organosolv process provides a clean, sulfur-free, and customizable approach for lignin extraction, yielding high-purity, low-MW lignin considering that its cost and solvent recovery continue to be significant challenges. In addition to maintained structural connections appropriate for chemical and high-value biopolymer applications.[80]

3.2. Advanced extraction and fractionation techniques

Advanced lignin extraction and fractionation techniques have emerged as sustainable substitutes for traditional pulping procedures. The intent is to recover lignin with high functional group retention, narrow MW distribution, and minimal structural damage. The selective delignification of lignocellulosic biomass is made possible by these methods which include membrane ultrafiltration, microwave-assisted extraction, ionic liquid (ILs) and deep eutectic solvent (DES) pretreatment, and sequential solvent fractionation. It preserves lignin natural β-O-4 bonds and phenolic hydroxyl properties.[81,82] Recent research suggest that technical lignin's molecular heterogeneity may be considerably reduced by controlled fractionation, producing reliable fractions that enhance material performance and reactivity.[68] For example, integrated biorefinery techniques and organic solvent fractionation have demonstrated up to 85–90% lignin solubilization, accompanied by enhanced homogeneity and thermal durability.[83] Additionally, the recovery of uncondensed, sulfur-free lignin is suitable for advanced polymer, resin, and carbon applications. Thus, made easier by gentle extraction techniques as those employing ionic liquids or green solvents.[84]

Abolore *et al.* (2025) indicated that a significant development in lignin isolation is the move toward ionic liquid (ILs) and deep eutectic solvent (DES) systems. This enables selective breaking of ether and ester bonds while maintaining native β-O-4 structures. For example, at relatively mild temperatures (120–150 °C), ILs like [Bmim][HSO_4] achieved >85% delignification, producing sulfur-free lignin with a high phenolic hydroxyl content (4.6 mmol g^{-1}). These features highlight the impact of solvent acidity and recyclability on lignin quality, making IL-derived lignin especially appropriate for polymer synthesis and functional materials.[81] Ponnuchamy *et al.* (2021) demonstrated that lignin heterogeneity can be further refined using solvent-based lignin fractionation. They produced fractions with regulated MWs (1200–4000 g mol^{-1}) and unique physicochemical features by sequentially extracting kraft lignin using more polar solvents. The highest β-O-4 linkage content (up to 40%) and increased solubility were retained in the methanol-extracted fraction. Thus, demonstrating that specific solvent selection can adjust lignin chemical reactivity and processability.[83] Pang *et al.* (2021) formed homogenous fractions with narrow MW dispersion (Mn/MW < 1.8) and retained hydroxyl functionalities by fractionating soda and organosolv lignin using membrane-assisted ultrafiltration. Higher-weight fractions exhibited enhanced thermal stability, whereas the low-MW fraction (<2 kDa) displayed a higher phenolic content (5.2 mmol g^{-1}). This illustrates the membrane fractionation supplements solvent extraction by offering scalable control over lignin structure and purity.[68] The recovery of sulfur-free, structurally preserved, and compositionally uniform lignin is made possible by sophisticated extraction methods. Additionally, fractionation techniques such as ionic liquids, deep eutectic solvents, and membrane-assisted processes are used. These techniques offer substantial advantages over traditional methods, opening the door to the high-value use of lignin in biopolymers, resins, and carbon materials.[81,82]

3.3. Purification and modification strategies

Lignin must be purified and modified to improve its chemical reactivity, homogeneity and suitability for advanced material applications. The crude technical lignin often contains impurities including ash, polysaccharides, and condensed structures, which

limits its value. Cleaner lignin with preserved structural bonds is obtained by purification methods such solvent washing, membrane separation, and organosolv purification. Later chemical reactions that give lignin new functional groups include esterification, oxidation, and grafting. As result, it becomes more soluble, flexible, and compatible with polymers, which makes it appropriate for use in coatings, biodegradable polymers, and bio-composites.[72] Zijlstra *et al.* (2021) found that lignin with remarkable purity and structural preservation may be produced using a semi-continuous butanosolv extraction with in-line purification. Their method produced lignin with a high β-O-4 content (67 linkages per 100 C9 units) and removed over 98% of the carbohydrates. These effective purifying techniques lay the groundwork for generating lignin that may be modified chemically and incorporated into polymers.[69]

Resende *et al.* (2024) introduced novel carboxylic groups (0.73 mmol g^{-1}) that improved polarity and processability by esterifying softwood kraft lignin with succinic acid. The glass transition temperature (T_g) dropped from 183 °C to 118 °C because of the change, suggesting increased molecular flexibility and the possibility of thermoplastic mixing.[34] Rahmani *et al.* (2024) demonstrated the use of long-chain oil fatty acids (TOFA) to functionalize lignin and incorporate it into polyvinyl alcohol-cellulose fibre bio-composites, which enhanced thermal stability and tensile strength (8.7 MPa). These results demonstrate how purification ensures chemical homogeneity and eliminates inactive residues, while targeted modification introduces reactive or flexible functional groups. Thus, changing lignin function from a complicated byproduct to a flexible bio-based polymer precursor appropriate for composites, coatings and high-performance materials.[72] Crude technical lignin must be purified and modified to become a reactive, consistent and valuable biopolymer. The chemical modifications, such as esterification, succinylation, and oxidative functionalization, introduce reactive groups that enhance solubility, flexibility, and compatibility with polymer matrices; they also require purification techniques. Techniques such as solvent extraction and membrane-assisted methods effectively eliminate impurities while preserving lignin's native linkages. Moreover, combining these strategies increases the use of lignin in bio-composites, coatings and cutting-edge sustainable materials. Thus, facilitating its incorporation into contemporary biorefinery and circular economy frameworks.[34,69]

4. Synthesis of lignin-derived carbon materials

4.1. Thermal conversion and carbonization mechanisms

Thermal conversion of lignin produces carbon-rich materials with adjustable porosity and surface chemistry through various carbonization processes. The processes that include depolymerization, fragmentation and aromatic condensation. This process typically begins at 200–300 °C, when lignin breaks down and cleaves ether and aliphatic bonds. It continues up to 900 °C when highly condensed aromatic structures with sp^2 and sp^3 hybridised carbons form, producing char with high carbon content and thermal stability.[49] Ischia *et al.* (2025) demonstrated that carbon spheres (180–220 nm) and graphene-like layers with a carbon content of approximately 72.50 wt% are formed during the hydrothermal conversion of lignin. The technique produces sophisticated carbon nanostructures using aromatic precursor condensation and thermal defragmentation, without the need for harsh chemicals.[85] Salcedo-Puerto *et al.* (2024) studied the hydrothermal carbonization of industrial kraft lignin and found that lignin degrades between 200 °C and 500 °C. Thus, producing hydro-char with up to 70% carbon and improved aromaticity. When compared to raw lignin, thermal examination revealed that hydro-char had greater thermal stability, indicating condensation and char production.[49] Lignin may be efficiently converted into carbon with high carbon content (up to 72.5 wt%), thermal stability, and customised porosity.[49,85]

4.2. Pyrolysis methods and temperature effects

The structural, chemical, and energetic characteristics of carbon compounds derived from lignin are significantly influenced by temperature and pyrolysis method. The customised functionality for energy storage, catalysis, and environmental remediation applications is enabled by optimising these conditions.[86–89] Song *et al.* (2025) found that while slow pyrolysis of alkaline lignin produced a lower yield (29%), it also produced a much higher specific surface area (up to 763 $m^2 g^{-1}$) and conductivity (15.94 S cm^{-1}). Due to more extensive aromatisation and graphitisation at higher temperatures and slower heating rates. As fast pyrolysis produced a much higher biochar yield (up to 52% at 1000 °C) and consumed minimal energy (0.0026 kWh).[90] Zhu *et al.* (2022) showed that lignin-based activated carbons with a BET surface area as high as 2149.50 $m^2 g^{-1}$ and capacitance of 300 F g^{-1} (at 0.5 A g^{-1}) were produced by fast pyrolysis (550 °C) of alkali lignin from the pulp/paper industry.[91] It was combined with KOH activation (800 °C), outperforming slow pyrolysis-derived carbons by about a factor of two in both pore development. However, fast pyrolysis yields were 22% lower than slow methods.[91] Li *et al.* (2023) studied the relationships between process and structure and found that while slow pyrolysis (same temperature, slow heating) maximises biochar yield (50 wt%) with high aromatisation, fast pyrolysis (≥500 °C, rapid heating) favours bio-oil (60–70 wt%). High temperatures and heating rates also significantly affect surface area, porosity, and carbon structure, which, in turn, influence the properties of lignin-derived carbon products.[92] The faster pyrolysis methods increase production rates but generally decrease biochar yield. Additionally, it enhances porosity, while slow pyrolysis maximises solid yield and aromatic condensation, thereby optimising electrical and adsorptive properties. The effective tuning of pyrolysis temperature and method is crucial for tailoring lignin-derived carbon materials for advanced applications.[90–92]

4.3. Hydrothermal carbonization

Hydrothermal carbonization uses aqueous-phase processes at high pressures and moderate temperatures to transform lignin

and biomass into carbon-rich compounds. This eco-friendly method makes it possible to produce carbon solids with adjustable porosity, surface chemistry and shape that are appropriate for use in energy and environmental applications.[85,93] Salcedo-Puerto *et al.* (2024) found that industrial kraft lignin hydro-char produced *via* hydrothermal carbonization (HTC) at temperatures between 200 and 260 °C reached carbon contents close to 70%. Thus, enhanced aromaticity and improved thermal stability are evidenced by shifts of decomposition peaks to higher temperatures.[49] Mao *et al.* (2018) produced lignin-based carbon spheres using HTC. While observing that when the processing temperature increased from 230 to 270 °C, the particle size increased from 2 to 3 μm. Surface area rose from 384 to 1278 m^2 g^{-1} using KOH activation and microwave treatment, suggesting better potential for environmental applications.[93] Ischia *et al.* (2025) found that lignin can be transformed into various carbon nanomaterials, including carbon spheres (180–220 nm), carbon dots, and graphene-like layers. Thus, by undergoing a two-stage hydrothermal process without the use of harsh chemicals. These materials have distinctive structural characteristics, including sp^2 and sp^3 carbon hybridisations, and a high carbon content of about 72.50 wt%. The complex aromatic polymer lignin is first hydrothermally cleaved into smaller units, which subsequently undergo condensation and aromatisation to generate carbon nanostructures. This process produces materials with customizable shape, high purity and potential uses in energy storage, environmental remediation, and catalysis.[85] HTC is a useful method to generate lignin-based carbons with improved carbon content, regulated morphology, and adjustable porosity; material qualities are mostly determined by process variables and pretreatments.[85,93]

4.4. Physical and chemical activation

Physical and chemical activation techniques are essential for enhancing lignin-derived carbons by increasing porosity, surface area and functional groups. The chemical activation uses chemicals such as KOH, $ZnCl_2$, and H_3PO_4 to form a highly developed pore network at comparatively lower temperatures. Physical activation often involves gasification with steam or CO_2 at high temperatures.[10,94] Cao *et al.* (2024) showed that lignin was chemically activated by K_2CO_3 at 800 °C, resulting in a BET surface area of up to 1723.8 m^2 g^{-1} and a phenol adsorption efficiency of 98.22%. Additionally, the method promoted the formation of functional groups containing oxygen, thereby improving material stability and adsorption capacity. Additionally, they noted that while rising temperatures promote the formation of micropores, overheating may cause pore collapse, thereby reducing porosity.[10] Kim *et al.* (2025) studied steam activation of pitch-based carbon fibres at 900 °C, producing activated carbon fibres (ACF) with a remarkably large surface area of 2564 m^2 g^{-1}. The ACF activated at 800 °C demonstrated a maximum CO_2 adsorption capacity of 4.32 mmol g^{-1} at 273 K. This was attributed to micropores with a diameter of approximately 0.73 nm, which enabled effective CO_2 uptake. With a low activation energy of 5.41 kJ mol^{-1} and adsorption kinetics fitting a pseudo-first-order model, the study demonstrated that physisorption dominated CO_2 adsorption.[94] Álvarez-Montero *et al.* (2025) produced lignin-based activated carbons with surface areas of 1389 m^2 g^{-1} and 1830 m^2 g^{-1}, respectively, through chemical activation using KOH and $ZnCl_2$. Due to the formation of microporous structures that promote adsorption kinetics, the KOH-activated carbon demonstrated a high adsorption capacity (50 mg g^{-1}) for nano-plastics. Fig. 3(c) illustrates a schematic representation of lignin-based activated carbon preparation *via* chemical activation. Lignin undergoes pyrolysis to form char, followed by simultaneous activations using KOH (900 °C), $FeCl_3$ (700 °C), and H_3PO_4 (500 °C), with subsequent HCl washing, drying, and yield of the final activated carbon product.[57] At lower treatment temperatures, chemical activation of lignin typically yields larger surface areas and micropore volumes compared to physical activation, thereby enhancing electrochemical performance and adsorption efficiency. To adjust pore size distributions and facilitate applications such as CO_2 capture, physical activation remains useful. The production of lignin-derived carbons suited to certain environmental and energy use, activation conditions must be modified.[10,94]

4.5. Heteroatom doping (N, S, P, O)

Heteroatom doping converts inert surfaces into active sites for improved heavy-metal adsorption *via* chemisorption and enhances selectivity by adding non-carbon elements (N, S, P, and O) to lignin-derived carbons.[95,96] Lan *et al.* (2025) examined heavy-metal ion adsorption on heteroatom-doped carbon nanotubes (CNTs), including N-, O-, B-, S-, and B–N-CNT variants, using density functional theory (DFT). Adsorption energies were increased by N- and O-doping (up to −11.10 eV for Co on N-CNT at hollow sites) and decreased by B- and S-doping, with hollow > top > bridge being the favoured sites. Driven by charge transfer and electrostatic interactions, the adsorption capacity followed the order of Co > Ni > Fe > Hg > Cu > Cd > Pb > Cr > As > Zn; tests verified that N-CNTs had better removal efficiency than pristine CNTs.[95] Hu *et al.* (2024) studied the adsorption of three lignin types (AL, EL, and DLC-CL) and their $ZnCl_2$-activated biochar. After 6 cycles, DLC-CL-$ZnCl_2$-600 °C produced 526.32 mg g^{-1} for methylene blue and 2156.77 mg g^{-1} for Congo Red with a surface area of 1075 m^2 g^{-1} and 95% recyclability through pore filling, electrostatics, and π–π interactions.[96] These results show that heteroatom doping is a crucial strategy for improving adsorption in carbon-based materials for wastewater treatment. Therefore, by introducing chemically active surface sites, heteroatom engineering is a useful method to improve adsorption capacity and selectivity. Thus, it is possible to optimise the design of biochar formed from lignin for efficient and durable wastewater treatment.[95,96]

4.6. Composite and hybrid carbon materials

Biochar is combined with nanoparticles, polymers, or metal oxides to form composite and hybrid carbon materials that increase adsorption capacity, surface area, and selectivity for contaminants, including dyes and heavy metals. These hybrids,

such as chitosan-lignin composites or iron oxide-lignin biochar, achieve capacities exceeding 500 mg g^{-1}. This is achieved through improved pore structures, functional groups, and processes, including complexation and ion exchange.[97,98] Sun *et al.* (2021) reviewed biochar and lignin-based adsorbents (BBAs/LBAs), noting that hybrids like MgO-biochar achieve 66.70% phosphorus (P) removal and 11.70% NO_3^- *via* ion exchange/precipitation. However, lignin nanoparticles use chelation to absorb 90% of phosphate (5 mg L^{-1}). Carboxyl groups for Cr^{4+} absorption (130.50 mg g^{-1} in FeS-biochar composites) and dyes like MB (5306 mg g^{-1} from algal biochar) are increased by chemical modifications such H_2O_2-oxidized biochar.[97] Yang *et al.* (2025) investigated lignin modifications for heavy metals and antibiotics, emphasising the Fe_3O_4-lignin hydrogel (88 mg g^{-1} Cd^{2+}, 70% after 4 cycles) and the polyethyleneimine-lignin carbon (371.70 mg g^{-1} Sb^{3+}) *via* complexation/electrostatic interactions.[98] Though synergistic changes, such as Fe–Mg oxides and polymers, and composite/hybrid lignin-biochar materials significantly improve pollutant removal (371–575 mg g^{-1} for metals, 90% for antibiotics). The superior porosity, greater functional groups, and excellent recyclability (>70% after 4–10 cycles) make these hybrids viable substitutes for pure adsorbents in complex wastewater treatment.[97,98]

5. Characterisation techniques

The characterisation of biochar is necessary to identify materials suitable for use in tertiary potabilization treatments or wastewater treatment plants. The characterisation of activated carbons is obtained through two core alternative approaches, which are based on the determination of (adsorption performance and the physicochemical) parameters. The first approach determines the structure-dependent indices, which are estimated with respect to standardised compounds of the proper molecular dimensions, directly correlated to the adsorption capabilities of the activated carbon itself. The second approach enables the collection of information on the main structural properties, such as morphology, porosity distribution, and the nature of the chemical groups present on the surface.[99] Fig. 4(a) summarizes the comprehensive biochar characterization using multiple analytical techniques. It highlights the surface area (BET), morphology (SEM/TEM), functional groups (FTIR), crystallinity (XRD), thermal behaviour (TGA), carbon defects (Raman), and elemental composition (CHNS/O), providing an integrated understanding of biochar structure, composition, and physicochemical properties relevant to energy and environmental applications.

5.1. Elemental and structural analysis

5.1.1. Elemental analysis. Biochar is composed of carbon, hydrogen, and oxygen as primary elemental ingredients, with low amounts of nitrogen, sulphur, and other trace elements. Biochar resulted from aliphatic and aromatic compounds, which are carbon-rich and containing less oxygen undergo pyrolysis at high temperatures. During the pyrolysis of biomass, biochar's carbon content increased and its oxygen concentration dropped because of many chemical reactions.[102] The ultimate analysis is an effective approach for predicting biochar performance in a variety of applications. It includes information on biochar carbonization and probable stability. The carbon content is found to be maximum (40–80 wt%) in biochar.[103] Carbon directly reflects the degree of carbonization during pyrolysis. A high carbon content indicates enhanced aromaticity, structural condensation, and long-term stability, making the biochar more resistant to microbial degradation. The carbon-rich biochars are highly desirable for carbon sequestration, soil amendment, and climate mitigation. Moreover, the increased carbon content is associated with higher electrical conductivity and improved adsorption capacity for organic pollutants.[104–106] The presence of aliphatic carbon structures in biochar is represented by hydrogen. Higher levels of aromatic condensation and thermal maturity are often indicated by lower hydrogen content. The measure of biochar stability is the H/C atomic ratio; lower values indicate more graphitic and resistant carbon structures. As a result, biochar with low hydrogen content have longer residence durations and are more stable in soils.[107] Furthermore, nitrogen is essential for surface chemistry and nutrition availability. Nitrogen-doped biochars can improve soil fertility by slowing nitrogen release and retaining nutrients in soil applications.[108] Furthermore, in energy storage systems, nitrogen functionalities can improve electrochemical performance and catalytic activity.[109] The lower concentration of sulfur contributes to surface reactivity and redox behaviour. Sulfur-containing functional groups can increase biochar's affinity for heavy metals through complexation and precipitation mechanisms. In some cases, sulfur-doped biochars show improved catalytic and electrochemical characteristics. However, high sulfur can cause the creation of sulfur oxides during thermal processing, which is undesirable for some applications.[110] Oxygen content is another important element affect the biochar stability and properties. Oxygen is linked to surface functional groups including hydroxyl, carboxyl, carbonyl, and ether groups. These oxygenated functionalities have a considerable influence on biochar polarity, hydrophilicity, and cation exchange capacity. A high oxygen concentration improves wettability and the adsorption of polar molecules and metal ions. Also, it indicates lower thermal stability and a greater susceptibility to oxidation. The O/C ratio is commonly used to determine biochar reactivity and aging behaviour.[111] The H and O content of biochar decreases as the pyrolysis temperature rises. As a result, the H/C and O/C ratios drop, indicating increased biochar aromaticity and carbonization, as well as decreased surface polarity.[112] The O/C and H/C ratios of biochar are often used to assess its viability as a source of energy. A higher H/C ratio indicates increased energy density, indicating that biochar has greater potential as an effective energy carrier.[113] An increase in pyrolysis temperature typically increases carbon content by promoting the gradual volatilisation of thermally labile components. In contrast, at higher temperatures, the amounts of hydrogen and oxygen decrease due to the breaking of weaker bonds within the

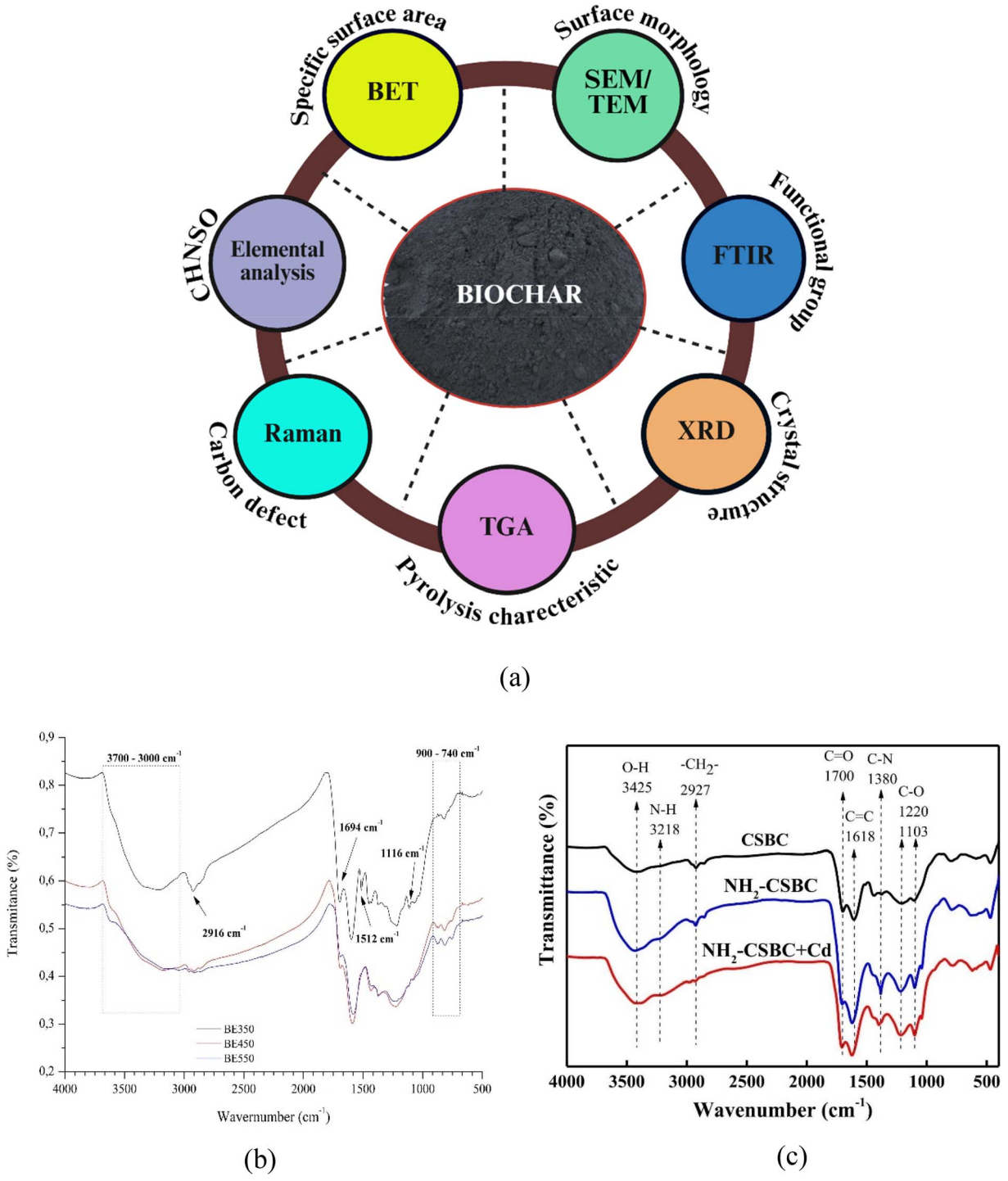

Fig. 4 (a) Various characterisation techniques of biochar for adsorption. (b) FTIR analysis of biochars from bamboo culm. Reproduced from Sbizzaro *et al.* (2021) with permission from Elsevier,[100] copyright 2021 (c) FTIR spectrum of CSBC, NH_2-CSBC before adsorption, and NH_2-CSBC after Cd(II) adsorption. Reproduced from Ma *et al.* (2023) with permission from Elsevier,[101] copyright 2023.

biochar structure.[114] The elemental analysis of different feedstock biochar for absorption is represented in Table 3.

5.1.2. FTIR analysis. FTIR analysis provides information about the functional groups in different adsorbents, which might facilitate the sorption process of heavy metal pollution. The chemical functional groups on the biochar surface were identified using attenuated total reflectance Fourier transform infrared (ATR-FTIR) spectroscopy, with 200 scans at a resolution of 4 cm^{-1}. Potassium bromide (KBr) was used as a material for the infrared beam splitter with coverage of the normal 4000–400 cm^{-1} mid-IR spectral region.[118] Vuong *et al.* (2025) confirmed the mechanisms for Pb and Zn immobilization by identifying the surface functional groups of biochar made from taro stems and the apatite amendment derived at 300 °C and

500 °C. The dehydration, decarboxylation, and increased aromaticity of the biochar matrix were shown by the FTIR spectra, which also showed a progressive reduction in oxygen-containing functional groups (–OH, C–H, and C–O) as the pyrolysis temperature increased. The different adsorption tendencies of taro stem biochar (TSB300) and (TSB500) toward heavy metals was explained by these structural changes. The presence of distinctive phosphate (PO_4^{3-}), hydroxyl (OH^-), carbonate (CO_3^{2-}), and fluoride (F^-) groups in apatite demonstrated its capacity to immobilize Pb and Zn *via* ion-exchange and precipitation processes.[126] Sbizzaro *et al.* (2021) reported that increasing the production temperature of bamboo biochar reduced aliphatic and oxygenated groups (–OH, C–O) and enhanced aromatic structures (900–740 cm^{-1}) as shown in Fig. 4(b). FTIR study indicates that as the production temperature of biochar increases, aliphatic and oxygen-containing functional groups (–OH and C–O) decrease, whereas aromatic bands (900–740 cm^{-1}) appear, indicating enhanced aromaticity. This pattern shows the progressive carbonization and reduced surface polarity at elevated temperatures, consistent with the decreasing O, H, O/C, and H/C ratios. FTIR clarifies the impact of production temperature on biochar's aromaticity, surface functionality, and its adsorption behaviour towards organic molecules, thereby revealing the connection between heat treatment and changes in surface chemistry.[100] Ma *et al.* (2023) reported that FTIR spectra of corn-stalk biochar before and after Cd(II) adsorption (Fig. 4(c)), identified noticeable shifts and intensity changes in the amino-related bands. These spectral changes confirm that the NH_2 functional groups on NH_2-CSBC actively participated in Cd^{2+} binding through strong complexation.[101]

5.1.3. XRD analysis. X-ray diffraction (XRD) is a commonly used technique for analysing the structure and crystallinity of biochar.[127] Chang *et al.* (2023) modified rice husk biochar and studied the adsorption of ammonium and nitrate from wastewater. The XRD patterns in Fig. 5(a) show that biochar produced at temperatures ranging from 300 to 700 °C exhibits broad, diffuse peaks, indicating an amorphous structure dominated by SiO_2 and disordered carbon. At 900 °C, sharp, well-defined diffraction peaks appear, indicating the development of crystalline phases. This demonstrates that higher pyrolysis temperatures promote the transition from amorphous to more crystalline structures in rice husk biochar.[128] Chaudhary *et al.* (2024) performed pyrolysis on several biomass samples, including sugarcane bagasse (SB), Brinjal Stem (BS), and Citrus Peel (CP). The XRD patterns of SB, BS, and CP biochar exhibited an amorphous carbon structure as shown in Fig. 5(b) characterised by wide C (002) reflections at $2\theta = 10.5$–$17.8°$ and faint C (100) peaks at around 44.3–44.6° for all pristine samples (a). After Pb adsorption (b), prominent peaks for Pb_2CO_2 show up at $2\theta = 34.1$–$36.3°$ and Pb $(NO_2)_2$ at 53.7° in BS, showing that Pb accumulates through surface precipitation. Cu-loaded biochar (c) shows Cu_2O reflections at 57.7–61.3°, whereas Cr adsorption (d) produces Cr_2O_3 (24.1° and 65.7°) and Cr_2N (41.4–44.3°) phases, suggesting reduction and complex formation. Cd-adsorbed samples (e) exhibited Cd $(OH)_2$ peaks at 29.3° and 60.9°, and $CdO/CdCl_2$ reflections at 35.9–56.6°. Persistent $CaCO_3$ peaks at 29.7°, with SiO_2 (26.5°) and KCl (23.1°, mostly in CP), highlighting the mineral phases to heavy-metal adsorption.[129]

5.1.4. Raman analysis. Raman spectroscopy serves as a powerful tool for evaluating structural defects and the extent of graphitisation in carbon-based materials. In the context of biochar design and improvement, two characteristic peaks are particularly important. The first is the D band, which indicates structural disorder, and the second is the G band, which reflects ordered graphitic domains. Together, these bands provide valuable insight into the structural quality and carbon ordering within biochar.[132] Raman spectroscopy is useful for analysing biochar due to its ability to detect sp^2-hybridized carbon structures. Biochar is made by pyrolyzing biomass and contains different degrees of aromatic carbon clusters, the size, ordering, and condensation of which are directly influenced by the pyrolysis temperature and feedstock type. Raman spectroscopy identifies two fundamental bands: the D-band (1350 cm^{-1}), caused by disordered carbon structures and defects in the graphitic lattice, and the G-band (1580 cm^{-1}), caused by the in-plane vibration of sp^2-bonded carbon atoms in perfect graphitic

Table 3 Elemental analysis of different biochars for adsorption

Biochar	C (wt%)	H (wt%)	N (wt%)	S (wt%)	O (wt%)	H/C	O/C	References
Corncob biochar	77.25	3.027	0.58	0.169	18.75	0.039	0.243	115
Walnut shell (WS-600)	68.65	2.14	1.49	0.08	25.70	0.37	0.28	116
Palm Kernel shell (750)	78.95	1.79	1.00	—	18.27	0.02	0.23	117
Wood chip (WB)	83.76	2.76	1.37	0.11	6.59	0.40	0.06	118
Tea waste (700)	77.89	1.76	4.05	—	6.50	0.02	0.08	119
Sunflower seed shells	72.3	5.5	0.8	—	21.2	0.9	0.2	120
Peanut shells	83.7	2.9	1.2	—	12	0.42	0.11	120
Coconut shell	90.6	1.3	0.8	0.1	4.2	0.17	0.03	121
Spent mushroom substrate	59.94	2.91	1.75	—	2.13	0.048	0.036	122
Cassava peel	40.95	5.67	0.22	0.09	52.17	1.66	0.95	123
Rice husk	40.15	5.98	0.41	0.78	52.68	1.79	0.98	123
Red pepper stalk	49.78	6.46	1.09	—	42.67	1.56	0.64	124
Coffee silverskin	60.78	2.591	2.897	0.148	11.78	0.508	0.146	125
Olive mill waste	61.3	4.33	1.4	—	32.9	0.837	0.41	125
Grape pomace	65.68	4.92	2.06	—	16.24	0.89	0.186	125

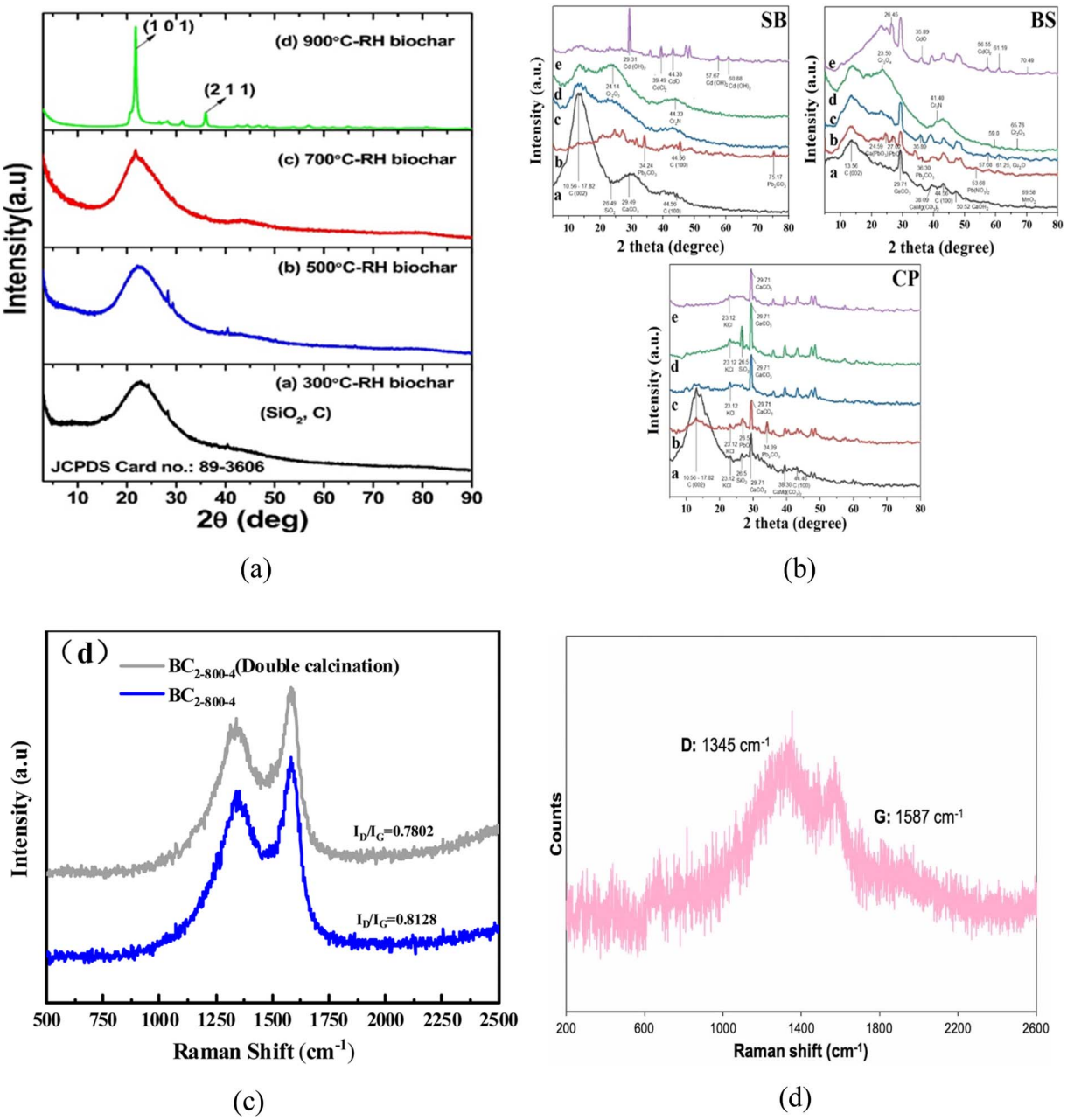

Fig. 5 (a) XRD patterns of pyrolysed RH biochar samples. Reproduced from Chang *et al.* (2023) with permission from Elsevier,[128] copyright 2023 (b) XRD spectra of biochar derived from sugarcane bagasse (SB), Brinjal Stem (BS), and Citrus Peel (CP), where (a) before adsorption, (b) after Pb adsorption, (c) after Cu adsorption, (d) after Cr adsorption, and (e) after Cd adsorption. Reproduced from Chaudhary *et al.* (2024) with permission from Springer Nature,[129] copyright 2024. (c). Raman analysis of Corn biochar (BC) adapted from Huang *et al.* (2023)[130] and (d) Raman spectra of Cedrela odorata biochar. Reproduced from Subratti *et al.* (2021) with permission from Elsevier,[131] copyright 2021.

domains. The intensity ratio ID/IG is a quantitative tool for determining the degree of structural order *vs.* disorder in biochar materials.[133] Huang *et al.* (2023) activated corn starch-based biochar with $ZnCl_2$ at 800 °C to obtain a porous, graphitic biochar for tetracycline adsorption. Raman analysis revealed that increasing the activation temperature and time lowered the ID/IG ratio, indicating higher graphitisation of the biochar (Fig. 5(c)). Biochar with lower ID/IG values showed slightly better tetracycline adsorption when surface areas were similar, due to stronger π–π interactions. Overall, both defects and graphitisation contributed to adsorption, depending on the textural properties of the biochar.[130] The Raman spectra of Cedrela odorata biochar exhibited distinct G and D bands as shown in Fig. 5(d), with their intensity ratio (IG/ID) indicating an equilibrium between graphitic and defective carbon structures. The reported IG/ID ratio of 0.57 suggests that the material is predominantly amorphous, with a minor graphitic structure. Compared to rice straw biochar, which had higher IG/ID values (up to 0.87), Cedrela odorata biochar showed significantly lower crystallinity.[131]

5.2. Surface and porosity characterisation

5.2.1. SEM analysis. Scanning Electron |Microscope (SEM) is a crucial tool for examining the morphology of adsorbent surfaces. It provides a clear image of biochar's micro- and mesoporous structure by allowing measurements of pore distribution and surface arrangement. It is also useful for comparing surface morphology before and after adsorption, thereby revealing structural changes caused by pollutant adsorption.[134] The distribution, size, and form of pores on biochar surfaces are observed through SEM. SEM images of soap nut seed biochar, for instance, revealed irregular pores on a rough surface, making it easier for ciprofloxacin molecules to adsorb.[135] Likewise, SEM analysis of biochar produced from sugarcane bagasse revealed enhanced porosity and homogeneity at elevated activation temperatures, corresponding with greater adsorption capabilities for Fe^{2+} ions.[136] Micropores and mesopores, which are crucial for ion adsorption, can be distinguished using SEM. For example, chromium adsorption decreased the pore size and number in raw biochar, indicating efficient ion capture. The pores were roughly 10 μm in size.[137] Energy-dispersive X-ray Spectroscopy (EDX/EDS) is commonly used in conjunction with SEM to analyse the elemental composition of biochar surfaces. This combination enables mapping and identification of elements, including adsorbed metals, carbon, oxygen, nitrogen, and sulfur.[138] Fseha *et al.* (2023) observed clear morphological changes in date palm frond biochar before and after phenol adsorption.[139] Before adsorption (Fig. 6(a)), the biochar displays a well-defined honeycomb-like structure with numerous open, interconnected pores. After adsorption (Fig. 6(b)), many pores appear partially filled, and the surface becomes smoother and more compact, indicating that phenol has occupied the pore spaces and surface sites. It was noted that the observed changes confirm successful phenol adsorption onto the biochar.[139] The combination of SEM with EDX provides accurate characterisation of the biochar surface's elemental composition. However, SEM-EDX's capacity to identify and characterise organic pollutants remains restricted.[134]

5.2.2. BET analysis. BET (Brunauer–Emmett–Teller) analysis is an important tool for determining the surface area and pore size of biochar suitable for adsorption. BET characteristics such as specific surface area, pore volume, and average pore size have a substantial impact on adsorption behaviour and diffusion processes.[143] BET analysis of various biochar samples for the adsorption process is presented in Table 4. Porosity has been recognised as a crucial characteristic of biochar that influences its adsorption behaviour towards aromatic chemicals. Lin and Zhao (2016) reported a significant linear association ($r = 0.897$) between toluene adsorption capacity and the specific surface area (SSA) of biochar, demonstrating that materials with larger surface areas provide more accessible adsorption sites for aromatics.[144] Thus, increasing SSA is an efficient way to enhance biochar's adsorption of aromatic chemicals. Studies has indicated that materials like activated carbon, porous carbon spheres, and hierarchically porous carbon have higher adsorption capacities when their specific surface area increases. For instance, porous carbon spheres with rich microporous-mesoporous structures offered greater opportunities for the adsorption of volatile organic compounds (VOCs),[145] while activated carbon with a bigger surface area showed a higher adsorption capacity for toluene.[146] Thus, increasing SSA is an efficient way to enhance the adsorption of aromatic chemicals by biochar. Highly microporous materials are typically produced through physical activation, which also significantly increases their specific surface area. Activating pine nut shells in CO_2 environment raised their specific surface area from 146 $m^2\ g^{-1}$ (non-activated) to 1503 $m^2\ g^{-1}$ after 80 min, primarily due to a formation of micropores.[147] Thermally unstable biomass components, such as starch, hemicellulose, and lignin, break down into volatile chemicals like acetic acid, tar, methanol, CO_2, and H_2 at high temperatures. By releasing these volatiles, new active adsorption sites are formed as previously blocked pores open and new porous routes are generated. Besides physical activation, chemical activation techniques are also extensively used to enhance the porosity of biochar. During co-pyrolysis with dehydrating or corrosive activating chemicals, the carbon matrix experiences cross-linking, condensation, and etching processes, resulting in a microporous structure.[148] Chen *et al.* (2025) utilised N_2 adsorption–desorption isotherms and identified a Type IV isotherm for their modified biochar, indicating the presence of micro- and mesoporous characteristics. A hierarchical pore network was directly connected to increased adsorption efficiency for certain pollutants.[149] Wang *et al.* (2015) prepared mesoporous carbon materials for the adsorption of benzene and cyclohexane and reported that the diffusion coefficient of the carbon with 5.0 nm pores was double that of the sample with 1.8 nm pores. These results indicate that pores only slightly larger than the adsorbate molecules contribute effectively to adsorption, while excessively large pores primarily facilitate the diffusion of aromatic compounds rather than their retention.[150]

5.3. Thermal behaviour

The thermal stability and structural characteristics of biochar are often studied using thermogravimetric analysis (TGA). It provides useful information on moisture content, pyrolysis yield, and the breakdown of major biomass components like hemicellulose, cellulose, and lignin. DSC provides insights into the thermal dynamics during adsorption or desorption, facilitating the calculation of the heat of adsorption and the differentiation between physisorption and chemisorption mechanisms.[156] TGA was performed using a Mettler TGA/DSC machine at a heating rate of 10 °C min^{-1} under an air environment from 25 to 700 °C to evaluate the thermal stability of the biochar. The TGA was used to study CO_2 adsorption kinetics at a gas flow rate of 50 mL min^{-1}. Results showed that nitrogen-containing surface groups on carbon materials increase CO_2 absorption. In this context, elemental analysis measures C, H, N, and S, whereas oxygen content is estimated using the difference, assuming that only these five elements are liberated from carbon samples. Rambhatla *et al.* (2025) analysed the TGA results, which showed that the decomposition of mixed wood

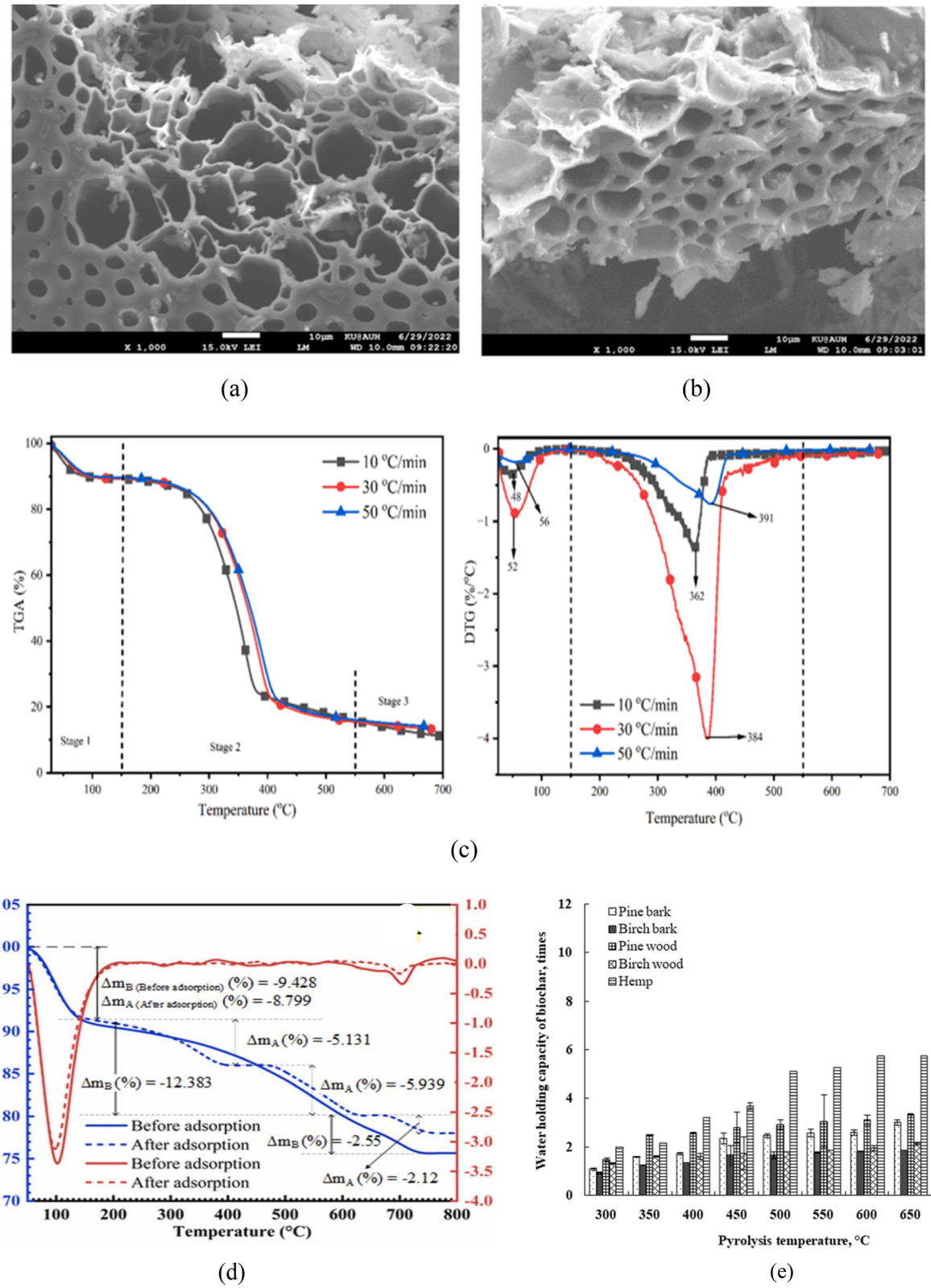

Fig. 6 SEM analysis of date palm frond biochar (600 °C) (a) before phenol adsorption and (b) after phenol adsorption (adapted from Fseha *et al.* (2023)).[139] (c). TGA analysis of mixed wood sawdust. Reproduced from Rambhatla *et al.* (2025) with permission from Elsevier,[140] copyright 2025, (d) TGA analysis of jackfruit peel biochar before and after adsorption. Reproduced from Ton-That *et al.* (2024) with permission from Elsevier,[141] copyright 2024. (e). Graphical representation of the water holding capacity of different biochars. Reproduced from Useviciūtė *et al.* (2020) with permission from Springer Nature,[142] copyright 2020.

Table 4 BET analysis of different biochar for adsorption application

Biochar	BET surface area ($m^2\ g^{-1}$)	Pore volume ($cm^3\ g^{-1}$)	Application	References
Eucalyptus waste (700 °C)	2592	1.150	Adsorption desulfurization (ADS) with high dibenzothiophene (DBT) adsorption capacity (172.5 mg g^{-1})	151
Groundnut shell	1089	0.630	Malachite green dye adsorption	152
Cow manure, (BC-CM)	263	0.164	Methylene blue dye removal	121
Rice husk (BC-RH), and coconut shell (BC-CS)	220 197	0.127 0.099		
Bagasse	8.217	6.310	Cationic dyes removal	153
Brinjal stem	360.910	0.649	Adsorption of heavy metals	143
Sludge and liriodendron leaves (SLAC)	45.206	0.142	Methyl orange removal	154
Marigold floral waste	93.550	0.092	Methylene blue removal	155

sawdust (Fig. 6(c)) takes place in three main steps from 30 to 700 °C. Initial weight loss below 150 °C is due to moisture and light volatiles. The largest mass reduction occurs between 150 and 550 °C as hemicellulose, cellulose, and part of the lignin break down. Above 550 °C, the remaining lignin slowly degrades, producing a stable char residue. DTG peaks align with these transitions. Higher heating rates shift decomposition to higher temperatures due to thermal lag, resulting in slightly greater volatile release and reduced char. Overall, the TGA profile highlights the material's thermal stability and the temperature-dependent behaviour of its biomass components.[140] Ton-That *et al.*(2024) pyrolysed the jackfruit peel and analysed the thermal behaviour undergoes three primary degradation phases. Initial mass loss was observed below 200 °C attributed to moisture evaporation (Fig. 6(d)). Significant weight reduction between 200-580 °C linked to the combustion of the graphitic carbon fraction, and a minor loss at 580–800 °C associated with the onset of ashing, featuring an endothermic peak near 700 °C. In addition to Pb(II) adsorption, further mass losses were detected within the temperature ranges of 250–450 °C and 450–650 °C, due to the breakdown of Pb(II) biochar complexes containing –OH and C=C functional groups.[141]

5.4. Hydrophobicity and wettability

The adsorption of aromatic hydrocarbons by biochar is generally governed by biochar surface characteristics, the molecular structures of the organic contaminants, and surrounding environmental conditions. The polarity index ((O + N)/C or O/C) is extensively used to evaluate a material's absorbability.[157] In several instances, hydrophobic interactions are identified as the primary mechanism driving the adsorption of aromatic chemicals onto biochar. However, adsorption mostly occurs at the adsorbent surface *via* specific functional groups. Also, bulk elemental polarity indices can be deceptive in determining whether biochar is hydrophobic or hydrophilic. Thus, assessing surface polarity, which is frequently determined by XPS analysis, provides a more suitable and accurate measure of adsorption behaviour.[158] The hydrophobic domain responsible for hydrophobicity is caused by the presence of aromatic structures, primarily aromatic rings, which lower chemical functionalization.[159] Wettability of a solid surface is the ability of a liquid to spread or adhere to it. It plays a crucial role in adsorption processes, as adsorption is essentially an interfacial phenomenon. Wettability is commonly quantified by measuring the contact angle between a liquid droplet and a solid surface (the sessile-drop method), with a lower contact angle indicating stronger wetting (higher affinity) and greater potential for liquid adsorption.[160] In adsorption-based studies, it has been demonstrated that modifying surface chemistry, through surfactant deposition or nanoparticle coatings, can alter a material's wettability and, consequently, its adsorption performance.[161] Usevičiūtė *et al.* (2020) showed that the water-holding capacity of different biochars increased with increasing pyrolysis temperature. Five feedstocks, pine bark, birch bark, pine wood, birch wood, and hemp, were taken for the test. Fig. 6(e) showed that water-holding capacity increases with increasing pyrolysis temperature, indicating that higher temperatures enhance the porosity and structure of the resulting biochar. Among the materials, hemp consistently showed the highest water-holding capacity, reaching its peak at 700 °C. In contrast, pine bark and birch bark display lower capacities across all temperatures, while pine and birch wood fall in the mid-range. This indicated that both feedstock type and pyrolysis temperature strongly affect biochar's water-holding capacity, primarily due to differences in lignocellulosic composition and thermal transformation.[142]

6. Lignin-based adsorbents for water treatment

6.1. Overview of adsorption principles

Adsorption is a fundamental surface phenomenon widely used in wastewater treatment. It is the process by which molecules or ions are held onto an adsorbent surface through chemical or

physical interactions. Physicochemical characteristics, including surface area, porosity, functional group density, and surface charge, affect the effectiveness of lignin-based adsorbents. Through ion exchange, coordination with metal ions, electrostatic attraction, and H-bonding among other activities. A naturally occurring aromatic polymer with several hydroxyl, methoxy, and carboxyl groups, lignin offers many binding sites for pollutants.[162] However, due to its limited surface area and heterogeneous structure, naturally occurring lignin frequently shows inadequate adsorption efficacy which promotes research into structural and chemical modifications. Yang *et al.* (2025) provided a methodical summary of the physicochemical processes governing adsorption by lignin-derived adsorbents. They found that the removal effectiveness of Cr^{6+} from amine-functionalized lignin biochar was up to 13.5 times more than that of unmodified lignin biochar. In comparison, polyethyleneimine-modified lignin porous carbon exhibited a remarkable adsorption capacity of 371.70 mg g^{-1} for Sb^{3+}. While imine-grafted lignin demonstrated 115.60 mg g^{-1} for Pb^{2+}, exceeding pristine kraft lignin by a factor of 3.2. The findings highlight that significant increases in adsorption affinity and reusability can be attained by changing surface charge and adding heteroatoms. These improved systems adsorption efficiencies after 5–8 cycles often remained between 85 and 90%, indicating good material strength.[98] Tkachenko *et al.* (2024) provided a mechanistic quantification for dye adsorption using methylene blue (MB^+) as a probe molecule. Their study revealed that 61% of adsorption was due to H bonding (mainly through aliphatic and phenolic –OH groups), 38% to electrostatic interactions, and less than 1% to π–π stacking. The maximum adsorption capacity (Q_m) for MB^+ on kraft lignin was 118 mg g^{-1}, increasing to 162 mg g^{-1} upon carbonyl group reduction. The adsorption followed the Langmuir isotherm ($R^2 > 0.98$) and pseudo-second-order kinetics ($k_2 = 0.0098$ g mg^{-1} min^{-1}), validating chemisorptive control. The FTIR and XPS analyses confirmed that –OH and –COOH functionalities were the primary active sites responsible for binding.[163] Hydrogen bonding, ion exchange, coordination and electrostatic forces are all involved in adsorption on lignin-based materials. These processes are influenced by solution chemistry and surface functioning. Amino, sulfonic, and metal oxide groups are added, the active-site density and adsorption capacity increase from several to several hundred mg g^{-1}. Thus, it is essential to comprehend the quantitative contributions of each interaction pathway to build next-generation lignin adsorbents with predictable and adjustable adsorption behaviour.[71,98]

6.2. Heavy metal adsorption

Heavy metal (HMs) ions, including Pb^{2+}, Cd^{2+}, Cr^{2+}, Cu^{2+} and Ni^{2+}, are among the most hazardous and persistent contaminants. They tend to bioaccumulate and cannot be broken down organically, posing significant dangers to the environment and public health.[164] Various biomass sources for adsorbing heavy metal ions in lignin-based adsorbents are listed in Table 5. Zhang *et al.* (2023) found that lignin-based biosorbents with carboxyl and phenolic hydroxyl groups were effective at absorbing specific metal ions. A lignin composite adsorbent demonstrated significant reusability at pH 5 at 293 K, with maximal adsorption capacities of 70.41 mg g^{-1} (Ni^{2+}), 75.70 mg g^{-1} (Cu^{2+}), 82.41 mg g^{-1} (Zn^{2+}), and 91.74 mg g^{-1} (Pb^{2+}) with more than 86% desorption efficiency using 0.5 M HNO_3. The Langmuir model states that a lignin-based resin (LBR) made by polycondensation from calcium lignosulfonate has adsorption capacities of 194.6 mg g^{-1} (Pb^{2+}) and 59.9 mg g^{-1} (Cu^{2+}), with pseudo-second-order kinetics suggesting that chemisorption predominated. Fig. 7(a) shows a schematic of heavy metal ion removal from wastewater using chemically modified lignin biosorbents. The raw lignin (AL-KL-LS) from contaminated water containing Pb^{2+}, Cu^{2+}, and Cr^{6+} undergoes functionalization *via* amination (-NH_2), carboxylation (-COOH), sulfonation (-SO_3H), thiolation, and PEI/PANI grafting. Adsorption proceeds through H-bonding, electrostatic interactions, and surface complexation, yielding metal-coordinated structures and purified effluent.[165] Yang *et al.* (2025) found that adsorption performance is significantly improved by functionalized lignin. The amine-modified lignin porous carbon for Sb^{3+} yielded 371.7 mg g^{-1}, while for Pb^{2+}, the imine-modified lignin demonstrated 115.6 mg g^{-1}, which is approximately three times greater than that of raw lignin. Fe_3O_4-modified lignin hydrogels could be magnetically recovered with more than 60% efficiency and exhibited 88 mg g^{-1} Cd^{2+} adsorption capacity. Increased surface charge, nitrogen coordination and redox-active iron sites were identified as the causes of the improvements.[98] According to the type of modification and target metal, lignin-based adsorbents exhibit adsorption capabilities ranging from 70 to 550 mg g^{-1}, which are primarily controlled by complexation, ion exchange and electrostatic interactions. They are potential green materials for heavy metal cleanup due to their low cost, high regeneration efficiency and modular chemistry.[98,164,165]

6.3. Organic dye adsorption

Methylene blue (MB), Congo red (CR), and azo dyes (AD) are examples of synthetic dyes that contribute significantly to industrial wastewater pollution, particularly from the textile, paper, and printing industries. These dyes are poisonous, stable and impervious to biological deterioration. Through processes such as ion exchange, hydrogen bonding, π–π stacking, and electrostatic interactions, the lignin aromatic backbone and oxygen-rich functional groups (–OH, –COOH, –OCH_3) provide strong binding sites for dye molecules. However, unmodified lignin frequently shows poor dye removal effectiveness. The following resulted in the development of modified or composite lignin-based adsorbents with enhanced adsorption capacity and selectivity.[169,178,179] Meng *et al.* (2020) produced aminated CELF (cosolvent enhanced lignocellulosic fractionation) lignin for dye removal. They obtained >90% removal efficiency and high adsorption capacities of 502.7 mg g^{-1} for Direct Blue 1, fitting pseudo-second-order kinetics and the Langmuir isotherm. After 4 cycles, the adsorbent retained 65% efficiency due to the amine groups' high electrostatic attraction toward

Table 5 Lignin-based adsorbents for heavy metal ions from various biomass sources[a]

Source of biomass	Metal ion	C_i (mg L^{-1})	C_e (mg L^{-1})	Removal efficiency (%)	q_e (mg g^{-1})	Temperature (°C)	pH	Adsorbent dose (g)	References
Corn stover	Cd^{2+}	100	4.21	95.79	19.16	25	5.5	0.2 (in 20 mL)	166
Sarkanda grass	Cd^{2+}	112.4	<1.12	>99	13.42	20	6.2	5.0	167
Pine nut shells	Cr^{4+}	Varied	—	—	360 (q_{max} Langmuir)	25	2.0	2.0	168
Agricultural waste (lignin nanoparticles)	Cd^{2+}	50	—	—	127.9	25	5.0	1.0	169
Rice husk	Pb^{2+}	Varied	—	>95	—	RT	Varied (2–10)	1.0	170
Lignocellulosic biomass	Cu^{2+}	Varied	—	>95	60.86	25	6.0	2.0	171
Industrial softwood	Pb^{2+}	100	—	90	49.8	25	7.0	1.0	172
Norway spruce wood	Pb^{2+}	Varied	—	99	10.3 (q_{max})	45	5.0	2.0	173
Norway spruce wood	Cd^{2+}	Varied	—	Above 95	6.3 (q_{max})	45	6.0	2.0	173
Norway spruce wood	Cu^{2+}	Varied	—	95	7.9 (q_{max})	45	5.5	2.0	173
Norway spruce wood	Zn	Varied	—	Above 90	6.0 (q_{max})	45	6.0	2.0	173
Walnut shell	Pb^{2+}	5	<0.05	99	47.4 (q_{max})	RT	5.0	—	174
Barley straw	Cd^{2+}	100	5	95	95	25	6.0	2.0	175

[a] C_i = initial concentration, C_e = equilibrium concentration, q_e = equilibrium adsorption capacity.

anionic dyes and increased surface reactivity.[179] Wang *et al.* (2018) synthesised carbon composite lignin adsorbents (CCLA) by hydrothermally treating glucose and calcium lignosulfonate. Having a maximal adsorption capacity of 120–140 mg g^{-1}, the composite eliminated 99% of Congo red and Eriochrome black T at 40 mg L^{-1}. They are driven by π–π interactions and H-bonding between the dye molecules and lignin aromatic rings; adsorption followed chemisorption-controlled pseudo-second-order kinetics.[178] Pourbaba *et al.* (2024) showed that hydro-tropically generated lignin nanoparticles (LNPs) have a methylene blue adsorption capacity of 127.9 mg g^{-1}. This is roughly 6 times that of pristine lignin (20.7 mg g^{-1}), with equilibrium attained in 3 minutes. According to the Langmuir model, the homogeneous active sites and increased surface area (14.90 m^2 g^{-1}) improved dye uptake through chemisorption and monolayer adsorption.[169] Therefore, with adsorption capabilities ranging from 100 to 500 mg g^{-1}, depending on modification and dye type, lignin-based adsorbents exhibit great potential for dye removal. In wastewater dye treatment, modified lignin systems show fast kinetics, high regeneration efficiency and sustainability. The main mechanisms are π–π stacking, hydrogen bonding and electrostatic interactions.[169,179]

6.4. Pharmaceutical micropollutant adsorption

Antibiotics, analgesics and hormones are examples of pharmaceutically active micropollutants (PhAMPs) which are persistent contaminants. They are increasingly found in wastewater and surface water due to their widespread use and inadequate removal in traditional treatment systems.[180] They lead to endocrine disruption, antibiotic resistance and ecotoxic consequences even at trace levels (ng-μg L^{-1}). Adsorption-based approaches using bio-based and carbonaceous materials have attracted interest for PhAMP remediation, in contrast to complex oxidation or membrane processes. This is due to their high affordability, reusability, and efficiency.[180,181] Gupta *et al.* (2024) addressed the origin and risk of PhAMPs, underlining that most medicines cannot be efficiently removed by traditional biological and chemical treatments. Even after secondary treatment, wastewater still contains antibiotics and analgesics, such as diclofenac and carbamazepine, with concentrations usually between 5 and 150 μg L^{-1}. Adsorption, which uses biochar, clays and lignin-derived adsorbents to achieve >90% removal efficiencies. The study identified electrostatic attraction, H-bonding, and π–π interactions between drug molecules and active sites on the adsorbent surface as the most practical and environmentally friendly method.[180] Mahdavi *et al.* (2025) identified adsorption as the most versatile method for treating quaternary wastewater after conducting a quantitative evaluation of several adsorbents for pharmaceutical removal. The maximal adsorption capacities (Q_m), ranging from 150 to 650 mg g^{-1}, depending on the adsorbent type and surface chemistry, activated carbons and polymer composites demonstrated a strong affinity for diclofenac, ibuprofen, and carbamazepine. They suggested that adsorption utilising functionalized bio-based adsorbents might meet the EU's 80% removal target for emerging micropollutants in wastewater treatment plant (WWTP) effluents. Also showed that adsorption efficiency depended on both capacity and affinity, in addition to surface area.[182] Munuhe *et al.* (2025) discussed the use of nanostructured adsorbents for the effective removal of pharmaceutical contamination. They found that magnetic starch composites had a diclofenac capacity (620.5 mg g^{-1}), whereas boron-doped graphene eliminated amitriptyline (up to 737.4 mg g^{-1}). Chemisorption was confirmed by adsorption kinetics that matched pseudo-second-order kinetics. The study highlighted that magnetic biochar and carbon-based nanoparticles provide simple separation and regeneration. Thus, lowering operating costs and suggesting the combination of

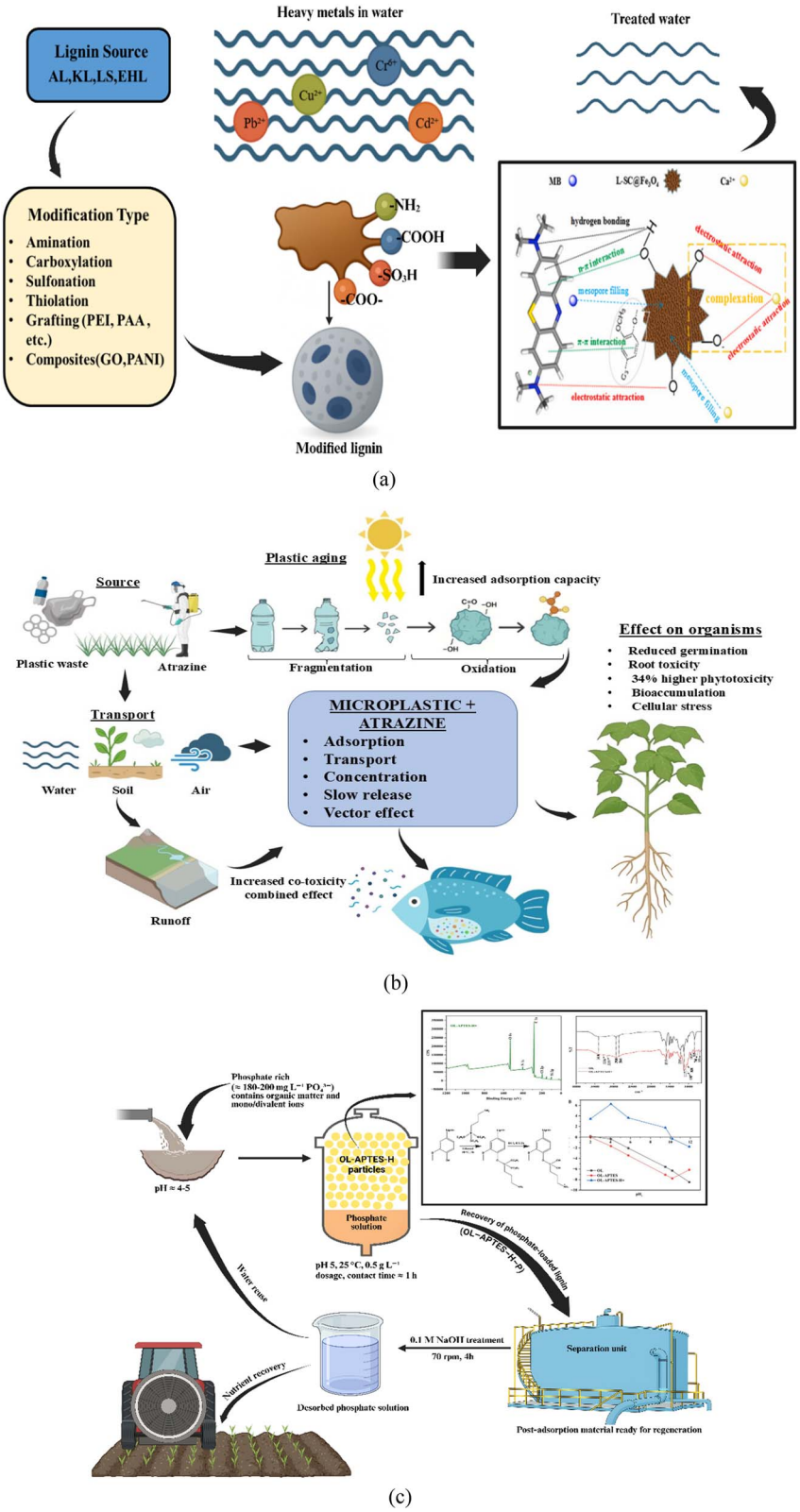

Fig. 7 (a) Schematic representation of heavy metal adsorption by modified lignin-based adsorbents (redrawn from Zhang *et al.* (2023)[165]), (b) UV-aged microplastics act as vectors for atrazine, enhancing environmental mobility and combined toxicity,[176] (c) schematic of phosphate recovery and nutrient recycling using functionalized organosolv lignin (OL-APTES-H) from wastewater (redrawn from Masliha *et al.* (2025)[177]).

adsorption with catalytic or biological post-treatments for sustainable pollutant elimination.[181] Despite typical adsorption capacities for common pharmaceuticals ranging from 100 to 700 mg g^{-1}, adsorption remains one of the most effective and sustainable methods for removing pharmaceutical micropollutants. The hybrid biochar and lignin-derived materials offer environmentally benign, regenerative alternatives for next-generation wastewater treatment. Mechanisms such as π–π stacking, Hydrogen Bonding, and electrostatic attraction predominate.[180–183]

6.5. Other emerging pollutants (microplastics, pesticides)

Emerging pollutants, such as microplastics (MPs) and pesticides, are gaining attention due to their persistence, potential for bioaccumulation, and synergistic toxicity with other contaminants. The pesticides contribute to long-term ecological damage through leaching and runoff. Microplastics act as both pollutants and carriers of both organic and inorganic contaminants.[184] Adsorption-based techniques have been increasingly used for removal because of their affordability, suitability for complicated matrices, and ease of usage. There have been promising results from the development of hybrid adsorbents from metal oxides, lignin, and charcoal for the simultaneous removal of these pollutants.[176,184,185] Verma *et al.* (2024) offered a thorough explanation of adsorption-based microplastic cleanup. According to their findings, depending on particle size and adsorbent type, MPs can be removed from water with removal efficiencies ranging from 80 to 99% using carbon-based and bio-derived adsorbents such as biochar, activated carbon and layered double hydroxides (LDHs). The mechanisms involved pore filling, hydrophobic interaction, and electrostatic attraction, all of which were enhanced by surface roughness and oxidation. The easy separation and regeneration were also enabled by hybrid magnetic adsorbents (Fe_3O_4-biochar), underscoring adsorption as a scalable, energy-efficient method for MP mitigation.[184] Biswas *et al.* (2024) found that aged microplastics with oxygenated functional groups absorbed up to 6.4 μg g^{-1} of organochlorine and neonicotinoid pesticides. Hydrophobic interactions, π–π stacking, and hydrogen bonding between pesticide molecules and microplastic surfaces were the primary factors controlling adsorption. The study highlighted that the adsorbed pesticide-microplastic compounds can prolong pesticide persistence in aquatic systems, acting as secondary pollution sources.[185] Souza *et al.* (2025) experimentally investigated the adsorption of the herbicide atrazine on aged polyethylene microplastics. The adsorption capacity increased from 0.504 mg g^{-1} to 0.742 mg g^{-1}, attributed to UV-induced oxidation and carbonyl group formation. Moreover, combined exposure of atrazine and microplastics increased phytotoxicity in Lactuca sativa by 34%, revealing the compound effect of co-contaminants. The study demonstrated that ageing processes enhance adsorptive behaviour and toxicity of MPs, underscoring the need for integrated treatment strategies. Fig. 7(b) shows that the UV-aged microplastics act as vectors for atrazine, enhancing environmental mobility and combined toxicity.[176] According to surface characteristics and aging effects, adsorption is a sustainable and effective way to remove microplastics and pesticides, reaching 80–99% MP removal and 0.5–7 μg g^{-1} pesticide uptake.[184] The process is mainly driven by hydrogen bonds, π–π interactions, and hydrophobic attraction which are further strengthened by surface oxidation and hybridization.[184]

6.6. Modified lignin adsorbents *vs.* raw lignin

Raw lignin has a low adsorption effectiveness due to its uneven structure, small surface area and lack of reactive functional groups. Many chemical modifications, including carboxylation, amination, and sulphur/nitrogen doping, have been developed to enhance adsorption selectivity, capacity, and reusability while introducing new active sites. Through improved chelation, ion exchange, and electrostatic interactions, modified lignin-based adsorbents perform better and are more efficient at removing organic and heavy-metal pollutants.[186,187] Masliha *et al.* (2025) reported the process of functionalizing organosolv lignin, such as by grafting it with 3-aminopropyltriethoxysilane. This produces bio-based adsorbents that can extract and recover phosphates from wastewater, as shown in Fig. 7(c). These adsorbents exhibit monolayer adsorption with capacities (21 mg g^{-1}); the solution ionic content and pH influence their efficiency.[177] Xie *et al.* (2021) synthesized carboxyl-modified lignin nanospheres (ECLNPs) for Pb^{2+} and Cu^{2+} adsorption. A sample of raw lignin was transformed into a spherical shape with a diameter of 50 nm and a doubled carboxyl content of 0.66 mmol g^{-1}. Following pseudo-second-order kinetics and Langmuir isotherm behaviour, adsorption capacities for Pb^{2+} and Cu^{2+} reached 126.0 mg g^{-1} and 54.4 mg g^{-1}, respectively. Unmodified lignin has a much lower absorption (<30 mg g^{-1}). After 3 cycles, the ECLNPs maintained >80% efficiency, demonstrating exceptional structural stability and reusability.[188]

Zhang *et al.* (2022) produced a dual-modified LMM with sodium alginate and dopamine to enhance Pb^{2+} adsorption. After 3 cycles, the modified microspheres maintained 69% efficiency and demonstrated great selectivity toward Pb^{2+}, reaching a maximum capacity of 250 mg g^{-1}. The synergistic effects of amine and carboxyl groups, which enhanced surface complexation and electrostatic binding, were attributed to the improved performance. Unmodified alkali lignin exhibited a lower coordination ability and fewer functional sites, resulting in a reduced adsorption capacity of about 60 mg g^{-1}.[189] Wang *et al.* (2025) introduced thiourea-functionalized lignin (TUFA-L), which contains sulphur and nitrogen heteroatoms for Cr^{6+} adsorption.[186] The modified lignin had a high adsorption capacity of 593.90 mg g^{-1} at 40 °C more than 10 times that of raw lignin. The pseudo-second-order kinetics of adsorption and the Langmuir isotherm demonstrated that monolayer chemisorption was dominated by electrostatic attraction, coordination, and reduction processes. The TUFA-L demonstrated the benefits of heteroatom functionalization by preserving structural stability and reusability across multiple adsorption–desorption cycles.[186] The adsorption potential of lignin increases significantly by modification, with capacities rising

from less than 50 mg g^{-1} in raw lignin to 100–600 mg g^{-1} in modified forms. Functionalization enhances selectivity, stability, and reusability by introducing active groups (–COOH, $–NH_2$, –SH) that facilitate metal ion complexation, π–π interactions, and hydrogen bonding. Therefore, for effective and environmentally friendly wastewater filtration, modified lignin adsorbents represent a sustainable improvement over raw lignin.[98]

7. Adsorption mechanisms and modelling

The adsorption mechanism of biochar for removing organic and inorganic pollutants involves various mechanisms. The most common mechanisms are electrostatic interactions, ion exchange, pore filling, hydrogen bonding, and π–π interactions, as illustrated in Fig. 8.

7.1 Types of adsorption interactions and mechanistic pathways

7.1.1. Ion-exchange. Ion exchange is the process of exchanging dissolved metal ions for protons or ionised cations that are present on the surface of biochar. The size of the metal ions and the surface functional groups of the biochar have a major role in this exchange effectiveness. The target metal ions replace the positively charged ions bound to the biochar surface. The ionic radius of the participating ions, charge differential, and bonding type are significant factors affecting this process.[190] The cation exchange capacity (CEC) of biochars, influenced by their surface functional groups, determines their ability to remove ions, including heavy metals, from the water.[191] Li *et al.* (2020) produced six magnesium-modified from banana straw, cassava straw, Chinese fir straw, corn straw, camellia nut shells, and taro straw and the resulting materials were named biomass feedstocks and introduced Mg^{2+} *via* impregnation. Their findings indicated that all the biochar showed significant adsorption capabilities for heavy metals such as Cd^{2+}, Cu^{2+}, and Pb^{2+}. The high Mg content and abundant surface functional groups enabled effective complexation and ion-exchange with metal ions. Consequently, cation exchange and mineral precipitation were identified as the primary mechanisms governing the adsorption process.[192]

7.1.2. Electrostatic attraction. This is the most important mechanism, which involves the adsorption of ionizable organic compounds onto the positively charged surface of the biochar *via* electrostatic interactions. Its efficiency in attracting or repelling pollutants depends on the pH and ionic strength of the aqueous solution.[193,194] It also varies with the biochar's point of zero charge, which influences how the surface interacts with charged ions. The effect of ionic strength on the electrostatic interaction of ions cannot be ignored, as it can significantly affect the rate of ionic bond formation.[194] Electrostatic interactions increase adsorption by establishing a strong attraction between the negatively charged adsorbent surface and positively charged metal ions. For example, Wang *et al.* (2024) observed that when the pH exceeds the pH_{pzc}, functional groups such as –COOH, –OH, and $–NH_2$ undergo deprotonation, resulting in a net negative charge on the biochar surface. The modified FeNi-RSN-(OH) (NH_2) and FeNi-RSN-OH composites had a negative surface charge, extensive surface area, and several functional groups that collectively enhanced electrostatic adsorption.[195] Yang *et al.* (2024) reported that electrostatic forces and ion exchange were identified as the primary mechanisms governing Pb^{2+} and Cd^{2+} adsorption from aqueous solutions. Their analysis revealed that electrostatic interactions accounted for 19.34% of Pb^{2+} removal and 18.06% of Cd^{2+} removal. Also, the incorporation of amino groups significantly improved the biochar's electrostatic adsorption performance.[196]

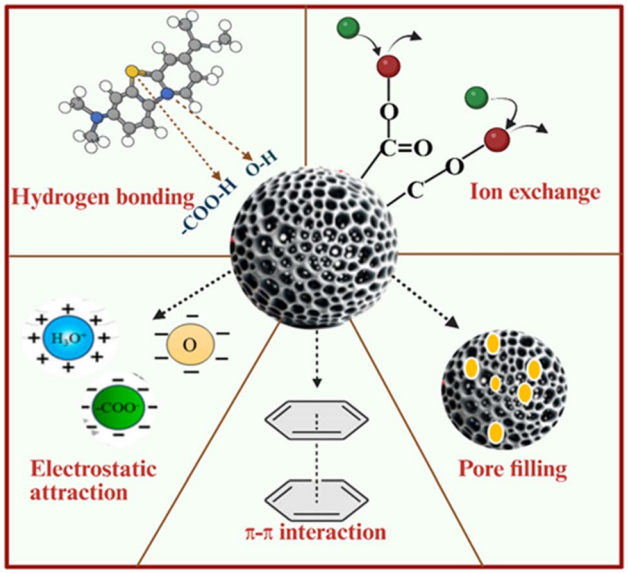

Fig. 8 Various types of adsorption mechanisms using biochar or bio-adsorbents.

7.1.3. H-bonding. Hydrogen bonding (H-bonding) is a powerful type of dipole–dipole interaction between a hydrogen donor and an acceptor atom. The donor hydrogen is often bonded to electronegative atoms, such as nitrogen, oxygen, and fluorine, within functional groups such as –COOH, –OH, $–NH_2$, or other electron-rich systems. These donor and acceptor groups, which are present on biochar surfaces or organic pollutants, can interact to form hydrogen bonds.[197] Zhu *et al.* (2018) studied the adsorption of methylene blue from cattle manure-derived biochar (CMB) at low temperature. A study showed that the oxygen-containing functional groups (-COOH, –OH) present on CMB contribute to the adsorption of methylene blue (MB) through hydrogen bonding. As the pyrolysis temperature increases, these surface functionalities are progressively lost, making the biochar more hydrophobic. Consequently, its affinity for polar molecules such as MB declines, leading to a noticeable reduction in adsorption capacity.[198]

7.1.4. Pore filling. The organic contaminants enter and occupy the mesopores (2–50 nm) and micropores (<2 nm) on the biochar surface. The extent of pore filling is influenced by the characteristics of the biochar, polarity and type of the organic contaminant.[193] Dou *et al.* (2022) pyrolysed pre-oxidised tilapia fish scales (PTFS) powder and activated it by KOH under

different conditions. Pore-filling mechanism was a major contributor in this study. The modified biochar had a larger surface area and more micro- and mesopores. These pores allowed pollutant molecules to enter and become physically trapped. The improved pore structure also helped with faster diffusion into the carbon matrix. As a result, pore filling significantly boosted the overall adsorption performance.[199] Overall, effective pore filling happens when the biochar has a low volatile content, and the organic pollutants are present in minimal concentrations.[193]

7.1.5. π– π interaction. The π–π interaction is a weaker type of dipole interaction compared to hydrogen bonding. This interaction refers to the attraction between neutral organic molecules and electron-rich π-systems. Delocalized electrons in π-bonding structures, such as C=C double bonds and aromatic rings, can interact with polar molecules or other π-systems. As the pyrolysis temperature rises, the aromatic character of biochar often intensifies due to the breakdown of aliphatic components. Guo *et al.* (2023) produced the corn straw biochar and studied the adsorption of Rhodamine B (RhB) from water. The π–π interactions significantly enhance RhB adsorption by enabling strong stacking between the dye aromatic rings and the aromatic domains of biochar. Moreover, in combination with hydrogen bonding, these interactions further increase π-electron density and shorten the distance between interacting rings, thereby strengthening overall binding. This synergy contributes to the exceptionally high adsorption capacity of biochar for RhB, making π–π stacking a key mechanism in its effective removal from water.[200]

7.2. Adsorption isotherm

One of the main goals of studying adsorption thermodynamics is to determine the relationship between the adsorbate's equilibrium quantity (Q) and its equilibrium concentration (C_e). This basically involves understanding a system's final adsorption behaviour under different starting circumstances. Important factors, including the maximum adsorption capacity (Qm), the adsorption intensity, and the underlying adsorption process, can be determined by employing suitable models to analyse the thermodynamic data.

7.2.1. Langmuir isotherm. The Langmuir isotherm describes the monolayer adsorption on a uniform surface with identical sites. Its linear equation can be written as:

$$\frac{1}{Q} = \frac{1}{Q_m} + \frac{1}{bQ_mC_e} \quad (1)$$

Here Q represents the is the adsorption capacity (mmol g^{-1}), C_e refers to the equilibrium concentration in the solution (mmol L^{-1}), Q_m is the highest amount of adsorption, and b is the Langmuir adsorption constant (L $mmol^{-1}$). The value of Q_m and b will be obtained from the curve of $\frac{1}{Q}$ and $\frac{1}{C_e}$.[201] The enhanced Langmuir models based on binary adsorption are known as competitive and noncompetitive Langmuir models and are essentially monolayer adsorption models. The noncompetitive Langmuir model allows two adsorbates to share an adsorption site without interacting, while the competitive model allows just one. The Langmuir and the Freundlich models, empirical formulas, were fully expressed by the Langmuir-Freundlich model. Three models can be expressed using eqn (2)–(4):

Competitive Langmuir model:

$$q_{ei} = \frac{q_m K_{Li} C_{ei}}{1 + K_{Li} C_{ei} + K_{Lj} C_{ej}} \quad (2)$$

Noncompetitive Langmuir model:

$$q_{ei} = q_m \left(\frac{K_{Li} C_{ei} + K_{Lij} C_{ei} C_{ej}}{1 + K_{Li} C_{ei} + K_{Lj} C_{ej} + K_{Lij} C_{ei} C_{ej}} \right) \quad (3)$$

Langmuir-Freundlich model:

$$q_{ei} = \frac{q_m K_{LFi} {C_{ei}}^{1/ni}}{1 + K_{LFi} {C_{ei}}^{1/ni} + K_{LFj} {C_{ei}}^{1/ni}} \quad (4)$$

where q_{ei} represents the adsorption capacity of adsorbate i (in mmol g^{-1}), C_{ei} and C_{ej} are the equilibrium concentrations of adsorbates i and j (in mmol L^{-1}), q_m is the estimated maximum adsorption capacity for adsorbate i (mmol g^{-1}), and K_{Li}, K_{Lj}, and K_{Lij} are Langmuir constants. Additionally, K_{LFi}, K_{LFj}, ni, and nj are the Langmuir-Freundlich model constants.[202] Zhou *et al.* (2022) studied the impact of pyrolysis parameters (temperature, duration, and heating rate) on biochar adsorption performance for Cu^{2+} and Zn^{2+} ions in water. Biochar was produced using optimal pyrolysis (422–425 °C, 2–3 h). Adsorption tests revealed that fitting to the Langmuir isotherm model resulted in maximal monolayer capacities of 210.56 mg g^{-1} (Cu) and 223.32 mg g^{-1} (Zn). The optimised biochar exceeded the non-optimised controls in terms of adsorption, demonstrating that monolayer chemisorption is dominant under equilibrium circumstances.[203]

7.2.2. Freundlich adsorption isotherm. Freundlich adsorption is basically used to describe the equilibrium relationship between the quantity of adsorbate adsorbed per unit mass of carbon and the concentration of adsorbate remaining in the solution. It can be represented as:

$$q_e = K_f C^{1/n} \quad (5)$$

here, q_e represents the total amount of adsorbate adsorbed per unit mass of carbon. K_f is a constant that indicates the adsorption capacity. C denotes the equilibrium concentration of the adsorbate in the solution. n is a constant that represents the effectiveness and strength of sorption.[204] Applying log on both sides of the equation, it can be written as,

$$\log q_e = \log K_f + \frac{1}{n} \log C \quad (6)$$

Plotting $\log q_e$ *versus* $\log C$ gives a straight line. As activated carbon's adsorption efficiency increases, the K_f value rises. The Freundlich isotherm fits well at low pressure but is less accurate at high pressures.[204] The research conducted by Gao *et al.* (2025) produced biochar (BCL) and its acid-base modified version (BCL-K-H). The biochar and acid treated biochar were examined

for adsorption of thiamethoxam (TH) and Rhodamine B (RhB). Adsorption data was fitted to both Langmuir and Freundlich isotherms. However, Freundlich model provided a better match (R^2 > 0.99) for pollutants, showing heterogeneous multilayer adsorption on modified biochar surfaces. The modified biochar had a higher Freundlich constant (K–F), indicating more active high-energy sites and a stronger pollutant attraction following pretreatment.[205]

7.2.3. Temkin adsorption isotherm. The Temkin adsorption isotherm includes a term that reflects the interactions among adsorbed molecules. It assumes that, at intermediate concentrations, the adsorption heat for each molecule falls linearly with increasing surface coverage, instead of decreasing logarithmically. This is based on the idea that binding energies are uniformly distributed up to a defined maximum value. The relationship is expressed through the following equation:

$$q_e = \frac{R_T}{b}\ln(A_T C_e) \tag{7}$$

$$q_e = \frac{R_T}{b_T}\ln A_T + \left[\frac{R_T}{b}\right]\ln C_e \tag{8}$$

$$B = \frac{R_T}{b_T} \tag{9}$$

$$q_e = B\ln A_T + B\ln C_e \tag{10}$$

In this model, B_T represents the Temkin isotherm constant, and A_T is the Temkin isotherm equilibrium binding constant (L g^{-1}). T is the absolute temperature measured at 298 K, B is a constant related to the heat of sorption (J mol^{-1}), and R stands for the universal gas constant (8.314 J $mol^{-1}K^{-1}$). The intercept and slope of the plot of q_t *vs.* ln t are used to get the values of A_T and B_T respectively.[206] Xian *et al.* (2018) studied the various isotherm models employed for biochar Cd(II) adsorption properties from waste mushroom substrate at varying pyrolysis temperatures. Compared to other models, Temkin and Langmuir isotherm suited the Cd(II) adsorption data better, indicating that chemically regulated adsorption *via* electrostatic interactions was a significant factor in the process and that the heat of adsorption dropped linearly with surface coverage.[122]

7.2.4. Radlich–Peterson adsorption isotherm. The Radlich–Peterson (R–P) adsorption isotherm is a combined model that integrates elements of the Freundlich and Langmuir isotherms into a single equation and expressed as:

$$Q_e = \frac{K_R C_e}{(1 + a_R C_e{}^g)} \tag{11}$$

The Redlich–Peterson constant (K_R) reflects the adsorption capacity of the system and is expressed in L g^{-1}. The parameter a_R is the isotherm constant of the model, with units of L mg^{-1}. The exponent g is a unitless value between 0 and 1 that indicates the level of heterogeneity in the adsorption process. When $g = 1$, the model reduces to the Langmuir isotherm, which represents monolayer adsorption. In contrast, when $g = 0$, it resembles the Freundlich isotherm, which characterises adsorption on heterogeneous surfaces.[207] Activated and modified bamboo biochar has been developed by Nguyen *et al.* (2025) to remove oxytetracycline. A mixed adsorption was indicated by the identical β values (0.74) and the best fit of the R–P model to both biochar (R^2 = 0.998 for steam activated biochar (B2) and 0.992 for CO_2 activated biochar (B1)), with B2 demonstrating superior adsorption owing to its larger capacity and B1 having a higher K_{RP}.[208]

7.2.5. Dubinin–Radushkevic (D–R) adsorption isotherm. The Dubinin–Radushkevich (D–R) adsorption isotherm is widely used to distinguish between physical and chemical adsorption of heavy metal cations by evaluating their mean free energy. The mathematical form of the D-R isotherm model is expressed as follows:

$$q_e = (q_s)\exp(-K_{ad}\varepsilon^2) \tag{12}$$

The above equation in a linearised form is shown as,

$$\ln q_e = (q_s)\exp(-K_{ad}\varepsilon^2) \tag{13}$$

Values of q_s and K_{ad} obtained by plotting a graph of ln q_e *versus* ε^2.

$$\varepsilon = RT\ln\left[1 + \frac{1}{c_e}\right] \tag{14}$$

B_{DR} value is a constant used to determine the mean free energy of adsorption in the transfer of each adsorbate molecule from an aqueous phase to the external surface of a solid. Herein mean free energy (E) is calculated as noted in equation.[209]

$$E = \frac{1}{\sqrt{2B_{DR}}} \tag{15}$$

Hanandeh *et al.* (2016) examined the adsorption of mercury (Hg^{2+}) using biochar generated at various pyrolysis temperatures (350–630 °C). The Dubinin-Radushkevich isotherm model best suited the experimental equilibrium data, implying that the adsorption involves pore-filling and energy distribution, which is compatible with the D–R model assumptions. The maximum adsorption capacity increased with pyrolysis temperature (84.9–104.6 mg g^{-1}). A pseudo-second-order model best fitted the kinetic behaviour, whereas thermodynamic analysis revealed a spontaneous and exothermic nature.[210]

7.3. Kinetic models

Kinetic models are commonly used to analyse adsorption data. The model that best fits explains how adsorption is taking place. The most used models include the pseudo-first-order, pseudo-second-order, Elovich, and intraparticle diffusion models.[211] The PFO model assumes that the adsorption rate is proportional to the adsorbent concentration, suggesting that physical adsorption dominates.[212] In contrast, the PSO model assumes that the adsorption rate is proportional to the adsorbate concentration at the active sites, suggesting that chemical adsorption is the primary mechanism.[213,214] These models help identify the main controlling mechanisms of the reaction process, such as diffusion and surface adsorption. A higher

model fit indicates that the reaction process aligns well with the model's assumptions, suggesting that the model effectively explains the underlying mechanisms.[215]

7.3.1. Pseudo first order. The differential equation for the Pseudo-first-order model (PFO) is expressed as follows.[216]

$$\frac{\mathrm{d}qt}{\mathrm{d}t} = k_1(q_e - q_t) \quad (16)$$

where q_e is the methane adsorbed amount when the pressure reaches equilibrium in cc g^{-1}, q_t is the methane adsorbed amount at time t in cc g^{-1}, k_1 is the adsorption rate constant of PFO in 1 min^{-1}, and t is the adsorption time in min. Integrating eqn (16) for the initial condition, $t = 0$, and $q_t = 0$, the linear equation is obtained

$$\ln(q_e - q_t) = \ln q_e - k_1 t \quad (17)$$

From eqn (5), the plot of $\ln(q_e - q_t)$ *versus* t is linear on a semi-log plot, and q_e and k_1 can be calculated according to the slope and the y-intercept of $\ln q_e$. Thus, q_t can be calculated according to q_e, k_1, and t.Rearranging eqn (17), the adsorption amount at different times can be calculated by.[217]

$$q_t = q_e(1 - e^{-k_1 t}) \quad (18)$$

7.3.2. Pseudo-second order. The pseudo-second-order equation is the model that best describes the adsorption of species in solution. The appropriate boundary conditions for its integration are $q\,(t = 0) = 0$ and $q\,(t = t) = q_t$, and the integrated form is represented in eqn (19). The parameter k_2 is the pseudo-second order adsorption rate constant (g mg^{-1} h^{-1}), and it depends on the operating conditions; t is the time (h), and q is the sorbate uptake (mg g^{-1}).

$$\frac{d_{q_t}}{d_t} = k_2(q_e - q_t)^2 \quad (19)$$

7.3.3. Intraparticle diffusion model. The intraparticle diffusion model describes adsorption as a multi-stage process. During this process, the adsorbate moves into the pores of the adsorbent, revealing the diffusion barriers that can occur in biosorption. These barriers indicate that the adsorbate may encounter resistance as it travels toward the adsorbent's internal active sites.

The classical intraparticle diffusion model $q_t = kt^{\frac{1}{2}}$ or $q_t = kt^{\frac{1}{2}} + b$ where q_t is the adsorption amount at time t, k is the sorption rate constant, and b is a constant, has been widely used to simulate diffusion kinetics during the adsorption process[205]

7.3.4. Elovich model. This model is used to further describe pseudo-second-order kinetics, assuming the sorbent surface is energetically heterogeneous. Elovich model has been used for the chemisorption of gases onto the heterogeneous surfaces of adsorbents[206] (Table 6).

The Elovich equation is given as:

$$\frac{d_{q_t}}{d_t} = \alpha e^{-\beta_{q_t}} \quad (20)$$

where α is the initial rate of adsorption (mg g^{-1} min^{-1}), β is the desorption constant (g mg^{-1}) during an experiment. To simplify the equation, it can be assumed that: $\alpha\beta t >> t$ and applying boundary conditions; $q_t = 0$ at $t = 0$ and $q_t = q_t$, at $t = t$, eqn (5) becomes.[217]

$$q_t = \frac{1}{\beta}\ln(\alpha\beta) + \frac{1}{\beta}\ln(t) \quad (21)$$

8. Lignin-derived carbons for oil–water separation

8.1. Surface wettability and superhydrophobicity principles

Superhydrophobic/superoleophilic or superhydrophilic/underwater superoleophobic wettability membranes improve separation performance by allowing selective oil or water permeability.[223] The equilibrium contact angle (θ) of a liquid on a solid is a measure of wettability, which is determined by the material's micro texture and surface chemistry.[224] Superhydrophobic surfaces with contact angles exceeding 150° and low sliding angles are highly desirable for oil–water separation due to their self-cleaning and anti-wetting properties.[225] Yun *et al.* (2025) developed a lignin-derived carbon flake (L_{cf}) sorbent by employing lignin as a binder to coat melamine foam with carbonized lignin particles. Across a range of organic solvents, the modified foam had a WCA of 139° and an oil sorption capacity of 49–105 g g^{-1}. Additionally, it demonstrated hydrophobicity and mechanical resilience, maintaining performance across multiple reuse cycles. This demonstrates the role of carbon derived from lignin in reusable, eco-friendly oil sorbents.[226] Wu and Jiang (2025) enhanced oil–water separation by infusing silicone oil, which reduced interface hysteresis while maintaining selective wettability on polydimethylsiloxane. The surfaces exhibited self-healing properties and served as an adaptable alternative to intricate modification techniques, with potential applications in liquid transport systems.[227] Li *et al.* (2022) produced a superhydrophobic coating by spraying polyvinyl alcohol (PVA), cellulose nanocrystals (CNCs), and lignin nanospheres (LNPs) onto wood surfaces. This was followed by surface fluorination using 1H,1H,2H,2H-perfluorooctyltrichlorosilane (FOTS). The final coating exhibited a water contact angle of 162, demonstrating good abrasion resistance and outstanding UV resistance for 7 h at 1000 W. These characteristics were attributed to FOTS's low surface energy. The combined surface roughness from LNPs and CNCs demonstrates the promise of biodegradable biopolymers in strong superhydrophobic design.[225] These findings show that lignin-derived materials can produce strong superhydrophobicity and high-performance oil–water separation by combining micro/nano-structuring with surface energy management.[225,226]

8.2. Carbon sponges, foams, aerogels and membranes

Porous carbon structures, such as sponges, foams, aerogels, and membranes, have proven highly effective in oil–water separation due to their tunable 3D networks, large surface areas, and inherent hydrophobicity. For example, lignin is an abundant aromatic

Table 6 Different types of kinetic models of adsorption for pollutant removal from wastewater

Adsorbent	Adsorbate	Conversion technologies	Temperature	Adsorption kinetics	Isotherm	Result	References
Direct red 23	Pig manure biochar	Pyrolysis	800 °C	The pseudo-first and second-order rate model	The Freundlich model and the intra-particle diffusion model were the best-suited models	A maximum adsorption capacity of 2.19×10^{-5} mol g^{-1} was obtained at pH 2.20 and 25 °C	218
Cd^{2+}	Silica gel modified corn straw biochar (SGB)	Pyrolysis	500 °C	Pseudo-second order waste is well fitted	The Langmuir model is suited since it has the highest R^2 (0.9890)	The maximum adsorption capacity of SGB was 38.08 mg g^{-1}	219
Cd^{2+} and Cu^{2+}	Gasifier biochar (GCB) from Pinewood	Gasification	700–900 °C	Pseudo-second order	The Freundlich model (Cd) and the Langmuir model (cu) were well-suited	Cd(II) adsorption capacity 86.2 mg g^{-1} & Cu^{2+} adsorption capacity 68.6 mg g^{-1}	220
As(V)	Wheat strawsCerium–manganese modified biochar	Pyrolysis	873 K	Pseudo-second order kinetics	The Langmuir model fits the data well, with an R^2 value of 0.9910	108.88 mg g^{-1}	221
Methylene blue (MB)	NaOH modified rape straw biochar(M-RSB_{600})	Pyrolysis	600 °C	Quasi-second-order kinetics with adsorption kinetics of MB onto RSB_{600} and M-RSB_{600} ($R^2 > 0.98$)	Freundlich and Temkin models better reflected the equilibrium data ($R^2 > 0.95$)	250.30 mg g^{-1}	222
Methylene blue	Cattle manure-derived low temperature biochar (CMB)	Pyrolysis	200 and 800 °C	Pseudo-second order kinetics	Langmuir model	CMB_{200} resulted in the good adsorption of 241.99 mg g^{-1} compared to the CMB_{800}	198
Pb^{2+} and Cd^{2+}	Amino/MnO_2 combined rice straw derived biochar	Pyrolysis	600 °C	Quasi-second order kinetics	Langmuir model	Adsorption of 159.25 mg g^{-1} for Pb^{2+} and 70.84 mg g^{-1} for Cd^{2+}	196

biopolymer that can be transformed into carbon sponges or aerogels with oleophilic surfaces and hierarchical porosity, allowing for rapid oil absorption and simple regeneration (*e.g.*, by thermal treatment).[226,228] Barker-Rothschild *et al.* (2024) derived porous carbons from lignin, as shown in Fig. 9(a), which were primarily produced by pyrolysis. It is a thermal decomposition process where lignin is heated in an inert atmosphere (above 600 °C). This results in the breakdown of complex chemical bonds and the formation of carbon-rich solids with huge micropores and mesopores. The pyrolysis proceeds through various stages, including moisture evaporation, mainly decomposition (between 250–500 °C) and carbonisation (above 500 °C). Therefore, this increases

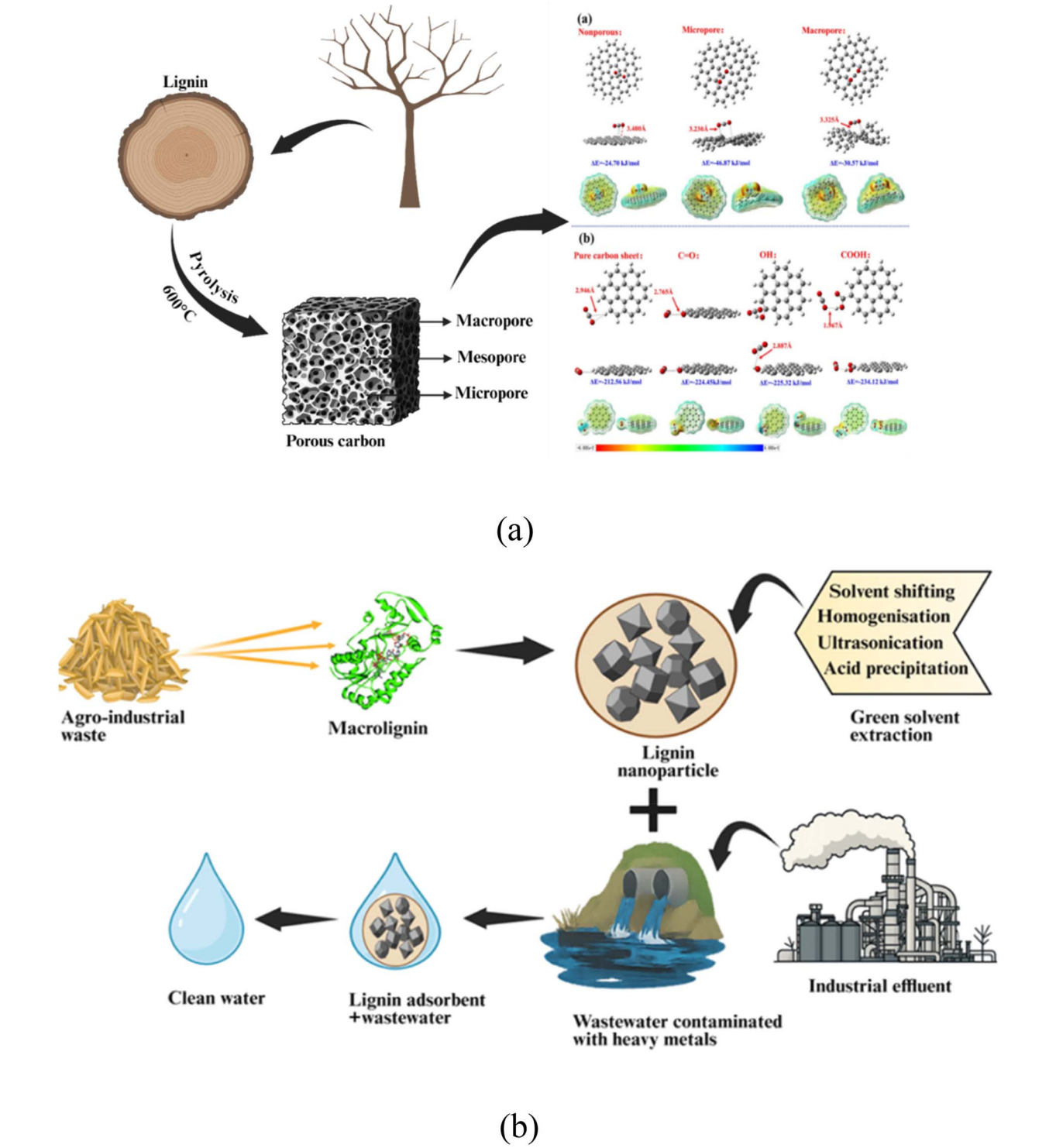

Fig. 9 (a) Schematic overview of lignin-derived porous carbon formation and surface chemistry by pyrolysis (redrawn from Barker-Rothschild *et al.* (2024)[229]). (b). Agro-industrial lignin waste extraction and use of lignin nanoparticles in adsorption (redrawn from Nargotra *et al.* (2025)[230]).

aromatic condensation, leading to biochar formation with surface functional groups, such as hydroxyl and carbonyl groups, that enhance adsorption.[229] Yun *et al.* (2025) developed a super-hydrophobic oil sorbent by applying a lignin-based carbon-flake layer to standard melamine foam. The modified foam (Lcf-L-MF) absorbed 49–105 g of oil per gram of foam with various organic solvents and exhibited a water contact angle of 139°, indicating sufficient hydrophobization.[226] Furthermore, this lignin-carbon foam demonstrated exceptional recyclability, retaining more than 83% of its initial adsorption capacity even after 20 sorption-desorption cycles.[226] Feng *et al.* (2024) produced lignin-based carbon fibrous aerogels that are self-supported and reinforced with graphene oxide (GO) nanosheets. This concept produced aerogels with linked macro- and mesopores by carbonising hardwood kraft lignin ultrafine fibres and graphene oxide (GO) into a coherent 3D network. The LCA/GO composites showed exceptional oil sorption and were very hydrophobic (water contact angles 132–136°). For example, the LCA/GO7.5 sample absorbed organic liquids at rates up to 55.9 g g^{-1} (for CCl_4) and 17–56 g g^{-1} for various oils. However, this material showed durability while delivering ultrahigh flux in dynamic separation testing.[228] Improving lignin-derived carbon sponges, foams, aerogels (and membranes) for effective oil–water separation requires rational structural design. This includes producing hierarchical porosity, rough hydrophobic surfaces, and composite frameworks. In each instance, optimised oil absorption capacity, rapid sorption kinetics, and long-lasting reuse were enabled by customising the 3D architecture and surface chemistry. Thus, highlighting the crucial role that material design plays in developing carbon-based separation media.[226,228]

8.3. Oil sorption mechanisms

The surface chemistry, porosity and wettability properties that determine interactions with oil molecules play a major role in oil sorption by lignin-derived and biomass-based materials. Optimising material design for oil–water separation applications needs a thorough understanding of the underlying sorption mechanisms.[96] Hu *et al.* (2024) studied biochar derived from 3 different lignin types and found that $ZnCl_2$-activated lignin-derived carbon had the highest Congo red adsorption capacity of 2156.77 mg g^{-1}. Due to its customised pore structure and high aromatic carbon content, which followed a Langmuir-type monolayer adsorption mechanism.[96] Mostovoy *et al.* (2025) demonstrated that sorbents based on chemically modified buckwheat husk can achieve oil sorption capacities of up to 6.1 g g^{-1}. Their robust physical entrapment and capillary-driven uptake of petroleum compounds even after repeated reuse cycles were attributed to their macro-porous fiber structure, high specific surface area (67.00 m^2 g^{-1}) and hydrophobic surface.[231] The hierarchical porous architectures, surface area, and surface chemistry of lignin-based and biomass-derived materials collectively enhance capillary action and selective oil affinity, the main factors influencing their oil sorption effectiveness. Superhydrophobic and highly porous materials exhibit rapid sorption, robust reusability, and high oil absorption capacity (up to 91.6 g g^{-1}), making them ideal candidates for oil–water separation applications.[11]

8.4. Demulsification and emulsion treatment

In wastewater treatment and petroleum production, demulsification is crucial for separating stable oil–water emulsions. Since conventional chemical demulsifiers are expensive and harmful to the environment, sustainable substitutes made of renewable biomass resources are being developed.[232] Jiang *et al.* (2023) demonstrated that poly-oxyethylene polyoxypropylene quaternized polyoxyolefins (PR demulsifiers). They performed in low temperature demulsification, achieving >60% oil separation in an hour at room temperature *via* two mechanisms: flocculation of suspended particles and interfacial tension reduction.[233] Gao *et al.* (2022) demonstrated that lignin nanoparticles (LNPs) work as highly effective, recyclable, selective emulsifiers that can stabilise kerosene emulsions with >95% stability (up to 6 months). Additionally, pH-responsive demulsification allows for quick oil–water separation (>85% efficiency) and reuse of the lignin emulsifier for up to 5 cycles, showing superior environmental advantages over synthetic demulsifiers.[234] All these studies show that demulsification through interfacial tension reduction, particle flocculation, pH-responsive mechanisms, and magnetic responsiveness with quantifiable separation efficiencies (60–99%). The rapid kinetics provide possibilities for ecologically friendly industrial applications using bio-based and lignin-derived materials for sustainable emulsion treatment.[234]

8.5. Performance indicators (flux, capacity, recyclability)

Flux, sorption capacity and recyclability are the 3 main metrics used to assess the practical usefulness of oil–water separation materials. These performance measures help determine the material performs in practical.[235,236] Kim *et al.* (2021) developed a dual-functional mesh membrane modified by atmospheric cold plasma, which exhibited remarkable flux and excellent separation efficiencies. Under oil–water emulsion testing, they reported continuous operation with selectivity above 99.9% and water and oil penetration rates of about 900 L m^{-2} h^{-1} and 400 L m^{-2} h^{-1}, respectively.[235] Alsawy *et al.* (2022) studied biochar regeneration techniques and demonstrated that desorption techniques are matched to the adsorption mechanism, materials can maintain significant performance with repeated use. They found that while acid regeneration (HCl and HNO_3) frequently resulted in structural degradation and reduced capacity to below 70% after repeated use. The alkaline regeneration (NaOH) enabled biochar to retain up to 90–95% of its initial adsorption capacity for organic pollutants, such as dyes and phenols, over five cycles. In contrast to biochar treated with strong acids, which could leach active sites and collapse pore structures. Thus, the study highlighted that biochar regenerated using softer alkaline agents preserved surface area and porosity more successfully.[236] The findings validate that the most suitable materials for sustainable oil–water separation applications are those that combine high flux, big capacity, and long-lasting recyclability when customised for separation and regeneration settings.[235,236]

9. Regeneration and reuse

9.1. Desorption and regeneration techniques

Desorption and regeneration include chemical (acid/base/complexing elution), thermal (high temperature) decomposition, and other non-thermal techniques (such as wet oxidation and electrochemical methods). Restoration employed biochar/biocarbon adsorbents for reuse to remove or degrade adsorbed pollutants. High temperatures or aggressive eluents may restore capacity, but they may also harm the pore structure. The choice of approach is greatly influenced by the adsorbate (organic *vs.* inorganic), the principal adsorption mechanism (physisorption *vs.* chemisorption), and the adsorbent thermal and chemical durability.[236] Alsawy *et al.* (2022) examined biochar regeneration techniques and found that mesoporous magnetic biochar retained approximately 92.10% of its removal efficiency after five adsorption–desorption cycles. Thus, this demonstrates the effectiveness of 0.1 M NaOH in maintaining the adsorption capacity. Non-magnetic biochar, on the other hand, demonstrated a more notable decrease, underscoring the contribution of pore structure to improving regeneration stability.[236] Tan *et al.* (2023) studied the regeneration of nitric acid-modified empty fruit bunch biochar using different eluents. Among 6 chemicals examined, 0.1 M HCl achieved the highest initial Na^+ desorption of 66.23%, but capacity fell to 18.85% by the 6th cycle, demonstrating gradual structural deterioration with repeated acid exposure.[237] The findings from these studies demonstrate that thermal and chemical regeneration can effectively enhance biochar performance. Also, its long-term sustainability is dependent on the kind of pollutants being targeted, the content of the sorbent, and the regeneration environment.[237]

9.2. Adsorbent stability and recyclability

The economic and environmental sustainability of wastewater treatment depends on the sorbent's ability to retain its physical integrity and adsorption capability across several cycles of use. Stability and recyclability ensure lower material costs, less waste production and long-term use of adsorbent materials under operating conditions.[238–240] Gkika *et al.* (2025) demonstrated that several adsorbents derived from agro-industrial waste, including chemlali olive pruning residues and maize biomass, maintained 96.22% desorption efficiency with NaOH while exhibiting structural stability over several cycles, indicating their potential for long-term use in chromium removal applications.[240] Alcalde-Garcia *et al.* (2023) examined the performance of biopolymer-based hydrogels and composites. Therefore, demonstrating that some chemical regeneration techniques, particularly CO_2 bubbling and alkaline desorption. Additionally, they can maintain material integrity and adsorption efficiency over up to 5 reuse cycles, although efficiency often depends on the type of pollutant and the interaction mechanism.[238] The structural design and regeneration method play critical roles in ensuring high recyclability and long-term stability of adsorbents for sustainable water treatment applications.[238–240]

9.3. Oil recovery and reuse

Sustainable operation in oil–water separation systems depends on efficient oil recovery from sorbents. In addition to allowing sorbent and oil to be reused, high recovery efficiency reduces resource waste and secondary contamination.[241–243] Ren *et al.* (2025) derived a bio-based oil adsorbent from chemically altered sphagnum moss. It demonstrated good hydrophobicity, quick adsorption kinetics and an oil adsorption capacity of 22.756 g g^{-1} for motor oil. After 10 regeneration cycles using rotary evaporation, it maintained more than 90% of its adsorption capacity, exhibiting good selectivity and reusability for oil–water separation.[241] Li *et al.* (2023) explored the use of deep eutectic solvents (DES) in biomass pretreatment and lignin extraction, emphasising recovery techniques such as membrane filtration and rotary evaporation. The economic and environmental characteristics of biomass valorisation operations are greatly improved by these recovery procedures, which allow for more than 90% recycling efficiency of DES.[243] Zaarour *et al.* (2023) reported oil sorption capacities ranging from 80% to over 500%, depending on fabric type and alteration, and summarised developments in textile-based sorbents for oil spill cleanup. Textile sorbents demonstrated mechanical endurance after 100 abrasion cycles. It retained over 96% separation efficiency after 30 reuse cycles, indicating its scalability and efficacy for oil–water separation applications.[242] Sustainable resource management and environmental preservation rely on the recovery and reuse of oil. High recovery rates of up to 99% are made possible by effective recovery techniques, including solvent extraction, adsorption with bio-based materials, and sophisticated recycling methods. Therefore, ensure material reusability across multiple cycles. This significantly decreases pollution and conserves resources for industrial and ecological benefits.[241–243]

9.4. Valorization of spent adsorbents (catalysts, electrodes, soil recoveries)

Valorization of spent adsorbents, such as catalysts, electrodes and soil recovery materials is essential for resource recovery and sustainable waste management, turning waste into useful secondary products for industrial and environmental uses.[244,245] Rial *et al.* (2022) investigated the potential applications of spent adsorbents for the removal of heavy metals and dyes. It emphasises that bio-based spent adsorbents can maintain high heavy-metal adsorption capacities of up to about 100 mg g^{-1} after their first use. For example, magnetic chitosan composites demonstrated maximum adsorption efficiencies of 99.98% for Cu^{2+}, 93.69% for Cd^{2+}, and 83.81% for Zn^{2+}. The circular economy concept was promoted by the effective repurposing of used adsorbents as catalysts, achieving up to 99% yield in acetophenone production, and as additional cementitious materials that improved construction applications.[245] Alcalde-Garcia *et al.* (2023) presented a thorough analysis of desorption and regeneration techniques for hydrogel composites and biopolymeric adsorbents. By revealing regeneration efficiencies exceeding 90% over several cycles and desorption efficiencies of up to 98% for heavy metals using acid eluents such as HCl at pH 1. After 5 cycles, thermal regeneration at moderate temperatures (50 °C) retained

approximately 82% of the adsorption capacity.[238] The ultrasonic regeneration maintained over 96% of the adsorption capacity with much shorter processing times, demonstrating economical and ecologically friendly valorisation pathways.[238] A sustainable method of waste management with proven high efficiency and reusability is the valorisation of used adsorbents by regeneration, repurposing as catalysts, electrodes or construction additives. Further studies and the development of these methods are necessary to fully benefit from a circular economy framework, economic and environmental advantages.[238,244,245]

10. Industrial applications and case studies

10.1. Industrial wastewater treatment

Urbanisation and industrial growth are increasing rapidly in developing countries. This wastewater contains harmful chemicals. These chemicals can pose a threat to human health, damage the environment, and negatively impact the economy if not treated properly.[193] Industrial effluents arise from a variety of activities, including smelting, chemical manufacture, dye and leather processing, battery production, pharmaceutical companies, and mining operations. These wastewaters often contain two types of pollutants: organic compounds and heavy metals.[246] Industrial wastewater can be treated through various methods, including chemical approaches such as Fenton oxidation and electrochemical oxidation, physical methods such as adsorption and membrane filtration, and biological treatment procedures. According to the United States Environmental Protection Agency (USEPA), adsorption is regarded as one of the most effective and reliable methods for wastewater treatment. The adsorption technique could achieve the removal efficiency of up to 99.9%.[247] Biochar (BC) is a carbon-rich material formed by pyrolysis of biomass at regulated temperatures (300–900 °C) under oxygen-limited conditions. Nargotra *et al.* (2025) utilised agro-industrial lignin waste for the extraction and application of lignin nanoparticles for the adsorption of pollutants (Fig. 9(b)), which were employed to treat contaminated water containing industrial waste. The sustainable pathway for converting agro-industrial waste into lignin nanoparticles *via* green solvent extraction methods. These lignin-based nano-adsorbents are applied to industrial wastewater contaminated with heavy metals, enabling efficient pollutant removal. The process highlights waste valorization, eco-friendly material synthesis, and effective water purification, ultimately producing clean water while addressing environmental pollution and promoting circular economy-based wastewater treatment strategies.[230]

10.2. Oil spill cleanup technologies

Oil spills are a significant environmental concern associated with the oil and gas industry. They often occur due to pipeline and tanker corrosion, operational errors during production, or transportation-related circumstances.[248,249] Oils are complex mixtures with a wide range of physical characteristics that significantly impact the selection of restoration techniques. During spill cleanup, viscosity and the ability to form emulsions (linked to water content) are the most important factors to consider.[250] The concept of the maximum oil encounter rate (MOER), which represents each method's optimum capability under ideal conditions, was developed to better assess the efficacy of different technologies in large-scale disasters. Dispersants have the highest MOER of any cleanup approach, followed by skimming and *in situ* burning.[250] Akpomie *et al.* (2024) examined the efficiency of biochar made from Populus nigra leaves (PLBC). The biochar was produced through low-temperature pyrolysis at 350 °C. Furthermore, the characterisation revealed the presence of functional groups and surface pores in PLBC, which are suitable for oil adsorption, demonstrating its effectiveness as a low-cost sorbent for removing motor oil from water.[251] Hoang and Pham (2021) developed a novel absorbent material composed of polyurethane foam combined with rice straw for removing oil spillage and hazardous heavy metals from marine environments. Four variations of the absorbent were tested, differing in rice straw size and percentage. The sample comprising 25% rice straw with a fiber size of 0.5 mm demonstrated the highest oil absorption capacity and oil removal efficacy for crude oil, fuel oil, diesel, and petroleum. It also exhibited strong uptake of heavy metals such as Cd^{2+}, Pb^{2+}, and Hg^{2+}, reaching equilibrium within 60–120 min. Finally, the results show that this low-cost, biomass-based PU rice straw composite is a potential material for effective marine pollution treatment.[252]

10.3. Biorefinery waste valorization

Lignocellulosic biorefineries produce considerable amounts of residual biomass from agricultural and forestry sources. These residues provide an inexpensive and readily available feedstock for value-added processing. Due to their high cellulose, hemicellulose, and lignin content, they are ideal for circular economy frameworks. These materials can be efficiently transformed into high-value products through thermochemical, biochemical, and combined conversion pathways.[253,254] Bentahar *et al.* (2024) evaluated the potential of biorefinery by-products as adsorbent materials for removing methylene blue (MB). Fitting the adsorption data to the Langmuir model indicated that biochar-OH and humins-lignin biochar adsorbed methylene blue in a monolayer pattern. The maximal monolayer capacities were found to be 48.78 mg g^{-1} and 30.12 mg g^{-1}, respectively. These data demonstrate that both adsorbents are highly efficient in capturing cationic dyes.[254] Furthermore, Shahid *et al.* (2019) investigated the development of a microalgal biorefinery utilising combined biological and thermochemical processes. Mixed cultures of *Chlorella* sp. and *Bracteacoccus* sp. grown in municipal wastewater produced 12 g L^{-1} of biomass, and they removed 68% of nitrates and 75% of phosphates. The lipid-extracted biomass showed a three-stage pyrolysis profile at heating rates of 10–40 °C min^{-1}, with activation energies of 182–256 kJ mol^{-1}, indicating favourable product formation. It was noticed that the strong potential for simultaneous biomass and energy production alongside wastewater treatment.[255] Pyrolysed the industrial effluent-derived lignin at 380 °C with different additives, including H_3BO_3, $ZnCl_2$, and KOH, yielding

Table 7 Lignin-derived materials for the treatment of wastewater

Type of wastewater pollutant	Lignin-derived material	Adsorption model	Treatment mechanism	Results	References
Methylene blue dye	Lignin nanoparticles	Langmuir (best) and Freundlich model	Electrostatic repulsions	Maximum MB adsorption of about 334.4 $m^2 g^{-1}$	169
Methylene blue (MB dye)	Lignin-derived porous carbon (LPC)	Langmuir isotherm model	Electrostatic interaction, hydrogen bonding and π–π interactions	High specific surface area (3382.32 $m^2 g^{-1}$), high MB adsorption capacity (1119.18 mg g^{-1})	257
Heavy metal (Cd^{2+})	Virgin and calcined lignin	Langmuir and Freundlich model		Calcined lignin (lig 800) was the best for Cd^{2+} removal, with an adsorption capacity of 91.30 mg g^{-1}	258
Cr^{4+} heavy metal	Demethylated alkaline lignin	Langmuir, Freundlich and Temkin	Electrostatic interaction	Cr^{4+} adsorption of 703.6 mg g^{-1}	259
Sb^{3+} heavy metal	Amino functionalized Lignin-based biochar	Langmuir and Freundlich	Complexation, ligand exchange and hydrogen bonding	Maximum of 371.7 mg g^{-1} adsorption capacity of Sb^{3+}	260
Congo red dye	Lignin-based magnetic adsorbent	Langmuir, Freundlich, Temkin thermodynamic model	Electrostatic interactions, hydrogen bonds, and π–π interactions	Maximum adsorption of 218.2 mg g^{-1}	261
Malachite green (MG) and Pb^{2+}	Lignin-based adsorbent (C-SAL)	Adsorption isotherm models	Adsorption through electrostatic, hydrogen bonding and π–π interactions	Adsorption of 203.45 mg g^{-1} for MG and 115.67 mg g^{-1} Pb^{2+}. Good recyclability	262
Phosphate and nitrate from wastewater	Quaternary ammonium modified alkaline lignin (cationic lignin)	Langmuir and Freundlich isotherm models	Electrostatic repulsion	Reduction of phosphate from 0.42–0.18 mg L^{-1} (0.59 mg g^{-1}), nitrate from 4.1–2.3 mg L^{-1} (4.5 mg g^{-1})	263
Methylene blue (MB) and tetracycline hydrochloride	Bi-activated lignin-derived porous carbon	Langmuir, Freundlich, Temkin	Electrostatic interaction, pore filling, hydrogen bonding, and π–π interaction	Porous carbon with high surface area (3522 $m^2 g^{-1}$) and adsorption capacity of 1364 (MB) and 1682 mg g^{-1} (tetracycline hydrochloride)	264
Polystyrene nanoplastics in wastewater	Lignin-based activated carbon	Langmuir, Freundlich, Redlich–Peterson, Toth, Slips, MLSE	π–π interactions, H-bonding	Highest surface area of 1389 and 1063 $m^2 g^{-1}$ with KOH and $FeCl_3$ activation. Adsorption capacity was 49.53 mg g^{-1}	57

bio-oil along with significant amounts of char. The char produced with KOH exhibited strong adsorption of the pesticide carbofuran in aqueous media. These findings indicate that controlled pyrolysis at specific temperatures, with additives and post-treatments, offers an effective route for converting industrial lignin waste into valuable products[256] (Table 7).

11. Conclusions and future research directions

This review comprehensively highlights the growing potential of lignin-derived carbon materials as sustainable and high-performance solutions for pollutant removal and oil–water separation. The escalating discharge of industrial effluents, oil spills, and emerging contaminants, coupled with limited freshwater availability, underscores the urgent need for environmentally benign remediation technologies. Lignin, accounting for 15–30% of lignocellulosic biomass and contributing over 60% of its carbon content, represents an abundant, renewable, and underutilised feedstock for advanced carbon materials. Thermochemical conversion routes such as pyrolysis, hydrothermal carbonisation, and chemical activation have enabled the transformation of lignin into porous carbons with exceptionally high surface areas (1700–2285 $m^2 g^{-1}$), tunable pore structures, and rich surface functionalities. The reviewed studies demonstrate that lignin-derived carbons exhibit remarkable adsorption capacities, often exceeding 300 mg g^{-1} for dyes and organic pollutants, and are efficient in removing heavy metals, pharmaceuticals, and oils. In addition, lignin-based foams, aerogels, and sponges have demonstrated outstanding oil-absorption efficiencies (20–40 g g^{-1}), high hydrophobicity, and excellent recyclability. The key adsorption mechanisms, including electrostatic interactions, π–π stacking, surface complexation, hydrogen bonding, and pore filling,

govern their superior performance. Compared with conventional activated carbons, lignin-derived carbons offer advantages in terms of sustainability, tunability, and cost-effectiveness. Despite these advances, challenges related to feedstock heterogeneity, process scalability, regeneration efficiency, and techno-economic feasibility remain.

Although significant progress has been made, several research gaps remain to enable the large-scale deployment of lignin-derived carbon materials in real-world water treatment applications. First, future studies should focus on improving feedstock consistency by correlating lignin source, extraction method, and molecular structure with final carbon properties. Standardisation of lignin pretreatment and fractionation strategies is essential to minimise batch-to-batch variability and ensure reproducible material performance. Second, scalable and energy-efficient synthesis routes require further optimisation. Chemical activation produces high-surface-area carbons, often using corrosive reagents and complex post-treatment steps. Future research should prioritise greener activation strategies, such as bio-based activating agents, physical activation, and hybrid low-temperature processes, to reduce environmental and economic burdens. Life cycle assessment (LCA) and techno-economic analysis (TEA) should be systematically integrated to evaluate the sustainability and commercial viability of lignin-derived carbons in comparison to conventional activated carbons. Third, adsorption studies should move beyond single-component systems toward complex, multi-contaminant matrices that better represent real wastewater conditions. Investigations into competitive adsorption, long-term stability, regeneration efficiency, and performance under fluctuating pH, salinity, and temperature conditions are crucial. Moreover, mechanistic insights using advanced *in situ* and *operando* characterisation techniques can further clarify adsorption pathways and structure–performance relationships. Fourth, the development of functional lignin-derived carbon architectures, such as membranes, monoliths, magnetic composites, and hybrid materials, offers promising opportunities for easy recovery, reduced pressure drops, and enhanced reusability. Integration with advanced treatment technologies, including electrochemical oxidation, capacitive deionisation, and photocatalysis, may further enhance treatment efficiency. Ultimately, future research should focus on pilot-scale demonstrations and field validation studies to bridge the gap between laboratory findings and industrial implementation. Addressing these challenges will accelerate the translation of lignin-derived carbon materials into practical, sustainable solutions for wastewater treatment and oil–water separation, reinforcing their role in next-generation environmental remediation technologies.

Author contributions

Sonal Vithoba Tarkar, and Anuradha K: conceptualisation, data curation, collection, data interpretation, experimentation, and writing original draft, Ranjeet Kumar Mishra: conceptualisation, data curation, methodology, investigation, visualisation, editing original draft, and supervision, Mubarak Marutholi: investigation, visualisation, data curations and editing original draft.

Conflicts of interest

The author declares that they have no known competing financial interests or personal relationships that could be perceived to influence the study reported in this paper.

Abbreviations

Molecular weight	MW
Maximum contaminant level	MCL
Per-and polyfluoroalkyl substance	PFAS
Reactive oxygen species	ROS
Carbon	C
Hydrogen	H
Nitrogen	N
Sulphur	S
Oxygen	O
Secondary cell wall	SCW
Tracheary elements	TE
γ-Valerolactone	GVL
Hydrothermal liquefaction	HTL
Unconfined compressive strength	UCS
Adsorption capacity	qe
Lignin multilayer microsphere	LMM
Hydrothermal carbonisation	HTC
Activated carbon filter	ACF
Phenylalanine/tyrosine ammonia lyase	PTAL
4-hydroxylase	C4H
4-Coumarate: coenzyme A ligase	4CL
Hydroxycinnamoyltransferase	HCT
p-Coumarate 3-hydroxylase	C3H
Ferulate 5-hydroxylase	F5H
Caffeoyl-CoA *O*-methyltransferase	CCoAOMT
Caffeoyl-CoA reductase	CCR
Caffeic acid *O*-methyltransferase	COMT
Degree of Condensation	DC
Water contact angle	WCA

Data availability

No primary research results, software or code have been included, and no new data were generated or analysed as part of this review.

Acknowledgements

The authors would like to thank Biomass, Bioenergy and Bioproducts (3B) Lab, School of Civil and Chemical Engineering, Manipal Institute of Technology, Manipal, Karnataka, for providing the necessary facilities.

References

1 A. Kumar, A. Kapoor, A. K. Rathoure, G. L. Devnani and D. B. Pal, *Sustainable Processes Connect*, 2025, **1**, 1.

2 A. Boretti and L. Rosa, *NPJ Clean Water*, 2019, **2**, 15.
3 T. E. Oladimeji, M. Oyedemi, M. E. Emetere, O. Agboola, J. B. Adeoye and O. A. Odunlami, *Heliyon*, 2024, **10**, e40370.
4 J. Gong, B. Xiang, Y. Sun and J. Li, *J. Mater. Chem. A*, 2023, **11**, 25093–25114.
5 B. Zhang, E. J. Matchinski, B. Chen, X. Ye, L. Jing and K. Lee, in *World Seas: an Environmental Evaluation Volume III: Ecological Issues and Environmental Impacts*, Elsevier, 2018, pp. 391–406.
6 S. Ullah, S. S. A. Shah, M. Altaf, I. Hossain, M. E. El Sayed, M. Kallel, Z. M. El-Bahy, A. ur Rehman, T. Najam and M. A. Nazir, *J. Anal. Appl. Pyrolysis*, 2024, **179**, 106480.
7 M. S. Saidi Fereshteh, K. Dornaz, N. Tarit, B. C. Gates and R. Mohammad Reza, *Energy Environ. Sci.*, 2014, **7**, 103–129.
8 M. Muddasar, M. Mushtaq, A. Beaucamp, T. Kennedy, M. Culebras and M. N. Collins, *ACS Sustain. Chem. Eng.*, 2024, **12**, 2352–2363.
9 D. S. Bajwa, G. Pourhashem, A. H. Ullah and S. G. Bajwa, *Ind. Crops Prod.*, 2019, **139**, 111526.
10 P. Cao, Y. Li and J. Shao, *ACS Omega*, 2024, **9**, 24453–24463.
11 D. Ouyang, X. Lei and H. Zheng, *Nanomaterials*, 2023, **13**, 620.
12 M. Dong, L. He, M. Jiang, Y. Zhu, J. Wang, W. Gustave, S. Wang, Y. Deng, X. Zhang and Z. Wang, *Int. J. Environ. Res. Public Health*, 2023, **20**, 1679.
13 Y. Zhang, E. K. Sam, J. Liu and X. Lv, *Waste Biomass Valorization*, 2023, **14**, 3147–3168.
14 C. Simon, O. Morel, G. Neutelings, F. Baldacci-Cresp, M. Baucher, C. Spriet, C. Biot, S. Hawkins and C. Lion, *Chem. Biomed. Imaging*, 2023, **1**, 479–487.
15 D. Ménard, L. Blaschek, K. Kriechbaum, C. C. Lee, H. Serk, C. Zhu, A. Lyubartsev, Nuoendagula, Z. Bacsik, L. Bergström, A. Mathew, S. Kajita and E. Pesquet, *Plant Cell*, 2022, **34**, 4877–4896.
16 F. M. Casimiro, C. A. E. Costa, C. Vega-Aguilar and A. E. Rodrigues, *Int. J. Biol. Macromol.*, 2022, **215**, 272–279.
17 A. Crivellaro, A. Piermattei, J. Dolezal, P. Dupree and U. Büntgen, *Commun. Biol.*, 2022, **5**, 767.
18 N. Obrzut, R. Hickmott, L. Shure and K. A. Gray, *RSC Sustainability*, 2023, **1**, 2328–2340.
19 P. Li, J. Ren, Z. Jiang, L. Huang, C. Wu and W. Wu, *RSC Adv.*, 2022, **12**, 10289–10305.
20 J. C. del Río, J. Rencoret, A. Gutiérrez, T. Elder, H. Kim and J. Ralph, *ACS Sustain. Chem. Eng.*, 2020, **8**, 4997–5012.
21 Y. Tobimatsu and M. Schuetz, *Curr. Opin. Biotechnol.*, 2019, **56**, 75–81.
22 Y. Li, X. Zhang, J. Liu, K. Yu, X. Chen, L. Yuan, S. Peng, L. Zhou and W. Liu, *Food Qual. Saf.*, 2025, **9**, 1–19.
23 Y. Li, X. Meng, R. Meng, T. Cai, Y. Pu, Z.-M. Zhao and A. J. Ragauskas, *RSC Adv.*, 2023, **13**, 12750–12759.
24 X. Jiang, R. Sun, M. Kollman, H. min Chang and H. Jameel, *J. Wood Chem. Technol.*, 2023, **43**, 320–336.
25 D. D. S. Argyropoulos, C. Crestini, C. Dahlstrand, E. Furusjö, C. Gioia, K. Jedvert, G. Henriksson, C. Hulteberg, M. Lawoko, C. Pierrou, J. S. M. Samec, E. Subbotina, H. Wallmo and M. Wimby, *ChemSusChem*, 2023, **16**, 1–34.
26 W. Li, Y. Zhang, L. Das, Y. Wang, M. Li, N. Wanninayake, Y. Pu, D. Y. Kim, Y.-T. Cheng, A. J. Ragauskas and J. Shi, *RSC Adv.*, 2018, **8**, 38721–38732.
27 C. Li, Z. Wang, M. Hou, X. Cao, W. Jia, L. Huang, L. Wu, B. Wang, X. Sheng, Y. Guo and H. Shi, *Ind. Crops Prod.*, 2025, **223**, 120071.
28 J. Yao, M. Karlsson, M. Lawoko, K. Odelius and M. Hakkarainen, *RSC Sustainability*, 2023, **1**, 1211–1222.
29 M. E. Vuillemin, M. C. Quesada-Salas, C. Hadad, J. Jasniewski, E. Husson and C. Sarazin, *RSC Sustainability*, 2023, **1**, 853–865.
30 R. Bhadane, L. Vähäsalo, C. Xu and P. Eklund, *Biomass Bioenergy*, 2026, **205**, 108490.
31 Q. Zou, W. Wang and X. Wang, *Sci. Rep.*, 2024, **14**, 7558.
32 D. Tian, R. P. Chandra, J.-S. Lee, C. Lu and J. N. Saddler, *Biotechnol. Biofuels*, 2017, **10**, 157.
33 S. Magina and D. V. Evtuguin, *Biomass Bioenergy*, 2025, **198**, 107884.
34 G. Resende, G. D. Azevedo, F. Souto and V. Calado, *ACS Omega*, 2024, **9**, 50945–50956.
35 M. H. Tanis, E. Vercoutere, M. Galbe, B. Al-Rudainy and O. Wallberg, *ACS Sustain. Chem. Eng.*, 2025, **13**, 8457–8468.
36 J. Ruwoldt, F. H. Blindheim and G. Chinga-Carrasco, *RSC Adv.*, 2023, **13**, 12529–12553.
37 E. Jasiukaitytė-Grojzdek, T. Ročnik Kozmelj, G. Tofani, B. Segers, P. Nimmegeers, P. Billen, R. Pogorevc, B. Likozar and M. Grilc, *ACS Sustain. Chem. Eng.*, 2025, **13**, 3452–3466.
38 M. Tanase-Opedal and J. Ruwoldt, *ACS Omega*, 2022, **7**, 46583–46593.
39 S. Park, J. Jae, A. Farooq, E. E. Kwon, E. D. Park, J.-M. Ha, S.-C. Jung and Y.-K. Park, *Appl. Energy*, 2019, **255**, 113801.
40 F. S. Toma, Z. Jemaat, M. M. R. Khan, R. M. Yunus and M. D. H. Beg, in *Materials Today: Proceedings*, Elsevier Ltd, 2022, vol. 107, pp. 166–171.
41 A. M. Borrero-López, A. Blánquez, C. Valencia, M. Hernández, M. E. Arias, M. E. Eugenio, Ú. Fillat and J. M. Franco, *ACS Sustain. Chem. Eng.*, 2018, **6**, 5198–5205.
42 J. Ruwoldt, K. Syverud and M. Tanase-Opedal, *Sustainable Chem. Environ.*, 2024, **6**, 100102.
43 M. Wang, X. Luo, Q. Wang, V. Strehmel, Z. Chen, S. Li and B. Strehmel, *Commun. Chem.*, 2025, **8**, 199.
44 D. Sartika, A. Firmanda, I. W. Arnata, F. Fahma, D. A. Rusmawati, S. Robbani, A. Afifah, S. Bakhri, A. A. Y. Habib, M. Jusliandi and D. P. Putra, *Int. J. Biol. Macromol.*, 2025, **322**, 146859.
45 A. Khajeh, Z. Nazari, M. Movahedrad and A. H. Vakili, *Sci. Total Environ.*, 2024, **943**, 173500.
46 E. S. Wibowo and B.-D. Park, *Molecules*, 2023, **28**, 2755.
47 D. Aydemir, M. E. Ergun, S. K. Gulsoy, Z. E. Ozan and G. Gunduz, *Biofuels, Bioprod. Biorefin.*, 2024, **18**, 251–264.
48 S. Yu, J. He, Z. Zhang, Z. Sun, M. Xie, Y. Xu, X. Bie, Q. Li, Y. Zhang, M. Sevilla, M. Titirici and H. Zhou, *Adv. Mater.*, 2024, **36**, 1–44.
49 O. Salcedo-Puerto, C. Mendoza-Martinez, J. Saari and E. Vakkilainen, *Fuel*, 2024, **373**, 132389.

50 C. Yun, K. Kong, Y. Ban, H. Zhou, J. Hao, N. Li, K. Zhi, Y. Wang and Q. Liu, *J. Energy Inst.*, 2025, **123**, 102337.
51 A. Eraghi Kazzaz and P. Fatehi, *Ind. Crops Prod.*, 2020, **154**, 112732.
52 S. Sethupathy, G. Murillo Morales, L. Gao, H. Wang, B. Yang, J. Jiang, J. Sun and D. Zhu, *Bioresour. Technol.*, 2022, **347**, 126696.
53 A. Kylili, M. Koutinas, P. Z. Georgali and P. A. Fokaides, *Int. J. Sustainable Energy*, 2023, **42**, 1008–1027.
54 N. Ahmad, S. Aslam, N. Hussain, M. Bilal and H. M. N. Iqbal, *Bioenergy Res.*, 2023, **16**, 1246–1263.
55 M. Alherech, S. Omolabake, C. M. Holland, G. E. Klinger, E. L. Hegg and S. S. Stahl, *ACS Cent. Sci.*, 2021, **7**, 1831–1837.
56 T. Makaveckas, A. Šimonėlienė and V. Šipailaitė-Ramoškienė, *Sustainability*, 2025, **17**, 9913.
57 M. A. Álvarez-Montero, E. Sanz-Santos, A. Gómez-Avilés, C. Belver and J. Bedia, *Sep. Purif. Technol.*, 2025, **361**, 131380.
58 A. J. Adebayo and A. Olanrewaju, *Chem. Afr.*, 2025, **8**, 1711–1741.
59 I. F. Demuner, J. L. Colodette, A. J. Demuner and C. M. Jardim, *Bioresources*, 2019, **14**, 7543–7581.
60 T. Aro and P. Fatehi, *ChemSusChem*, 2017, **10**, 1861–1877.
61 G. Tofani, E. Jasiukaitytė-Grojzdek, M. Grilc and B. Likozar, *Green Chem.*, 2024, **26**, 186–201.
62 M. H. Lahtinen, J. Mikkilä, K. S. Mikkonen and I. Kilpeläinen, *J. Agric. Food Chem.*, 2021, **69**, 5955–5965.
63 C. Allegretti, S. Fontanay, Y. Krauke, M. Luebbert, A. Strini, J. Troquet, S. Turri, G. Griffini and P. D'Arrigo, *ACS Sustain. Chem. Eng.*, 2018, **6**, 9056–9064.
64 G. Shulga, B. Neiberte, A. Verovkins, V. Kudrjavceva and T. Betkers, in *Environment Technology Resources - Proceedings of the 16th International Scientific and Practical Conference*, RTU PRESS, 2025, vol. 1, pp. 497–502.
65 M. Parot, D. Rodrigue and T. Stevanovic, *Bioresour. Technol. Rep.*, 2022, **17**, 100880.
66 L. Qi, J. Liu, J. Peng, G. Yang, F. Li, Y. Xue and J. Chen, *Polymers*, 2021, **13**, 1600.
67 L. Y. Ee, Y. K. Tan, J. Miao, H. T. Chu and S. F. Y. Li, *Green Chem.*, 2023, **25**, 3137–3151.
68 T. Pang, G. Wang, H. Sun, W. Sui and C. Si, *Ind. Crops Prod.*, 2021, **165**, 113442.
69 D. S. Zijlstra, J. de Korte, E. P. C. de Vries, L. Hameleers, E. Wilbers, E. Jurak and P. J. Deuss, *Front. Chem.*, 2021, **9**, 1–14.
70 Q. Hua, L.-Y. Liu, M. A. Karaaslan and S. Renneckar, *Front. Chem.*, 2019, **7**, 1–10.
71 F. Andriani and M. Lawoko, *Biomacromolecules*, 2024, **25**, 4246–4254.
72 A. Rahmani, A. Abdulkhani, A. Ashori and J. Hosseinzadeh, *Sci. Rep.*, 2024, **14**, 28932.
73 G. Henriksson, U. Germgård and M. E. Lindström, *Nord. Pulp Pap. Res. J.*, 2024, **39**, 297–311.
74 C. S. Lancefield, H. J. Wienk, R. Boelens, B. M. Weckhuysen and P. C. A. Bruijnincx, *Chem. Sci.*, 2018, **9**, 6348–6360.
75 J. Li, Y.-N. Zha, H.-M. Wang, J.-N. Tian and Q.-X. Hou, *Ind. Crops Prod.*, 2025, **229**, 121004.
76 L. Kong, Z. Jin, F. Zhu, M. He, F. Qian and X. Peng, *Environ. Sci. Technol. Lett.*, 2024, **11**, 752–758.
77 Y. Cao, W. Qiu, J. Li, J. Jiang and S. Pang, *Sci. Total Environ.*, 2021, **765**, 142762.
78 H. S. N. Hawanis, S. H. R. Shamimimraphay, R. A. Ilyas, R. Jalil, R. Ibrahim, M. Y. M. Zuhri, H. A. A. Azriena, R. A. Majid and W. Fatriasari, *Ind. Crops Prod.*, 2025, **224**, 120307.
79 L. G. Nair, K. Agrawal and P. Verma, *Bioresour. Bioprocess.*, 2023, **10**, 50.
80 D. Wei Kit Chin, S. Lim, Y. L. Pang and M. K. Lam, *Biofuels, Bioprod. Biorefin.*, 2020, **14**, 808–829.
81 R. S. Abolore, S. Jaiswal and A. K. Jaiswal, *Ind. Crops Prod.*, 2025, **235**, 121696.
82 S. Roy, B. Godbole, N. R. Shiju and P. Biswas, *Mater. Today Chem.*, 2025, **47**, 102826.
83 V. Ponnuchamy, O. Gordobil, R. H. Diaz, A. Sandak and J. Sandak, *Int. J. Biol. Macromol.*, 2021, **168**, 792–805.
84 I. Sapouna, G. van Erven, E. Heidling, M. Lawoko and L. S. McKee, *ACS Sustain. Chem. Eng.*, 2023, **11**, 15533–15543.
85 G. Ischia, A. Yoko, L. Fiori and T. Adschiri, *Int. J. Biol. Macromol.*, 2025, **330**, 147997.
86 D. Mohan, K. Abhishek, A. Sarswat, M. Patel, P. Singh and C. U. Pittman, *RSC Adv.*, 2018, **8**, 508–520.
87 M. M. Mian and G. Liu, *RSC Adv.*, 2018, **8**, 14237–14248.
88 H. B. Truong, V. D. Dang, A. P. Khedulkar, J. Adorna, W.-J. Yu, T. A. N. Bui, T. Annadurai, M. Arshad, M.-K. Nguyen, L. K. H. Pham, N. C. Toan, G. T. Thu Hong, R. Saini, H. T. Nguyen, C. C. Truong and T. Van Anh, *RSC Adv.*, 2026, **16**, 5834–5851.
89 P. Khurana, S. Sran, R. Kumar Das, L. Sanchez-Silva and S. Kaur Brar, *RSC Adv.*, 2025, **15**, 20330–20340.
90 Y. Song, J. Tan, M. Jin, Z. Liu, J. Zhu, M. E. A. El-sayed, I. A. Abdelhafeez, Y. Zhang and Z. Shen, *J. Anal. Appl. Pyrolysis*, 2025, **191**, 107236.
91 L. Zhu, X. Liu, Y. Wu, Q. Wang, H. Wang and D. Li, *Renewable Energy*, 2022, **198**, 1318–1327.
92 W. Li and J. Shi, *Front. Bioeng. Biotechnol.*, 2023, **11**, 1–19.
93 H. Mao, X. Chen, R. Huang, M. Chen, R. Yang, P. Lan, M. Zhou, F. Zhang, Y. Yang and X. Zhou, *Sci. Rep.*, 2018, **8**, 9501.
94 C. H. Kim, M. Kim, J. Lee, H. Choi, S. Y. Lee and S. J. Park, *J. Mater. Chem. A*, 2025, **13**, 14580–14587.
95 Y. Lan, S. Xu, Y. Fu, L. Jin, Y. Han, X. He, Q. Wang, Y. Lv and H. Cui, *Diam. Relat. Mater.*, 2025, **152**, 111875.
96 M. Hu, J. Chen and Y. Liu, *Bioresour. Technol.*, 2024, **401**, 130712.
97 Y. Sun, T. Wang, X. Sun, L. Bai, C. Han and P. Zhang, *Ind. Crops Prod.*, 2021, **166**, 113473.
98 Z. Yang, X. Wan, Y. Chen, X. Chen, Z. Wang, C. Zhang, V. Kumar, C. Varrone, X. Xiao, P. Yu and W. Huang, *J. Environ. Chem. Eng.*, 2025, **13**, 119080.
99 M. Castiglioni, L. Rivoira, I. Ingrando, M. Del Bubba and M. C. Bruzzoniti, *Molecules*, 2021, **26**, 5063.
100 M. Sbizzaro, S. César Sampaio, R. Rinaldo dos Reis, F. de Assis Beraldi, D. Medina Rosa, C. Maria Branco de Freitas

Maia, C. Saramago de Carvalho Marques dos Santos Cordovil, C. Tillvitz do Nascimento, E. Antonio da Silva and C. Eduardo Borba, *J. Mol. Liq.*, 2021, **343**, 117667.
101 F. Ma, H. Zhao, X. Zheng, B. Zhao, J. Diao and Y. Jiang, *J. Environ. Chem. Eng.*, 2023, **11**, 109747.
102 R. Kumar Mishra, D. Jaya Prasanna Kumar, A. Narula, S. Minnat Chistie and S. Ullhas Naik, *Fuel*, 2023, **343**, 127968.
103 R. Kumar Mishra, B. Singh and B. Acharya, *Carbon Resour. Convers.*, 2024, **7**, 100228.
104 U. Sahoo, S. Maitra, A. Hossain, D. T. Santosh, S. Nath, M. Sairam, L. Sagar, J. Jena, S. Pattanayak, H. I. Gitari and E. Rezaei-Chiyaneh, in *Biochar-assisted Remediation of Contaminated Soils under Changing Climate*, Elsevier, 2024, pp. 1–33.
105 X. C. Yuan Yang, Li Jie, A. K. Patel, D. Cheng-Di, X. Jin, C. Gu, A. C. K. Yip, D. C. W. Tsang and Ok Y. Sik, *Biotechnol. Adv.*, 2023, **67**, 108181.
106 P. G. Sangrulkar Shruti and K. Balasubramanian, *Bioresour. Technol. Rep.*, 2023, **24**, 101684.
107 H. Sarwar, N. Ratnayake, A. Vuppaladadiyam, S. Pabba, S. Patel, L. Khudur, J. Elliot, T. Ngo, G. Veluswamy, H. Vuthaluru, A. S. Ball and K. Shah, *Biomass Bioenergy*, 2026, **209**, 108858.
108 L. W. Luo Jiaxiao, J. Lv, Z. Liu, T. Sun, Yi Yang and Z. Yong-Guan, *Environ. Sci. Technol.*, 2023, **57**, 11357–11372.
109 W. Gao, Z. Lin, H. Chen, S. Yan, Y. Huang, X. Hu and S. Zhang, *Fuel Process. Technol.*, 2022, **237**, 107468.
110 G. Murtaza, M. Usman, S. Hyder, H. S. El-Beltagi, K. M. Alwutayd, Z. Ahmed, J. Iqbal, S. Ullah and R. Iqbal, *Ind. Crops Prod.*, 2026, **239**, 122390.
111 B. Qiu, Q. Shao, J. Shi, C. Yang and H. Chu, *Sep. Purif. Technol.*, 2022, **300**, 121925.
112 A. D. Igalavithana, S. Mandal, N. K. Niazi, M. Vithanage, S. J. Parikh, F. N. D. Mukome, M. Rizwan, P. Oleszczuk, M. Al-Wabel, N. Bolan, D. C. W. Tsang, K. H. Kim and Y. S. Ok, *Crit. Rev. Environ. Sci. Technol.*, 2017, **47**, 2275–2330.
113 R. K. Mishra and K. Mohanty, *Biofuel Res. J.*, 2022, **9**, 1736–1749.
114 D. Akhil, D. Lakshmi, A. Kartik, D.-V. N. Vo, J. Arun and K. P. Gopinath, *Environ. Chem. Lett.*, 2021, **19**, 2261–2297.
115 Y. Deng, M. Li, Z. Zhang, Q. Liu, K. Jiang, J. Tian, Y. Zhang and F. Ni, *J. Environ. Chem. Eng.*, 2021, **9**, 105079.
116 L. Jia, Y. Yu, J. R. Guo, S. N. Qin, Y. L. Wang, X. Shen, B. G. Fan and Y. Jin, *Energy and Fuels*, 2020, **34**, 12743–12756.
117 Z. Ma, Y. Yang, Q. Ma, H. Zhou, X. Luo, X. Liu and S. Wang, *J. Anal. Appl. Pyrolysis*, 2017, **127**, 350–359.
118 D. N. G. Ngo, X.-Y. Chuang, C.-P. Huang, L.-C. Hua and C. Huang, *J. Environ. Chem. Eng.*, 2023, **11**, 110003.
119 S. Fan and L. Zhang, *Biomass Convers. Biorefin.*, 2021, **11**, 1719–1732.
120 S. Sutradhar, A. Mondal, F. Kuehne, O. Krueger, S. K. Rakshit and K. Kang, *Plants*, 2024, **13**, 820.
121 T.-J. Jiang, H. M. Morgan, W.-T. Tsai, H. Chien, T.-B. Yen and Y.-R. Lee, *Sustainability*, 2024, **16**, 6623.
122 Y. Xian, J. Wu, G. Yang, R. Liao, X. Zhang, H. Peng, X. Yu, F. Shen, L. Li and L. Wang, *RSC Adv.*, 2018, **8**, 28002–28012.
123 E. Ernest Mbamalu and I. Yakub Mohammed, *Waste Manag. Bull.*, 2024, **2**, 194–208.
124 J. Lee, X. Yang, S. H. Cho, J. K. Kim, S. S. Lee, D. C. W. Tsang, Y. S. Ok and E. E. Kwon, *Appl. Energy*, 2017, **185**, 214–222.
125 C. del Pozo, F. Rego, N. Puy, J. Bartrolí, E. Fàbregas, Y. Yang and A. V. Bridgwater, *Waste Manage.*, 2022, **148**, 106–116.
126 T. X. Vuong, D. P. Nguyen, V. H. Ngoc Nguyen, T. T. Ha Pham and T. T. Thuy Nguyen, *RSC Adv.*, 2025, **15**, 11975–12000.
127 A. W. Tadesse, M. Huang and T. Zhou, *Molecules*, 2025, **30**, 4288.
128 J.-H. Chang, P. Sivasubramanian, C.-D. Dong and M. Kumar, *Bioresour. Technol. Rep.*, 2023, **21**, 101346.
129 H. Chaudhary, J. Dinakaran, T. Notup, K. Vikram and K. S. Rao, *Environ. Manage.*, 2024, **73**, 408–424.
130 B. Huang, D. Huang, Q. Zheng, C. Yan, J. Feng, H. Gao, H. Fu and Y. Liao, *RSC Adv.*, 2023, **13**, 10397–10407.
131 A. Subratti, J. L. Vidal, L. J. Lalgee, F. M. Kerton and N. K. Jalsa, *Sustain. Chem. Pharm.*, 2021, **21**, 100421.
132 A. Kumar, R. K. Mishra and S. jaglan, *Process Saf. Environ. Prot.*, 2022, **163**, 68–81.
133 J. Xu, J. Liu, P. Ling, X. Zhang, K. Xu, L. He, Y. Wang, S. Su, S. Hu and J. Xiang, *Energy*, 2020, **202**, 117644.
134 P. R. Yaashikaa, P. S. Kumar, S. Varjani and A. Saravanan, *Biotechnol. Rep.*, 2020, **28**, e00570.
135 K. Velusamy, S. Periyasamy, P. S. Kumar, T. Jayaraj, R. Krishnasamy, J. Sindhu, D. Sneka, B. Subhashini and D.-V. N. Vo, *Environ. Pollut.*, 2021, **287**, 117632.
136 G. S. Braz, J. do C. L. Carvalho, J. G. de Andrade, A. T. D. Junior, R. P. de Lima, E. N. Lima, O. E. Ferreira, M. A. de Oliveira, A. C. da S. Bezerra and A. R. T. Machado, *Desalin. Water Treat.*, 2025, **321**, 100958.
137 P. Pradhan and I. M. Nambi, *Process Saf. Environ. Prot.*, 2025, **199**, 107268.
138 M. Shahabi Nejad and H. Sheibani, *J. Environ. Chem. Eng.*, 2022, **10**, 107363.
139 Y. H. Fseha, J. Shaheen and B. Sizirici, *Emerg. Contam.*, 2023, **9**, 100202.
140 N. Rambhatla, T. F. Panicker, R. K. Mishra, S. K. Manjeshwar and A. Sharma, *Results Eng.*, 2025, **25**, 103679.
141 L. Ton-That, T.-P.-T. Nguyen, B.-N. Duong, D.-K. Nguyen, N.-A. Nguyen, T. Ho and V.-P. Dinh, *Biochem. Eng. J.*, 2024, **212**, 109525.
142 L. Usevičiūtė and E. Baltrėnaitė-Gedienė, *Biomass Convers. Biorefin.*, 2021, **11**, 2775–2793.
143 H. Chaudhary, J. Dinakaran and K. S. Rao, *J. Environ. Chem. Eng.*, 2024, **12**, 113003.
144 J. Lin and G. Zhao, *Polymers*, 2016, **8**(10), 1–10.
145 X. Zhao, W. Zhao, Z. Chen, C. Liu, Y. Zhou, Z. Zhu, Y. Yang, J. Qi and J. Li, *J. Environ. Chem. Eng.*, 2024, **12**, 114799.
146 H. Zhang, L. Zhu, X. Xue, Q. Ren, J. Cui, B. Wang, D. Zhang and F. Cheng, *Surf. Interfaces*, 2025, **76**, 107907.

147 A. A. Bolotnikov, I. S. Krechetov, T. L. Lepkova and V. V. Berestov, *J. Electroanal. Chem.*, 2025, **999**, 119603.
148 Y. Li, X. Zhang, J. Deng, X. Yang, J. Wang and Y. Wang, *Chem. Phys. Lett.*, 2020, **747**, 137325.
149 Y. Chen, D. Wang, X. Wang, J. Wu and S. Song, *Sustainable Environ. Res.*, 2025, **35**, 4.
150 G. Wang, B. Dou, Z. Zhang, J. Wang, H. Liu and Z. Hao, *J. Environ. Sci.*, 2015, **30**, 65–73.
151 Q. Liu, Q. Chang, X. Liao, Y. Jiang, X. Lyu, Q. Zhao, J. Diao, X. Wang, X. Huang and S. Lyu, *Powder Technol.*, 2024, **448**, 120322.
152 L. Kumar, N. Chakinala, P. Kumar and A. G. Chakinala, *Chem. Eng. Process.*, 2025, **217**, 110538.
153 A. E. Moharm, G. A. El Naeem, H. M. A. Soliman, A. I. Abd-Elhamid, A. A. El-Bardan, T. S. Kassem, A. A. Nayl and S. Bräse, *Polymers*, 2022, **14**, 2587.
154 H. Cheng, Y. Liu and X. Li, *J. Hazard. Mater.*, 2021, **415**, 125749.
155 A. Mishra, L. Kaur, M. Sharma, P. Sharma, S. Murab, H. Ojha, J. Pandey and M. Pathak, *J. Mol. Struct.*, 2025, **1341**, 142657.
156 M. Shen, F. Kong, W. Guo, Z. Zuo, T. Gao, S. Chen, L. Tong, P. Zhang, L. Wang, P. K. Chu and Y. Ding, *Chem. Eng. J.*, 2024, **479**, 147923.
157 N. K. Niazi, I. Bibi, M. Shahid, Y. S. Ok, E. D. Burton, H. Wang, S. M. Shaheen, J. Rinklebe and A. Lüttge, *Environ. Pollut.*, 2018, **232**, 31–41.
158 X.-F. Tan, S.-S. Zhu, R.-P. Wang, Y.-D. Chen, P.-L. Show, F.-F. Zhang and S.-H. Ho, *Chin. Chem. Lett.*, 2021, **32**, 2939–2946.
159 D. F. de O. Torchia, E. Zonta, A. M. de Andrade and A. C. García, *Braz. J. Chem. Eng.*, 2022, **39**, 415–427.
160 R. Griffo, F. Di Natale, M. Minale, M. Sirignano, A. Parisi and C. Carotenuto, *Nanomaterials*, 2024, **14**, 301.
161 S. Li, O. Torsæter, H. C. Lau, N. J. Hadia and L. P. Stubbs, *Front. Phys.*, 2019, **7**, 1–12.
162 Y. Ge and Z. Li, *ACS Sustain. Chem. Eng.*, 2018, **6**, 7181–7192.
163 O. Tkachenko, D. Diment, D. Rigo, M. Stromme and T. M. Budnyak, *Biomacromolecules*, 2024, **25**, 4292–4304.
164 B. G. Fouda-Mbanga, E. Prabakaran and K. Pillay, *Biotechnol. Rep.*, 2021, **30**, e00609.
165 Z. Zhang, Y. Chen, D. Wang, D. Yu and C. Wu, *Ind. Crops Prod.*, 2023, **193**, 116119.
166 F. Chen, Y. Sun, C. Liang, T. Yang, S. Mi, Y. Dai, M. Yu and Q. Yao, *Sci. Rep.*, 2022, **12**, 17714.
167 E. Ungureanu, M. E. Fortună, D. C. Topa, C. O. Brezuleanu, V. I. Ungureanu, C. Chirută, R. Rotaru, B. M. Tofanica, V. I. Popa and D. C. Jităreanu, *Polymers*, 2023, **15**, 3794.
168 R. A. Costa, D. Lukić, V. Vasić, I. Sulaeva, T. Rosenau, A. Lourenço, M. Antov and J. Gominho, *Sustainable Chem. Environ.*, 2026, **13**, 100308.
169 R. Pourbaba, A. Abdulkhani, A. Rashidi and A. Ashori, *Sci. Rep.*, 2024, **14**, 9039.
170 W. Y. El-Nazer, T. E. Farrag, M. S. Beheary and R. A. Mansour, *Next Mater.*, 2025, **9**, 101219.
171 X. Wang, X. Wang, W. Chen, J. Yuan and Q. Zhang, *ACS Omega*, 2025, **10**, 13816–13828.
172 N. Akiba, A. T. Omori and I. Gaubeur, *Chemosphere*, 2022, **308**, 136538.
173 I. G. Al-Labadi, M. Horváth, A. T. Alkilani, A. M. Al-Ma'abreh, M. J. K. Bashir, B. E. Keshta, G. Hanbali, W. Al Zoubi, M. R. Abukhadra, H. A. Alqhtani and M. H. Eid, *Front. Water*, 2025, **7**, 1–18.
174 M. Macena, H. Pereira, L. Grosche, B. Esteves, I. Santos-Vieira and L. Cruz-Lopes, *Materials*, 2025, **18**, 2320.
175 Z. Wang and J. Li, *Molecules*, 2023, **28**, 7694.
176 L. G. X. de Souza, F. J. C. Teran, R. M. F. Cuba, A. R. Chaves and K. C. da Silva, *Toxics*, 2025, **13**, 257.
177 M. Masliha, M. Padnekar, J. De Micco, S. Ponnupandian, K. Mondal and R. B. Padamati, *Heliyon*, 2025, **11**, e42559.
178 X. Wang, C. Jiang, B. Hou, Y. Wang, C. Hao and J. Wu, *Chemosphere*, 2018, **206**, 587–596.
179 X. Meng, B. Scheidemantle, M. Li, Y. Y. Wang, X. Zhao, M. Toro-González, P. Singh, Y. Pu, C. E. Wyman, S. Ozcan, C. M. Cai and A. J. Ragauskas, *ACS Omega*, 2020, **5**, 2865–2877.
180 A. Gupta, S. Kumar, Y. Bajpai, K. Chaturvedi, P. Johri, R. K. Tiwari, V. Vivekanand and M. Trivedi, *Front. Microbiol.*, 2024, **15**, 1–11.
181 L. N. Munuhe, E. S. Madivoli, D. M. Nzilu, P. N. Lemeitaron and P. K. Kimani, *J. Chem.*, 2025, **2025**, 1–17.
182 P. Mahdavi, A. Siol and J. Thöming, *J. Environ. Chem. Eng.*, 2025, **13**, 117520.
183 T. O. Ajiboye, P. O. Oladoye and E. O. Omotola, *Arabian J. Geosci.*, 2024, **51**, 100225.
184 A. Verma, G. Sharma, A. Kumar, P. Dhiman, G. T. Mola, A. Shan and C. Si, *Chemosphere*, 2024, **352**, 141365.
185 B. Biswas, A. Joseph, V. P. Ranjan and S. Goel, *ACS ES&T Water*, 2024, **4**, 5207–5224.
186 H. Wang, T. Shen, Y. Wang, Z. Lv, Y. Liu, J. Wu, T. Li, S. Wang and Y. Shang, *Toxics*, 2025, **13**, 759.
187 E. C. Silva, K. B. L. de Góis, D. F. de Santana Souza, C. E. de A. Padilha, D. C. da Silva and A. de O. Wanderley Neto, *J. Indian Chem. Soc.*, 2025, **102**, 102013.
188 B. Xie, Y. Hou and Y. Li, *BioResources*, 2020, **16**(1), 249–262.
189 Z. Zhang, Y. Chen and C. Wu, *Polymers*, 2022, **14**, 2824.
190 Z. Abbas, S. Ali, M. Rizwan, I. E. Zaheer, A. Malik, M. A. Riaz, M. R. Shahid, M. Z. ur Rehman and M. I. Al-Wabel, *Arabian J. Geosci.*, 2018, **11**, 448.
191 J. L. Munera-Echeverri, V. Martinsen, L. T. Strand, V. Zivanovic, G. Cornelissen and J. Mulder, *Sci. Total Environ.*, 2018, **642**, 190–197.
192 A. Y. Li, H. Deng, Y. H. Jiang, C. H. Ye, B. G. Yu, X. L. Zhou and A. Y. Ma, *Langmuir*, 2020, **36**, 9160–9174.
193 T. G. Ambaye, M. Vaccari, E. D. van Hullebusch, A. Amrane and S. Rtimi, *Int. J. Environ. Sci. Technol.*, 2021, **18**, 3273–3294.
194 Y. Sun, F. Yu, C. Han, C. Houda, M. Hao and Q. Wang, *Water*, 2022, **14**, 1691.
195 H. Wang, Q. Chen, H. Xia, R. Liu and Y. Zhang, *Sep. Purif. Technol.*, 2024, **328**, 125074.
196 K. Yang, K. Shen, B. Zhang, Y. Hua, B. Guo and Y. Zhang, *J. Environ. Chem. Eng.*, 2024, **12**, 113645.

197 Y. Tong, P. J. McNamara and B. K. Mayer, *Environ. Sci.*, 2019, **5**, 821–838.
198 Y. Zhu, B. Yi, Q. Yuan, Y. Wu, M. Wang and S. Yan, *RSC Adv.*, 2018, **8**, 19917–19929.
199 S. Dou, X.-X. Ke, Z.-D. Shao, L.-B. Zhong, Q.-B. Zhao and Y.-M. Zheng, *Chemosphere*, 2022, **287**, 131962.
200 S. Guo, Z. Zou, Y. Chen, X. Long, M. Liu, X. Li, J. Tan and R. Chen, *Environ. Pollut.*, 2023, **320**, 121060.
201 T. Wang, M. Jiang, X. Yu, N. Niu and L. Chen, *Sep. Purif. Technol.*, 2022, **302**, 122116.
202 B. Gao, Q. Chang and H. Yang, *Sci. Total Environ.*, 2021, **765**, 144427.
203 R. Zhou, M. Zhang and S. Shao, *Sci. Rep.*, 2022, **12**, 13662.
204 P. K. Mahish, D. K. Verma and S. K. Jadhav, *Biosorbents*, 2024, pp. 123–132.
205 W. Gao, Y. Shi, Y. Zhou, J. Jia and S. Chen, *Sci. Rep.*, 2025, **15**, 19432.
206 U. A. Edet and A. O. Ifelebuegu, *Processes*, 2020, **8**, 665.
207 P. Duarah and M. K. Purkait, *Colloids Surf., A*, 2025, **715**, 136635.
208 H. N. Nguyen, T. P. Bui, T. T. H. Tran, T. H. H. Nguyen and P. T. Le, *Adv. Bamboo Sci.*, 2025, **11**, 100144.
209 B. Tekin and U. Acikel, *Gazi Univ. J. Sci.*, 2023, **36**, 495–509.
210 A. El Hanandeh, R. A. Abu-Zurayk, I. Hamadneh and A. H. Al-Dujaili, *Water Sci. Technol.*, 2016, **74**, 1899–1910.
211 X. Guo, Y. Liu and J. Wang, *J. Hazard. Mater.*, 2020, **400**, 123324.
212 X. Su, Y. Chen, Y. Li, J. Li, W. Song, X. Li and L. Yan, *J. Mol. Liq.*, 2022, **357**, 119083.
213 Z. Luo, X. Peng, W. Liang, D. Zhou, C. Dang and W. Cai, *Bioresour. Technol.*, 2023, **388**, 129762.
214 W.-H. Huang, Y.-J. Chang and D.-J. Lee, *Bioresour. Technol.*, 2024, **391**, 129984.
215 Y. Mei, S. Zhuang and J. Wang, *Sci. Total Environ.*, 2025, **968**, 178898.
216 A. Hu, Y. Zhang, P. Xiong, Y. Yang and Z. Liu, *ACS Eng. Au*, 2025, **47**, 3038–3052.
217 M. Musah, Y. Azeh, J. Mathew, M. Umar, Z. Abdulhamid and A. Muhammad, *Caliphate J. Sci, Technol.*, 2022, **4**, 20–26.
218 N. Liu, M. Zhu, H. Wang and H. Ma, *J. Mol. Liq.*, 2016, **223**, 335–342.
219 X. Kang, M. Sun, N. Geng, Y. Li, H. Wang, H. Pan, Q. Yang, Z. Yang, Y. Lou and Y. Zhuge, *Ecotoxicol. Environ. Saf.*, 2024, **281**, 116608.
220 G. A. Burk, A. Herath, G. B. Crisler, D. Bridges, S. Patel, C. U. Pittman and T. Mlsna, *Front. Environ. Sci.*, 2020, **8**, 1–11.
221 T. Liang, L. Li, C. Zhu, X. Liu, H. Li, Q. Su, J. Ye, B. Geng, Y. Tian, M. F. Sardar, X. Huang and F. Li, *Water*, 2020, **12**, 2720.
222 J. Chen, C. Tang, X. Li, J. Sun, Y. Liu, W. Huang, A. Wang and Y. Lu, *Water*, 2022, **14**, 3761.
223 R. Jin, J. Gong, Z. Li, B. Xiang, W. Liu and J. Li, *Sep. Purif. Technol.*, 2026, **386**, 136557.
224 X. Wang, C. Fu, C. Zhang, Z. Qiu and B. Wang, *Materials*, 2022, **15**, 4747.
225 M. Li, W. Huang, C. Ren, Q. Wu, S. Wang and J. Huang, *RSC Adv.*, 2022, **12**, 11517–11525.
226 H. Yun, S. Park, J. Bang, J. Kim, S. Jung, S. Won, S. Kim, H. Lim, S.-G. Kim, I.-G. Choi and H. W. Kwak, *Int. J. Biol. Macromol.*, 2025, **308**, 142618.
227 M. Wu and H. Jiang, *Phys. Status Solidi A*, 2025, **222**, 1–8.
228 Z. Feng, J. Zhang, R. Jia, Z. Cao, Y. Li and S. Wang, *Ind. Crops Prod.*, 2024, **218**, 119047.
229 D. Barker-Rothschild, J. Chen, Z. Wan, S. Renneckar, I. Burgert, Y. Ding, Y. Lu and O. J. Rojas, *Chem. Soc. Rev.*, 2025, **54**, 623–652.
230 P. Nargotra, M.-L. Tsai, C.-D. Dong, C.-H. Kuo, B. K. Bajaj, V. Sharma and C. Opin, *Environ. Sci. Health*, 2025, **48**, 100665.
231 A. Mostovoy, N. Eremeeva, A. Shcherbakov, M. Lopukhova, S. Ussenkulova, E. Zhunussova and A. Bekeshev, *Molecules*, 2025, **30**, 2285.
232 M. H. José, J. P. Canejo and M. H. Godinho, *Materials*, 2023, **16**, 2503.
233 S. Jiang, Q. Li, Q. Ma, B. Xu and T. Zou, *Molecules*, 2023, **28**, 7524.
234 K. Gao, J. Liu, X. Li, H. Gojzewski, X. Sui and G. J. Vancso, *ACS Sustain. Chem. Eng.*, 2022, **10**, 9334–9344.
235 D. Kim, R. Mauchauffé, J. Kim and S. Y. Moon, *Sci. Rep.*, 2021, **11**, 3169.
236 T. Alsawy, E. Rashad, M. El-Qelish and R. H. Mohammed, *NPJ Clean Water*, 2022, **5**, 29.
237 H. Tan, R. A. Wahab, P. Y. Ong, P. S. Goh, K. Y. Wong, Y. Van Fan and C. T. Lee, *Chem. Eng. Trans.*, 2023, **106**, 313–318.
238 F. Alcalde-Garcia, S. Prasher, S. Kaliaguine, J. R. Tavares and M.-J. Dumont, *ACS Eng. Au*, 2023, **3**, 443–460.
239 S. Satyam and S. Patra, *Heliyon*, 2024, **10**, e29573.
240 D. A. Gkika, A. K. Tolkou, I. A. Katsoyiannis and G. Z. Kyzas, *Sep. Purif. Technol.*, 2025, **368**, 132996.
241 J. Ren, X. Yang, Y. Wang, S. Zhang and J. Zhou, *Sci. Rep.*, 2025, **15**, 11792.
242 B. Zaarour and W. Liu, *J. Ind. Text.*, 2023, **53**, 1–39.
243 P. Li, Z. Zhang, X. Zhang, K. Li, Y. Jin and W. Wu, *RSC Adv.*, 2023, **13**, 3241–3254.
244 Z. Chen, W. Wei, H. Chen and B.-J. Ni, *Eco-Environ. & Health*, 2022, **1**, 86–104.
245 J. B. Rial and M. L. Ferreira, *Sci. Total Environ.*, 2022, **823**, 153370.
246 Y. Trivedi, M. Sharma, R. K. Mishra, A. Sharma, J. Joshi, A. B. Gupta, B. Achintya, K. Shah and A. K. Vuppaladadiyamd, *Desalination*, 2025, **600**, 118509.
247 R. Rashid, I. Shafiq, P. Akhter, M. J. Iqbal and M. Hussain, *Environ. Sci. Pollut. Res.*, 2021, **28**, 9050–9066.
248 X. Li, Y. Zhu, R. Abbassi and G. Chen, *Process Saf. Environ. Prot.*, 2022, **162**, 932–943.
249 H. Lu, D. Xi and G. Qin, *Sci. Total Environ.*, 2023, **874**, 162386.
250 D. P. Prendergast and P. M. Gschwend, *J. Clean. Prod.*, 2014, **78**, 233–242.
251 K. G. Akpomie and J. Conradie, *Biomass Convers. Biorefin.*, 2024, **14**, 539–551.

252 A. T. Hoang and X. D. Pham, *Journal of Marine Engineering & Technology*, 2021, **20**(3), 159–169.
253 N. Singh, R. R. Singhania, P. S. Nigam, C.-D. Dong, A. K. Patel and M. Puri, *Bioresour. Technol.*, 2022, **344**, 126415.
254 Y. Bentahar, C. Lomenech, A. Mija, E. de Jong, E. Bonjour, P. Jame and C. Hurel, *Biomass Convers. Biorefin.*, 2024, **14**, 13955–13970.
255 A. Shahid, M. Ishfaq, M. S. Ahmad, S. Malik, M. Farooq, Z. Hui, A. H. Batawi, M. E. Shafi, A. A. Aloqbi, M. Gull and M. A. Mehmood, *Bioresour. Technol.*, 2019, **289**, 121701.
256 D. T. Sarve, R. Dutta, A. Rastogi and J. D. Ekhe, *J. Indian Chem. Soc.*, 2022, **99**, 100398.
257 Y. Tan, X. Wang, F. Xiong, J. Ding, Y. Qing and Y. Wu, *Ind. Crops Prod.*, 2021, **171**, 113980.
258 F. Ogata, E. Nagahashi, H. Miki, C. Saenjum, T. Nakamura and N. Kawasaki, *Heliyon*, 2020, **6**, e04298.
259 W. Li, L. Chai, B. Du, X. Chen and R.-C. Sun, *Sep. Purif. Technol.*, 2023, **306**, 122644.
260 W. Huang, Z. Yang, J. Hu, X. Chen, W. Li, Z. Wang, C. Zhang, Q. Wang, X. Xiao and P. Yu, *Chem. Eng. J.*, 2024, **499**, 156262.
261 H. Bai, Y. Feng, C. Zhu, P. Guo, J. Wang, Y. Zhou, L. Zhang, S. Li and J. Chen, *J. Taiwan Inst. Chem. Eng.*, 2024, **164**, 105689.
262 B. Du, Y. Wang, Q. Zheng, X. Wang, X. Chen, J. Zhou, G. Yang and R.-C. Sun, *Sep. Purif. Technol.*, 2024, **330**, 125495.
263 F. V. Kewir, C. E. Astete, D. B. Nde, J. R. Eberhard, W. D. Constant and C. M. Sabliov, *Environ. Sci.:Adv.*, 2024, **3**, 1722–1734.
264 D. Bai, Z. Wei, X. Qiu and X. Lin, *Ind. Eng. Chem. Res.*, 2023, **62**, 13541–13553.